SENSORS & TRANSDUCERS

ISSN 1726-5479

vol. 273

2 / 26

Sensors for Automatic Control & Robotics

International Frequency Sensor Association Publishing

IFSA

Sensors & Transducers

International Official Open Access Journal of the International Frequency Sensor Association (IFSA) Devoted to Research and Development of Sensors and Transducers

Volume 273, Issue 2, June 2026

Editor-in-Chief
Prof., Dr. Sergey Y. YURISH

IFSA Publishing: Barcelona • Toronto

Sensors & Transducers is an open access journal which means that all content (article by article) is freely available without charge to the user or his/her institution. Users are allowed to read, download, copy, distribute, print, search, or link to the full texts of the articles, or use them for any other lawful purpose, without asking prior permission from the publisher or the author. This is in accordance with the BOAI definition of open access. Authors who publish articles in *Sensors & Transducers* journal retain the copyrights of their articles. The *Sensors & Transducers* journal operates under the Creative Commons License CC-BY.

Notice: No responsibility is assumed by the Publisher for any injury and/or damage to persons or property as a matter of products liability, negligence or otherwise, or from any use or operation of any methods, products, instructions or ideas contained in the material herein.

Published by International Frequency Sensor Association (IFSA) Publishing. Printed in the USA.

Sensors & Transducers

Volume 273, Issue 2
June 2026

www.sensorsportal.com

e-ISSN 1726-5479
ISSN 2306-8515

Editors-in-Chief: Professor, Dr. Sergey Y. Yurish, tel.: +34 696067716, e-mail: editor@sensorsportal.com

Editors for Western Europe
Meijer, Gerard C.M., Delft Univ. of Technology, The Netherlands
Ferrari, Vittorio, Universitá di Brescia, Italy
Mescheder, Ulrich, Univ. of Applied Sciences, Furtwangen, Germany

Editor for Eastern Europe
Sachenko, Anatoly, Ternopil National Economic University, Ukraine

Editors for North America
Katz, Evgeny, Clarkson University, USA
Datskos, Panos G., Oak Ridge National Laboratory, USA
Fabien, J. Josse, Marquette University, USA

Editor for Africa
Maki K., Habib, American University in Cairo, Egypt

Editors South America
Costa-Felix, Rodrigo, Inmetro, Brazil
Walsoe de Reca, Noemi Elisabeth, CINSO-CITEDEF UNIDEF (MINDEF-CONICET), Argentina

Editors for Asia
Ohyama, Shinji, Tokyo Institute of Technology, Japan
Zhengbing, Hu, Huazhong Univ. of Science and Technol., China
Li, Gongfa, Wuhan Univ. of Science and Technology, China

Editor for Asia-Pacific
Mukhopadhyay, Subhas, Massey University, New Zealand

International Advisory Board

Abdul Rahim, Ruzairi, Universiti Teknologi, Malaysia
Abramchuk, George, Measur. Tech. & Advanced Applications, Canada
Aluri, Geetha S., Globalfoundries, USA
Ascoli, Giorgio, George Mason University, USA
Atalay, Selcuk, Inonu University, Turkey
Atghiaee, Ahmad, University of Tehran, Iran
Augutis, Vygantas, Kaunas University of Technology, Lithuania
Ayesh, Aladdin, De Montfort University, UK
Baliga, Shankar, B., Laser Components DG, Inc., USA
Barlingay, Ravindra, Larsen & Toubro - Technology Services, India
Basu, Sukumar, Jadavpur University, India
Bousbia-Salah, Mounir, University of Annaba, Algeria
Bouvet, Marcel, University of Burgundy, France
Campanella, Luigi, University La Sapienza, Italy
Carvalho, Vitor, Minho University, Portugal
Changhai, Ru, Harbin Engineering University, China
Chen, Wei, Hefei University of Technology, China
Cheng-Ta, Chiang, National Chia-Yi University, Taiwan
Cherstvy, Andrey, University of Potsdam, Germany
Chung, Wen-Yaw, Chung Yuan Christian University, Taiwan
Cortes, Camilo A., Universidad Nacional de Colombia, Colombia
D'Amico, Arnaldo, Università di Tor Vergata, Italy
De Stefano, Luca, Institute for Microelectronics and Microsystem, Italy
Ding, Jianning, Changzhou University, China
Djordjevich, Alexandar, City University of Hong Kong, Hong Kong
Donato, Nicola, University of Messina, Italy
Dong, Feng, Tianjin University, China
Erkmen, Aydan M., Middle East Technical University, Turkey
Fezari, Mohamed, Badji Mokhtar Annaba University, Algeria
Gaura, Elena, Coventry University, UK
Gole, James, Georgia Institute of Technology, USA
Gong, Hao, National University of Singapore, Singapore
Gonzalez de la Rosa, Juan Jose, University of Cadiz, Spain
Goswami, Amarjyoti, Kaziranga University, India
Guillet, Bruno, University of Caen, France
Hadjiloucas, Sillas, The University of Reading, UK
Hao, Shiying, Michigan State University, USA
Hui, David, University of New Orleans, USA
Jaffrezic-Renault, Nicole, Claude Bernard University Lyon 1, France
Jamil, Mohammad, Qatar University, Qatar
Kaniusas, Eugenijus, Vienna University of Technology, Austria
Kim, Min Young, Kyungpook National University, Korea
Kumar, Arun, University of Delaware, USA
Lay-Ekuakille, Aime, University of Lecce, Italy
Li, Fengyuan, HARMAN International, USA
Li, Jingsong, Anhui University, China
Li, Si, GE Global Research Center, USA
Lin, Paul, Cleveland State University, USA
Liu, Aihua, Chinese Academy of Sciences, China
Liu, Chenglian, Long Yan University, China
Liu, Fei, City College of New York, USA
Mahadi, Muhammad, University Tun Hussein Onn Malaysia, Malaysia
Mansor, Muhammad Naufal, University Malaysia Perlis, Malaysia
Marquez, Alfredo, Centro de Investigacion en Materiales Avanzados, Mexico
Mishra, Vivekanand, National Institute of Technology, India
Moghavvemi, Mahmoud, University of Malaya, Malaysia
Morello, Rosario, University "Mediterranea" of Reggio Calabria, Italy
Mulla, Imtiaz Sirajuddin, National Chemical Laboratory, Pune, India
Nabok, Aleksey, Sheffield Hallam University, UK
Neshkova, Milka, Bulgarian Academy of Sciences, Bulgaria
Pal, Jitendra, Carnegie Mellon University, USA
Passaro, Vittorio M. N., Politecnico di Bari, Italy
Patil, Devidas Ramrao, R. L. College, Parola, India
Penza, Michele, ENEA, Italy
Pereira, Jose Miguel, Instituto Politecnico de Setebal, Portugal
Pillarisetti, Anand, Sensata Technologies Inc, USA
Pogacnik, Lea, University of Ljubljana, Slovenia
Pullini, Daniele, Centro Ricerche FIAT, Italy
Qiu, Liang, Avago Technologies, USA
Reig, Candid, University of Valencia, Spain
Restivo, Maria Teresa, University of Porto, Portugal
Rodríguez Martínez, Angel, Universidad Politécnica de Cataluña, Spain
Sadana, Ajit, University of Mississippi, USA
Sadeghian Marnani, Hamed, TU Delft, The Netherlands
Sapozhnikova, Ksenia, D. I. Mendeleyev Institute for Metrology, Russia
Singhal, Subodh Kumar, National Physical Laboratory, India
Shah, Kriyang, La Trobe University, Australia
Shi, Wendian, California Institute of Technology, USA
Shmaliy, Yuriy, Guanajuato University, Mexico
Song, Xu, An Yang Normal University, China
Srivastava, Arvind K., Systron Donner Inertial, USA
Stefanescu, Dan Mihai, Romanian Measurement Society, Romania
Sumriddetchkajorn, Sarun, Nat. Electr. & Comp. Tech. Center, Thailand
Sun, Zhiqiang, Central South University, China
Sysoev, Victor, Saratov State Technical University, Russia
Thirunavukkarasu, I., Manipal University Karnataka, India
Thomas, Sadiq, Heriot Watt University, Edinburgh, UK
Tian, Lei, Xidian University, China
Tianxing, Chu, Research Center for Surveying & Mapping, Beijing, China
Vanga, Kumar L., ePack, Inc., USA
Vazquez, Carmen, Universidad Carlos III Madrid, Spain
Wang, Jiangping, Xian Shiyou University, China
Wang, Peng, Qualcomm Technologies, USA
Wang, Zongbo, University of Kansas, USA
Xu, Han, Measurement Specialties, Inc., USA
Xu, Weihe, Brookhaven National Lab, USA
Xue, Ning, Agiltron, Inc., USA
Yang, Dongfang, National Research Council, Canada
Yang, Shuang-Hua, Loughborough University, UK
Yaping Dan, Harvard University, USA
Yue, Xiao-Guang, Shanxi University of Chinese Traditional Medicine, China
Xiao-Guang, Yue, Wuhan University of Technology, China
Zakaria, Zulkarnay, University Malaysia Perlis, Malaysia
Zhang, Weiping, Shanghai Jiao Tong University, China
Zhang, Wenming, Shanghai Jiao Tong University, China
Zhang, Yudong, Nanjing Normal University China

Sensors & Transducers journal is an open access, peer review international journal published monthly by International Frequency Sensor Association (IFSA).
Available in both: print and electronic (printable pdf) formats.

Sensors & Transducers Journal

Contents

Volume 273
Issue 2
June 2026

www.sensorsportal.com

ISSN 2306-8515
e-ISSN 1726-5479

Research Articles

Authors are encouraged to submit article in MS Word (doc) and Acrobat (pdf) formats by e-mail: editor@sensorsportal.com. Please visit journal's webpage with preparation instructions: https://sensorsportal.com/sensors_and_transducers.html

12th International Conference on Sensors and Electronic Instrumentation Advances

https://www.seia-conference.com/

30 September - 2 October 2026
Granada, Spain

GRANADA
SEIA'26

IFSA

The XII International Conference on Sensors and Electronic Instrumentation Advances brings together researchers, innovators, and industry leaders to advance sensor science and electronic instrumentation by linking fundamental research, engineering practice, and real-world deployment. The conference provides a platform for presenting innovations that improve the measurement, monitoring, and control of complex systems in industry, environment, healthcare, mobility, energy, and smart infrastructure. Particular emphasis is placed on moving sensing technologies from prototypes to scalable, reliable applications. SEIA' 2026 welcomes original research papers, applied case studies, and technology demonstrations across diverse sensor types and modalities. Main topics include accuracy, calibration, uncertainty evaluation, reliability, validation in demanding environments, manufacturability, testing, interoperability, system integration, secure connectivity, and regulatory compliance. Through technical sessions and applied tutorials, the conference aims to strengthen the global sensing community and promote secure, interoperable, and standards-aware solutions with practical impact.

Sensor Technology

- Accelerometers
- Inclinometers
- Gyroscopes
- Mechanical Sensors
- Optical Sensors
- Optical Fiber Sensors
- Photonic Sensors
- Chemical Sensors
- Biosensors
- Immunosensors
- BioMEMS
- Temperature Sensors
- Pressure Sensors
- Acoustic Sensors
- Electromagnetic Sensors
- Gas Sensors
- Humidity Sensors
- Infrared Sensors, Devices and Thermography
- Radiation Sensors
- Multi Sensor Fusion
- Smart Sensors
- Intelligent Sensors
- Artificial Intelligence based Sensors and Sensor Systems
- Virtual Sensors
- Sensor Interfacing and Signal Conditioning
- Sensor Calibration
- Nanomaterials and Electronics Technology for Sensors
- Semiconductor Materials for Sensors
- Polymer Materials for Sensors
- MEMS and NEMS
- Remote Sensors and Telemetry
- Sensor Applications

Sensor Instrumentation and Measuring Technology

- Metrology and Measurement Science
- Methods of Measurements
- Calibrations and Standards
- Measurement of Electrical Quantities
- Time and Frequency Measurements
- Measurement of Force, Mass, Torque, Inclination and Acceleration
- Magnetic Measurements
- Hardness Measurements
- Measurement of Geometrical Quantities
- Temperature and Thermal Measurements
- Pressure and Vacuum Measurements
- Vibration and Noise Measurement
- Flow Measurements
- Chemical Measurements
- Quantum Measurements and Photonics
- Acoustics and the Ultrasonic Measurements
- Environmental Measurements
- Power and Energy Measurements
- Measurement of Human Functions
- Measurements in Biology and Medicine
- Mathematical Tools for Measurements
- Optical and Radiation Measurements
- Microwave Measurements
- Virtual Instruments and Data Acquisition Systems
- Soft Measurements
- Measurement Systems
- Distributed Measurements
- Analog-to-Digital Converters, Digital and Mixed Signal Processing
- Waveform Analysis and Measurements
- Scientific and Industrial Instrumentation
- Cyber-Physical Systems and IoT
- Experimental Mechanics
- Measurement in Robotics
- Metrology in Food and Nutrition
- Intelligent and Computer Vision Instruments
- Reliability of Instrument and Measurement Systems
- Nanometrology
- Technical Diagnostics and Testing
- Nondestructive Testing
- Blockchain Applications in Metrology and Measurements
- Education and Training in Measurement and Instrumentation

Special Sessions:

Authors are welcome to propose and manage special sessions during the SEIA' 2026. Each special session will contain 4-6 papers in a related field as specified above.

Session organizers will get: Certificate of Appreciation; Free Registration; Special Publishing Theme within Conference Proceedings.

Contribution Types:

- Keynote Presentations
- Invited Talks
- Special Sessions
- Regular Sessions
- Poster Sessions
- Special Sessions
- Online Sessions
- Exhibition

Deadlines:

Submission (2-page extended abstract):	**still open**
Notification of acceptance:	**in 2 weeks after submission**
Registration:	**25 July 2026**
Camera ready and late registration:	**30 August 2026**

12th International Conference on Sensors and Electronic Instrumentation Advances

GRANADA SEIA'26

https://www.seia-conference.com/

One event - three different publications !

1) All registered abstracts will be published in the conference proceedings (with the ISBN and DOI). Some previous SEIA Conference Series Proceedings are indexed in Conference Proceedings Citation Index (CPCI), Web of Science by Clarivate Analytics.

2) Authors will be invited to submit full-page extended papers to special issue of open access journal: Sensors & Transducers (ISSN: 2306-8515, e-ISSN: 1726-5479), published by IFSA Publishing (Barcelona, Spain), and indexed in Scopus and MDPI Sensors (ISSN 1424-8220) open access journal, published by MDPI AG (Basel, Switzerland). Impact factor: 3.5.

3) The papers, presented at SEIA' 2026 may be extended to open access book chapters for the Book Series on 'Advances in Sensors', Vol. 10, 'Advances in Biosensors', Vol. 4 or 'Advances in Measurements and Instrumentation', Vol. 3. Some previous Book Series volumes are indexed in the Book Citation Index (Wed of Science) by Clarivate Analytics.

Conference Hotel

The SEIA' 2026 Conference will be held in Barceló Granada Congress Hotel, Granada, Spain
Address: Calle Maestro Montero 12 18004 Granada Spain

Social Programme

- Welcome Cocktail: 29 September 2026 (20:00-21:30)
- Gala Dinner: 1 October 2026 (20:00-23:00)
- Farewell Cocktail: 2 October 2026, Friday (after lunch time)

Organizing Committee

Chairman
Prof., Dr. Sergey Y. Yurish (IFSA, Spain),
e-mail: seia@sensorsportal.com

Advisory Chairman
Prof. Vijyakumar Varadarajan
(Hano Technical University, Somalia)

Conference and Publication Manager
Tetyana Zakharchenko (IFSA Publishing, S.L., Spain)

Steering Committee:

Prof. Gennaro Conte (University Roma Tre, Italy)
Dr. Pavel Shuk (Saint-Gobain NorPro, USA)
Dr. Marius Gheorghe (Ideal Aerosmith, Inc., USA)
Dr. Paolo Dabove (Politecnico di Torino, Italy)
Prof. George Kiriakidis (European Materials Research Society (E-MRS), France)
Prof., Dr. Arkady Zhukov (Univ. of the Basque Country, Spain)

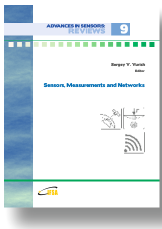


IFSA Publishing MDPI sensors an open access journal by MDPI


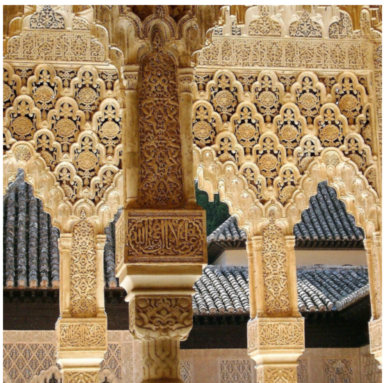

Sensors & Transducers
Published by IFSA Publishing, S. L., 2026
http://www.sensorsportal.com

A Simulation Study of Novel Piezo-MOS and Current Mirror Integrated Microbridge Mass Sensor for Low Mass Sensing Applications

[1,*] **Menuvolu TETSEO,** [1] **Kalpana GOGOI,** [1] **Gaurav KUMAR,**
[2] **Shashi KUMAR and** [1] **Pradeep Kumar RATHORE**
[1] Department of Electronics and Communication Engineering, National Institute of Technology Meghalaya, Sohra 793108, India
[2] Micron Technology Operation India LLP, Hyderabad, Telangana 500032, India
[*] E-mail: P21EC008@nitm.ac.in

Received: 26 Jan. 2026 /Revised: 20 March 2026 /Accepted:27 May 2026 /Published: 29 June 2026

Abstract: The article presents a MEMS microbridge integrated with two identical MOSFETs in a current mirror configuration. The input MOSFET, embedded on the substrate, serves as a reference MOSFET, while the output MOSFET is placed at the fixed edge of the microbridge to detect deflection-induced mechanical stress. Due to the piezoresistive effect, applied mass changes the channel mobility of the output MOSFET, resulting in changes in drain current and voltage across its drain terminals. Three microbridge-based sensing configurations are investigated: (a) pMOS channel resistive loaded, (b) nMOS channel resistive loaded and (c) dual channel current mirror integrated microbridge mass sensors. Simulation using COMSOL Multiphysics and TSpice software shows sensitivity of approx. 0.11 µV/µg, 2.33 µV/µg and 12.67 µV/µg for pMOS, nMOS and dual channel sensors, respectively. Fabrication process steps and mask-layout design are also discussed. Overall, this study demonstrates a promising and robust approach for highly sensitive low-mass sensing applications.

Keywords: Microelectromechanical systems, Piezoresistive devices, Current mirror circuit, Sensor systems.

1. Introduction

Over the years, a significant amount of research has been dedicated to Microelectromechanical System (MEMS) based biosensors [1-5]. A key area of focus within this research is the detection of small masses, particularly in the field of biomedical and chemical applications. Integrating sensors alongside a readout circuit on a single chip is highly preferable and instrumental in achieving high sensitivity and precision in detecting small masses. This integration can be facilitated by the CMOS-MEMS technology [6-13]. CMOS-MEMS enables seamless integration of the MEMS sensor with CMOS readout circuit, leading to improved performance, noise reduction, and various other benefits such as miniaturization, cost-effectiveness, reduced power consumption and rapid response times.

Mass sensors using MEMS structures such as diaphragm, microcantilever and microbridge have been reported by researchers worldwide [13-17]. The MEMS microbridge structure consists of a beam with two fixed edges and two free edges. When load is applied, the microbridge undergoes deflection and stress is induced at its fixed edges. This stress can be measured using different transduction solutions like piezoresistive [11], piezoelectric [18], capacitive [17], and optical transduction mechanism [19]. Each of these methods faces inherent limitations like temperature sensitivity, noise and nonlinearity when operated under adverse environmental conditions [20]. Recent years have seen the integration of FETs with

MEMS, where researchers have reported several studies exploiting the piezoresistive effect in MOSFETs [21–24]. This piezoresistive effect in silicon MOSFET arises due to distortion of energy band upon application of load. This distortion affects the effective mass, which in turn affects the electron and hole mobility, and hence its resistivity [25]. This piezo-MOS transduction mechanism is an inherent property of MOSFETs and remains relatively unexplored, leaving a significant scope for further investigation using CMOS circuit as sensor readout circuits.

In this context, one promising approach is the use of MOSFET-based current mirror as sensor readout circuit [24, 26–29]. While commonly used as biasing circuit, current mirrors have shown to offer several advantages when used as a readout circuit such as temperature compensation, seamless interfacing and full CMOS compatibility. This eliminates the need for complex ΔR/R measurements and additional temperature compensation circuit, unlike other works reported in the literature [30–32]. Prior studies have demonstrated the efficiency of this approach in pressure sensors [26–29], and most recent work demonstrated cantilever-based piezo-MOS sensing under tip loading [24]. In the present study, the same sensing concept is applied to a microbridge structure under central loading, introducing a different mechanical boundary condition. This changes the governing equations and stress distribution, with symmetric stress generated at both fixed edges, resulting in a distinct electromechanical response.

From the literature [33], microbridge structures offer advantages over microcantilevers due to their double-clamped configuration, including better mechanical stability, lower sensitivity to residual fabrication stress, easier sensing-layer deposition, and improved MEMS integration. They also exhibit higher resonant frequency and mass sensitivity. While microcantilevers are preferred for large deflection and very low mass sensing, microbridges are suitable for applications requiring higher stability and larger mass range. However, the present work is limited to a proof-of-concept study on integrating a microbridge structure with a MOSFET sensing element and a current mirror readout circuit for low-mass sensing applications, focusing only on the static behavior of the sensor under constant mass-loading conditions.

2. Design and Modelling

2.1. Physical Structure and Working Principle

The proposed mass sensor consists of a microbridge beam as its mechanical mass sensing element. This study introduces three different mass sensor configurations, shown in Fig. 1: (a) resistive loaded p-channel MOSFET based current mirror integrated mass sensor, (b) resistive loaded n-channel MOSFET based current mirror integrated mass sensor, (c) dual channel MOSFET current mirror integrated mass sensor. In the p-channel and n-channel sensors, two identical MOSFETs are arranged in a resistive loaded current mirror configuration. These sensors consist of one reference MOSFET (Mp1/Mn1) positioned on the substrate and one stress sensing MOSFET (Mp2/Mn2) placed on one fixed edge of the bridge. Resistors are connected to the drain terminals of both the reference and output MOSFET branches to provide resistive loading. The dual channel mass sensor consists of four MOSFETs, with Mp1 and Mn1 serving as reference MOSFETs, while Mp2 and Mn2 act as stress sensing MOSFETs. The current mirror circuits were designed using the 5 μm CMOS technology parameters given in Table 1. These parameters were selected to analyze the proposed circuit under long-channel operating conditions, where current mirror behavior and stress-induced mobility variation can be examined without additional complexity from advanced device scaling effects.

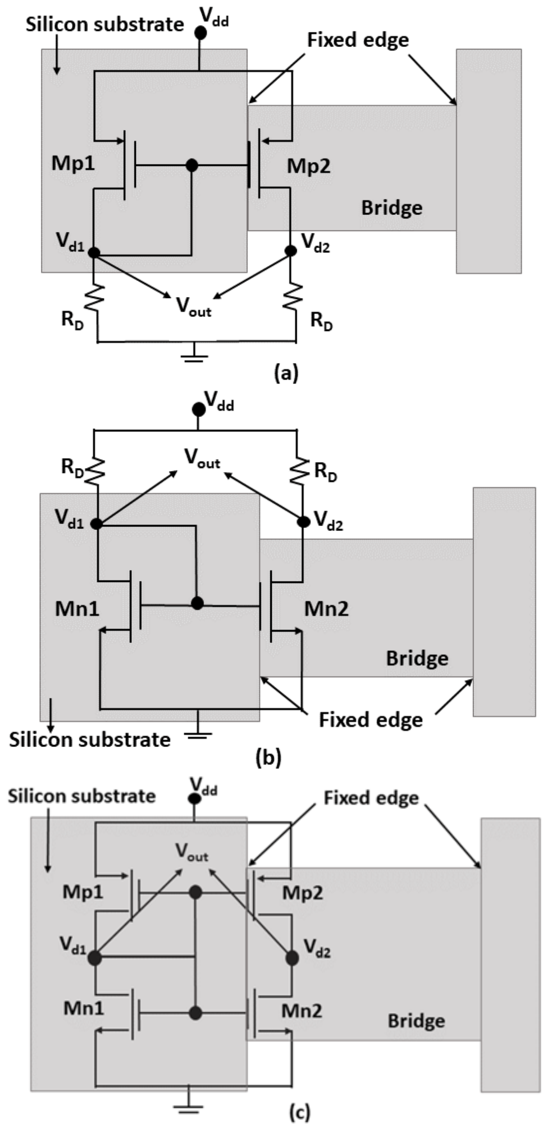

Fig. 1. (a) pMOS channel resistive loaded; (b) nMOS channel resistive loaded, and (c) dual channel current mirror integrated microbridge mass sensors.

Table 1. Parameters of 5 µm CMOS technology [34].

Parameters	p-MOSFET	n-MOSFET
Mobility (cm²/Vs)	250	750
Threshold voltage (V)	-1	1
Thickness of gate oxide (nm)	85	85
Supply voltage (V)	10	10
Oxide capacitance (fF/µm²/Vs)	0.406	0.406
Early voltage (V/ µm)	6.67	20
Transconductance (µA/V²)	10.15	30.45

The cross-sectioned view of the proposed bridge sensor under no-load and applied load condition is illustrated in Fig. 2. Upon applying mass load, the bridge undergoes deflection, inducing stress at its fixed edges. This leads to a change in mobility of the output MOSFET (Mp2/Mn2), and consequently its drain voltage and current, while the mobility of the reference MOSFET (Mp1/Mn1) remains the same and unaffected by load. The output voltage corresponding to external load can be calculated between the drain terminals of the reference MOSFET M1 and output MOSFET M2. In all three sensor configurations, the reference MOSFET is diode-connected, establishing the gate bias for the corresponding sensing transistor.

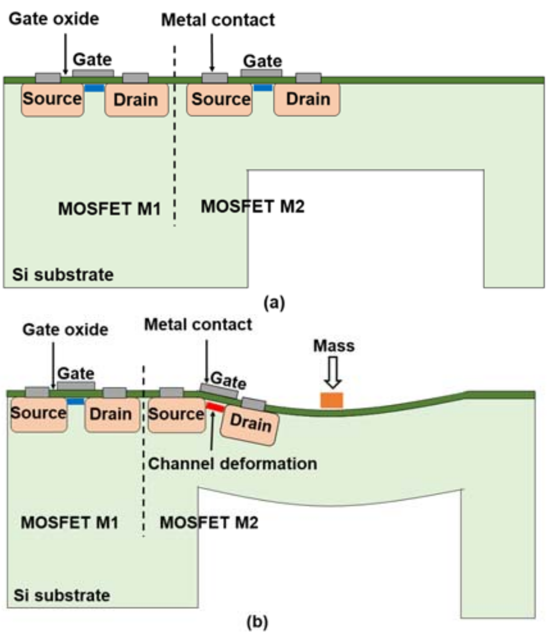

Fig. 2. The cross-sectional view of the microbridge sensor under: (a) no load condition and (b) applied load condition.

2.2. Theoretical Model

a) Micromechanical Element: Microbridge

The proposed sensor incorporates a silicon microbridge with its dimension parameters given in Table 2. The maximum displacement (W_{max}) and stress (T_{max}) for the bridge under load conditions are given in equations 1 and 2 [35].

$$W_{\max} = \frac{Mg}{Ebh^3} x^2 \left(\frac{3}{2} a_1 - x\right), \quad (1)$$

$$T_{\max} = \frac{3a_1}{2bh^2} Mg , \quad (2)$$

where b and h are breadth and height of bridge, E is the Young's modulus, M represents central mass of the bridge, x is the original position of the beam and a_1 is the distance of the central mass from the fixed ends of the bridge.

Table 2. Parameters used to design and simulate the proposed current mirror bridge based mass sensors.

Parameters	p-MOSFET	n-MOSFET
MOSFET Channel length and width	Length = 10 µm Width = 20 µm	
Microbridge dimension (Length, breadth, height)	(200, 100, 5) µm	
Drain resistor (R_D)	11.94 kΩ	17.73 kΩ
Resistance of MOSFET piezoresistor	197.92 kΩ	593.46 kΩ
Piezoresistive coefficient (10^{-12} Pa^{-1})	π_{11} = -66 π_{12} = 11 π_{44} = -1380	π_{11} = 1020 π_{12} = -534 π_{44} = 136
Mass load	In range of 0 to 100 µg, with step size of 10 µg	

b) Transduction Mechanism

The proposed sensor uses the piezoresistive effect in MOSFET as the transduction mechanism. As reported in a previous work [26], the pMOS and nMOS are designed as a simple piezoresistor where its resistance is equal to MOSFET's channel resistance ($R_{ch} = r_o = V_A/I_D$). [25] reported that under externally applied load, the mobility changes alone create a drain current change of the MOSFET. Hence, the carrier mobility and corresponding drain currents of both the pMOS and nMOS under load condition are given as

$$\frac{\Delta\mu_p}{\mu_p} = \frac{\Delta\mu_n}{\mu_n} = \frac{\Delta R_{ch}}{R_{ch}} = -\pi\sigma , \quad (3)$$

$$I_{Dp} = (\mu_p \pm \Delta\mu_p) C_{ox} \frac{W}{L} \frac{(V_{SG} - V_{tp})^2}{2} , \quad (4)$$

$$I_{Dn} = (\mu_n \pm \Delta\mu_n) C_{ox} \frac{W}{L} \frac{(V_{GS} - V_{tn})^2}{2} , \quad (5)$$

where μ denotes the carrier mobility, $\Delta\mu$ is the change in carrier mobility under applied load, π is the piezoresistive coefficient, while σ is the stress developed in the MOSFET channel region. L and W denote channel length and width respectively, C_{ox} is the oxide capacitance per unit area. V_{GS} is the gate-to-source voltage, while V_{tp} and V_{tn} represent the threshold voltages of the p- and n-channel MOSFETs, respectively.

c) Readout Circuit

The output voltage corresponding to external load can be calculated between the drain terminals of the reference MOSFET M1 and the output MOSFET M2

$$V = V_{DS1} - V_{DS2} = -\pi\sigma I_{D1} R_D, \quad (6)$$

where V_{DS1} and V_{DS2} represent drain-to-source voltages of MOSFET M1 and M2, respectively.

All the MOSFETs were biased to operate in the saturation region. The mathematical model of the readout circuit has been described and explained in [24, 26].

3. Simulation Results

COMSOL Multiphysics was employed to simulate the mass sensing bridge structure while the analysis of the electrical behavior of the current mirror circuit was done using TSpice simulation tool. The parameters employed for simulations are given in Table 2. The simulation starts with the construction of a 3D mass sensing bridge structure integrated with strain sensing MOSFET equivalent piezoresistors. Subsequently, the material properties, mechanical and electrical boundary conditions, and meshing of the sensor structure were defined. Input voltages corresponding to the threshold voltages of the pMOS and nMOS transistors were applied across their respective equivalent piezoresistors. Mass load was then applied to the bridge structure, and simulations were conducted to analyze the piezoMOS behavior of the proposed mass sensors. Fig. 3 and Fig. 4 illustrate the maximum displacement and stress profiles of the microbridge structure obtained from COMSOL Multiphysics. Under a load of 100 µg, the microbridge structure undergoes a maximum deflection of 0.207 nm at the center and maximum stress of 65.3 kPa at the fixed edges.

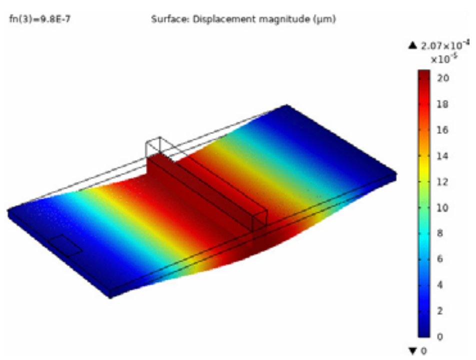

Fig. 3. Displacement profile of a microbridge structure under 100 µg load.

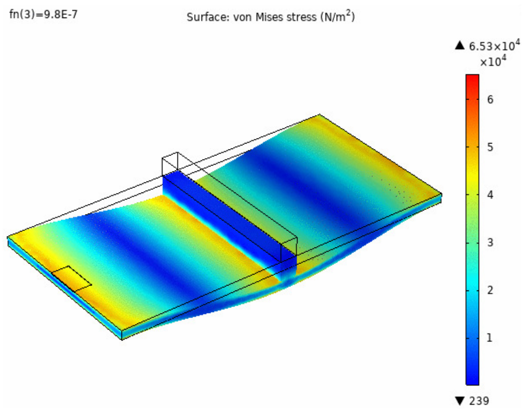

Fig. 4. Stress profile of a microbridge structure under 100 µg load.

The variations in channel resistance and mobility were obtained. These mobility values were subsequently used in TSpice simulation tool to determine the drain currents and voltages of the current mirror readout circuit. In order to study the effect of thickness of MOSFET equivalent piezoresistor, simulation was performed for five piezoMOS thicknesses for both pMOS and nMOS. Under an input load of 100 µg, pMOS and nMOS equivalent piezoresistors gives a change of (0.00088, 0.00086, 0.00079, 0.00079, 0.00072) cm^2/Vs and (0.0331, 0.0320, 0.0309, 0.0285, 0.0267) cm^2/Vs in its channel mobilities for piezoMOS thickness of (0.1, 0.25, 0.5, 0.75, 1) µm, respectively. Fig. 5 and Fig. 6 show the variations in channel mobility and resistance of pMOS and nMOS equivalent piezoresistors, respectively, with different values of piezoMOS thickness. The results showed that mobility and resistance changes are higher with smaller piezoMOS thickness. However, simulation of structures with one dimension significantly smaller than the others may result in meshing and convergence issues [36]. Therefore, piezoMOS thickness of 0.5 µm was selected for this study [26].

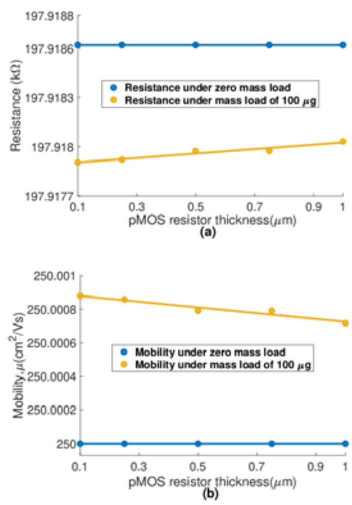

Fig. 5. Plot of: (a) channel resistance and (b) channel mobility with respect to resistor thickness of pMOS.

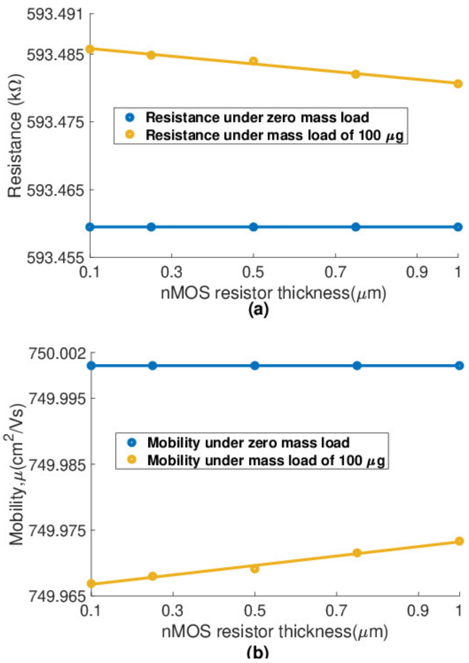

Fig. 6. Plot of: (a) channel resistance and (b) channel mobility with respect to resistor thickness of nMOS.

A mesh convergence analysis using nine mesh sizes was conducted to evaluate simulation accuracy, with results summarized in Table 3. The output voltage plot with respect to the number of meshing elements is given in Fig. 7. The graph shows that the voltage output starts to saturate after 'coarse' mesh size, meaning any mesh size ranging from 'coarse' to 'extremely fine' produced convergent result. Hence, we have conducted this study with 'finer' mesh size, which lies within the range of converged result, affirming its accuracy.

Table 3. Results from meshing analysis.

Meshing size	**No. of meshing elements**	**Output voltage (µV)**	**% variation in output voltages**
Extremely coarse	444	150	-
Extra coarse	944	220	46.667
Coarser	1630	220	0
Coarse	3135	230	4.545
Normal	6370	230	0
Fine	13704	230	0
Finer	19863	230	0
Extra fine	32511	230	0
Extremely fine	77173	230	0

When mass is loaded on the bridge beam, it results in a change of channel resistance and channel mobility of all three mass sensors. The piezoMOS effect, described by [25], was used to study channel resistance and mobility change. Fig. 8 (a-c) show the channel resistance change for the pMOS, nMOS and dual channel mass sensors with varying load, respectively. Under a 100 µg load, the pMOS sensor showed a reduction of approx. 0.6 Ω, nMOS sensor showed an increase of approx. 24.5 Ω, while dual mass sensor showed a decrease of approx. 0.6 Ω and enhancement of approx. 24.6 Ω for its pMOS and nMOS equivalent resistor, respectively.

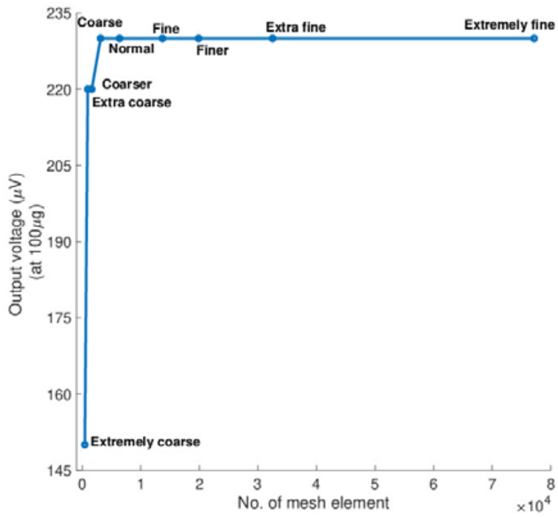

Fig. 7. Graph of output voltage with respect to number of mesh elements.

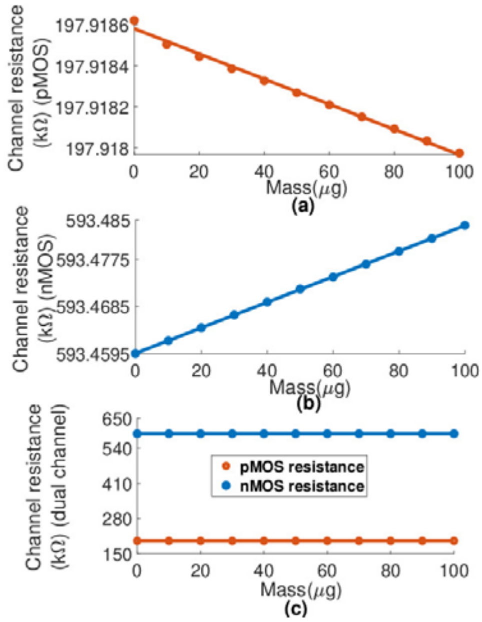

Fig. 8. Graph of channel resistance vs mass for: (a) pMOS, (b) nMOS and (c) dual channel mass sensor.

Fig. 9 (a-c) show the change in the channel mobility for the pMOS, nMOS and dual channel mass sensors, respectively. Under 100 µg load, the pMOS experiences an increase of approx. 0.0008 cm^2/Vs while the nMOS undergoes a decrease of approx. 0.0309 cm^2/Vs. The dual sensor showed an increase of approx. 0.0008 cm^2/Vs and a decrease of approx. 0.0311 cm^2/Vs for the pMOS and nMOS, respectively. This channel mobility obtained from COMSOL Multiphysics was then used in TSpice simulation tool to calculate the electrical properties of the mass sensors. The reference MOSFETs remains independent of load applied, while output MOSFETs acts as a function of external load. Therefore, drain currents and voltages of the output MOSFETs will change under load, while those of reference MOSFETs remain the same. Under 100 µg load, the pMOS experience an increase of 0.001 µA in its drain current while the nMOS and dual channel mass sensors show a reduction of approximately 0.01 µA in its drain current. This variation in the drain current is shown in Fig. 10 (a-c).

Fig. 11 (a-c) illustrate the drain voltage change of the three sensors under varying mass load. An increase in the drain voltage of approx. 0.00005 V, 0.00023 V and 0.00127 V was noted for the pMOS, nMOS and dual channel mass sensors, respectively. The plots of differential output voltage proportional to the input mass load for pMOS, nMOS, and dual channel mass sensors are depicted in Fig. 12 (a-c). The pMOS, nMOS and dual channel mass sensors give a sensitivity of 0.11 µV/µg, 2.33 µV/µg, and 12.67 µV/µg, respectively.

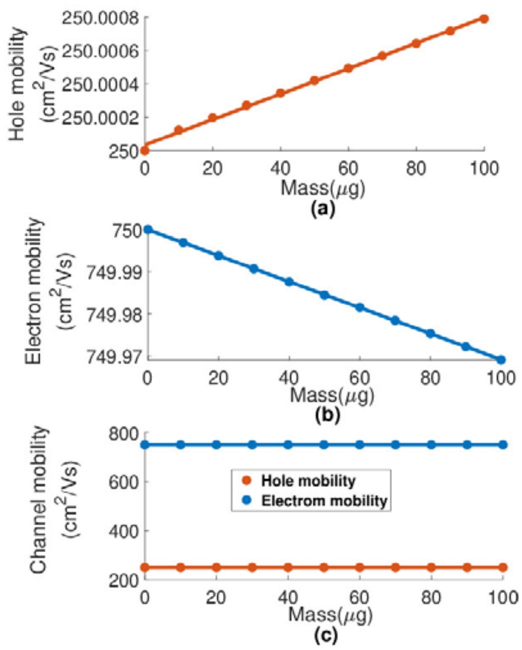

Fig. 9. Graph of channel mobility vs mass for: (a) pMOS, (b) nMOS and (c) dual channel mass sensor.

The higher sensitivity of dual channel sensor over the other two sensors can be attributed to the fact that the dual sensor incorporates two sensing elements, while pMOS and nMOS mass sensor have only one sensing element. In addition, the higher sensitivity of nMOS over pMOS mass sensor is due to the piezoresistive effect. It has been reported that devices with n-type show better piezo resistivity in both longitudinal and transverse direction as compared to p-type device [37]. Table 4 summarizes the electrical parameters of both the reference and output MOSFET for each sensor configuration under a 100 µg load.

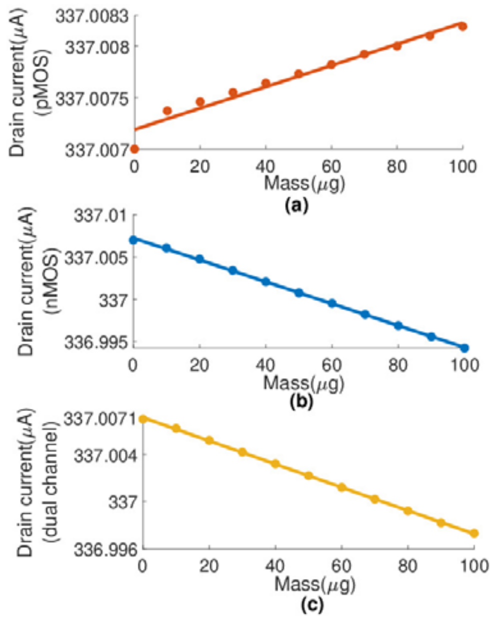

Fig. 10. Graph of drain current vs mass for: (a) pMOS, (b) nMOS and (c) dual channel mass sensor.

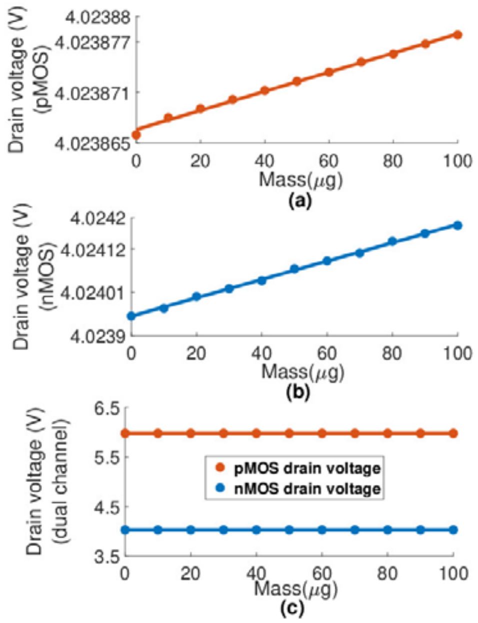

Fig. 11. Graph of drain voltage with respect to mass for: (a) pMOS, (b) nMOS and (c) dual channel mass sensor.

Additional performance metrics including noise, limit of detection (LOD), resolution, and linearity were calculated for all three sensor configurations. Noise was evaluated using the Johnson–Nyquist relation [38] based on the equivalent MOSFET channel resistance. At 300 K for 1 Hz bandwidth, the calculated RMS noise voltages are 57.3 nV for the pMOS sensor, 99.3 nV for the nMOS sensor, and 114.6 nV for the dual-channel sensor. The corresponding LOD values are 1.56 µg, 0.128 µg, and 0.027 µg, respectively. The estimated resolutions are 0.52 µg, 0.043 µg, and 0.009 µg for the pMOS, nMOS, and dual-channel sensors, respectively. Linearity is assessed by linear regression of output voltage versus applied mass, yielding R^2 values of 0.9959, 0.9987, and 0.9999 for the pMOS, nMOS, and dual-channel sensors, respectively. These results demonstrate excellent linearity across the entire sensing range.

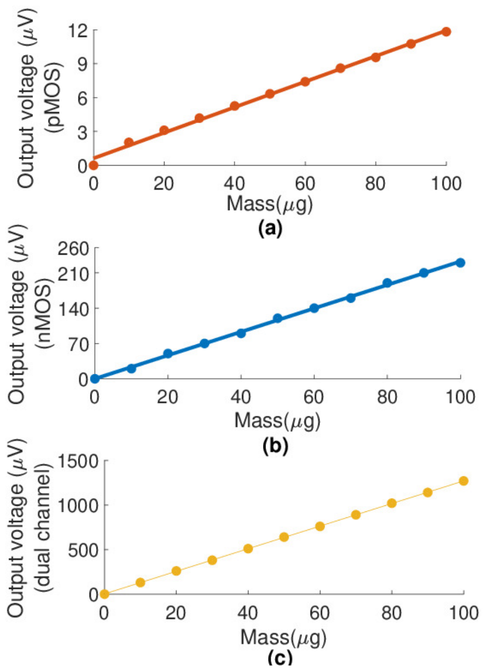

Fig. 12. Graph of output voltage with respect to mass for: (a) pMOS, (b) nMOS and (c) dual channel mass sensor.

To further evaluate temperature stability, the sensors are simulated at temperatures of 300 K, 325 K, and 350 K. Table 5 summarizes the corresponding electrical characteristics for all three sensor configurations under a load of 100 µg. The results show that channel resistance, mobility, and drain voltages vary with temperature across all three sensors. However, the calculated sensitivities remain stable over the investigated temperature range. This occurs because both the reference and sensing MOSFETs undergo similar temperature-dependent variations in their device parameters. Consequently, the current mirror output largely cancels these common shifts, providing inherent temperature compensation within the simulated range.

The proposed fabrication process flow of the pMOS mass sensor is shown in Fig. 13. The process starts with dry oxidation on an RCA-cleaned silicon wafer to grow the field oxide (Fig. 13 (a)). The first lithography step patterns the source-drain regions (Fig. 13 (b)), followed by source-drain doping (Fig. 13 (c)). Subsequently, another lithography process defines the gate oxide region (Fig. 13 (d)), followed by the growth of gate oxide (Fig. 13 (e)). A third lithography process patterns the contact vias (Fig. 13 (f)), while the fourth lithography process forms the metal lines and contact pads (Fig. 13 (g)), followed by metallization and the lift-off process (Fig. 13 (h)). The front side of the wafer is then coated with photoresist to protect the circuit (Fig. 13 (i)). The backside window is then patterned by the fifth lithography step, followed by DRIE etching of backside silicon (Fig. 13 (j)). Subsequently, the front side of the bridge structure is defined using a sixth lithography step, followed by DRIE etching of silicon to release the structure (Fig. 13 (k)). Finally, removal of photoresist from both top and bottom layers (Fig. 13 (l)) completes the fabrication of the sensor. The fabrication process flow is largely similar for all three sensors, with the pMOS and nMOS designs consisting of six lithography steps whereas the dual channel sensor requires eight lithography steps, two additional lithography needed for the formation of the P/N well and source/drain regions.

Table 6 also shows the sensitivity comparison of our sensors with that of several reported work in literature. These comparisons show that our bridge sensors achieve comparable and even superior performance relative to existing design, including cantilever-based structures, which are typically more sensitive than bridge configurations. The higher sensitivity reported in [37] is attributed to its multi-beam array structure. In contrast, the proposed single-beam bridge sensor achieves comparable performance with lower structural complexity and simpler CMOS integration.

Further work was done to study the effect of bridge thickness on sensor sensitivity. Five different bridge thicknesses (1, 2, 3, 4 and 5) µm were simulated, and the results show that lower thickness leads to higher sensitivity, as shown in Table 7. This is because thinner bridge structures exhibit lower stiffness and undergo greater deflection under the same applied load, resulting in larger output variation. However, extremely thin structures may introduce fabrication complexities, increased fragility during mass loading, and reduced structural robustness during handling and operation. This highlights the need for a tradeoff between sensitivity, structural reliability and fabrication complexity in sensor design.

4. Conclusion

This study investigates CMOS-MEMS integrated mass sensors with three different configurations. Among them, the dual-channel sensor demonstrated the highest sensitivity of 12.67 µV/µg, significantly outperforming the pMOS and nMOS sensors with sensitivities of 0.11 µV/µg and 2.33 µV/µg, respectively. In addition to superior performance, the dual-channel sensor also offers the advantages of being fully CMOS-compatible and does not require any external component. Comparison with previously reported sensors shows that our sensors are comparable, and in some cases, outperforms existing works including cantilever-based sensors, which are typically considered more sensitive but are fragile and less stable than bridge structures. The effect of microbridge thickness on sensor sensitivity was also examined. The fabrication process steps for the sensor were also presented. Future works will focus on sensor fabrication and experimental characterization of the proposed sensors.

Table 4. Electrical parameters of the proposed current mirror mass sensors under 100 µg load.

Parameters	p-channel MOSFET mass sensor		n-channel MOSFET mass sensor		Dual channel mass sensor	
	M1	M2	M1	M2	M1	M2
Gate to source voltage, V_{GS} (V)	5.976	5.976	4.024	4.024	5.976	5.976
Drain current, I_D (µA)	337.007	337.008	337.007	336.994	337.007	336.997
Drain to source voltage, V_{DS} (V)	4.02395	4.02396	4.02395	4.02418	5.97605	5.97478
Output voltage, V_{out} (µV)	$(V_{DS1} - V_{DS2}) = 10$		$(V_{DS1} - V_{DS2}) = 230$		$(V_{DS1} - V_{DS2}) = 1270$	

Table 5. Variation of electrical parameters and sensitivity of the proposed sensors with temperature under 100 µg.

Sensor type	Temperature (K)	Channel resistance (kΩ)	Mobility (cm²/Vs)	Drain voltage (V1)	Drain voltage (V2)	Sensitivity (µV/ µg)
p-channel MOSFET mass sensor	300 K	197.9433	249.9687	4.02376	4.02377	0.1
	325 K	198.0341	249.8540	4.02308	4.02309	0.1
	350 K	198.1223	249.7427	4.02242	4.02243	0.1
n-channel MOSFET mass sensor	300 K	592.9951	750.5868	4.02297	4.02320	2.3
	325 K	591.21	752.8428	4.01939	4.01962	2.3
	350 K	589.4231	755.1010	4.01582	4.01605	2.3
Dual channel mass sensor	300 K	197.9452	249.9663	5.97711	5.97585	12.6
	325 K	198.0392	249.8476	5.98093	5.97967	12.6
	350 K	198.1247	249.7397	5.9847	5.98344	12.6

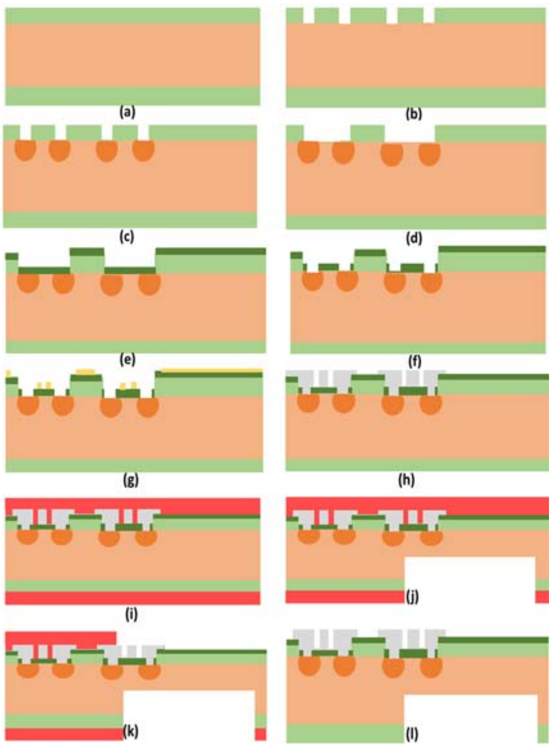

Fig. 13. Fabrication process flow of pMOS mass sensor.

Table 6. Comparison of proposed sensors with other works reported in literature.

Type of work	Sensitivity (µV/µg)	Ref.
Simulation and experimental	18.87	[39]
Simulation and experimental	0.515	[40]
Experimental	0.024	[41]
Experimental	0.219	[42]
Experimental	5.299	[43]
Simulation	0.11 (pMOS) 2.33 (nMOS) 12.67 (dual)	This work

Table 7. Effect of bridge thickness on sensor sensitivity.

Thickness of bridge (µm)	Sensor sensitivity (µV/µg)		
	pMOS	nMOS	Dual channel
1	1.44	32.13	173.99
2	0.55	12.04	65.44
3	0.24	6	32.41
4	0.14	3.55	19.21
5	0.11	2.33	12.67

Acknowledgements

The authors acknowledge the National Institute of Technology Meghalaya for providing institute overhead funds from the DRDO-sponsored project (Ref: DFTM/07/3603/DIA-CoE,MZU/MEMS/P-03) for the payment of publication fees. The authors also acknowledge the use of a high-end desktop computer purchased under the ISRO-sponsored project (Ref: ISRO/RES/3/807/18-19) for carrying out the simulations reported in this work.

References

[1]. A. C. R. Grayson, R. S. Shawgo, A. M. Johnson, N. T. Flynn, et al., A BioMEMS review: MEMS technology for physiologically integrated devices, *Proceedings of the IEEE*, Vol. 92, Issue 1, 2004, pp. 6-21.

[2]. F. Khoshnoud, C. W. de Silva, Recent advances in MEMS sensor technology–biomedical applications, *IEEE Instrumentation & Measurement Magazine*, Vol. 15, Issue 1, 2012, pp. 8-14.

[3]. Y. Pandey, S. P. Singh, Recent advances in bio-MEMS and future possibilities: An overview, *Journal of The Institution of Engineers (India): Series B*, Vol. 104, Issue 6, 2023, pp. 1377-1388.

[4]. G. S. Lakshmi, S. R. Karumuri, P. A. Sridhar, J. Akhtar, et al., Design and performance analysis of a microbridge and microcantilever-based MEMS pressure sensor for glucose monitoring, *IEEE Sensors Journal*, Vol. 23, Issue 5, 2023, pp. 4589-4596.

[5]. C. Chircov, A. M. Grumezescu, Microelectro-mechanical systems (MEMS) for biomedical applications, *Micromachines*, Vol. 13, Issue 2, 2022, 164.

[6]. P. Amiri, Z. Kordrostami, M. N. S. Ashkezari, Design of a MEMS bionic vector hydrophone with piezo-gated MOSFET readout, *Microelectronics Journal*, Vol. 98, 2020, 104748.

[7]. C. L. Dai, P. H. Kao, M. C. Liu, C. C. Wu, et al., Micro FET pressure sensor manufactured using CMOS-MEMS technique, *Microelectronics Journal*, Vol. 39, Issue 5, 2008, pp. 744-749.

[8]. H. Baltes, O. Brand, A. Hierlemann, D. Lange, et al., CMOS MEMS-present and future, in *Proceedings of the 15th IEEE International Conference on Micro Electro Mechanical Systems (MEMS)*, 2002, pp. 459-466.

[9]. H. H. Tsai, C. F. Lin, T. P. Sun, C. P. Jiang, et al., Multiple type biosensors fabricated using the CMOS BioMEMS platform, *Sensors and Actuators B: Chemical*, Vol. 144, Issue 2, 2010, pp. 407-412.

[10]. Y. K. Yen, C. Y. Chiu, A CMOS MEMS-based membrane-bridge nanomechanical sensor for small molecule detection, *Scientific Reports*, Vol. 10, Issue 1, 2020, 2931.

[11]. A. A. Zope, J. H. Chang, M. C. Lin, C. H. Chen, et al., A CMOS-MEMS thermal-piezoresistive oscillator for mass sensing applications, *IEEE Transactions on Electron Devices*, Vol. 67, Issue 3, 2020, pp. 1183-1191.

[12]. Y. C. Lee, M. L. Hsieh, Y. C. Chou, C. H. Cheng, et al., CMOS-MEMS technologies for the applications of environment sensors and environment sensing hubs, *Journal of Micromechanics and Microengineering*, Vol. 31, Issue 7, 2021, 074004.

[13]. G. Vidal-Álvarez, E. Marigó, J. J. Sánchez, A. Uranga, et al., Fabrication and measurement of a suspended nanochannel microbridge resonator monolithically integrated with CMOS readout circuitry, *Micromachines*, Vol. 7, Issue 3, 2016, 40.

[14]. Z. J. Davis, W. Svendsen, A. Boisen, Design, fabrication and testing of a novel MEMS resonator for mass sensing applications, *Microelectronic Engineering*, Vol. 84, Issue 5-8, 2007, pp. 1601-1605.

[15]. Z. Hu, J. Hedley, C. McNeil, Design, fabrication and characterization of a piezoelectric MEMS diaphragm resonator mass sensor, *Journal of Micromechanics and Microengineering*, Vol. 23, Issue 12, 2013, 125019.

[16]. P. Joshi, S. Kumar, M. M. Hossain, M. T. Lemaire, et al., Distributed MEMS mass-sensor based on piezoelectric resonant micro-cantilevers, *Journal of Microelectromechanical Systems*, Vol. 28, Issue 3, 2019, pp. 382-389.

[17]. M. U. Nathani, H. Nazemi, P. Hashemi, Capacitive based micromachined resonators for low level mass detection, *Micromachines*, Vol. 12, Issue 1, 2020, 13.

[18]. K. Meinel, C. Stoeckel, C. Weiss, S. Sorge, et al., Piezoelectric scanning micromirror with built-in sensors based on thin film aluminum nitride, *IEEE Sensors Journal*, Vol. 21, Issue 8, 2020, pp. 9682-9689.

[19]. R. M. Pinto, P. Brito, T. I. B. Marques, J. P. Conde, et al., Thin-film silicon MEMS for dynamic mass sensing in vacuum and air: Phase noise, Allan deviation, mass sensitivity and limits of detection, *Journal of Microelectromechanical Systems*, Vol. 28, Issue 3, 2019, pp. 390-400.

[20]. S. Beeby, MEMS Mechanical Sensors, *Artech House*, Norwood, 2004.

[21]. G. Shekhawat, S. H. Tark, V. P. Dravid, MOSFET-embedded microcantilevers for measuring deflection in biomolecular sensors, *Science*, Vol. 311, Issue 5767, 2006, pp. 1592-1595.

[22]. E. L. Gardner, A. De Luca, F. Udrea, Thin-film MOSFET-based pressure sensor, *IEEE Sensors Letters*, Vol. 3, Issue 7, 2019, pp. 1-4.

[23]. P. Singh, J. Miao, G. Li, C. S. Premachandran, et al., Microcantilever sensors with embedded piezoresistive transistor read-out: Design and characterization, *Sensors and Actuators A: Physical*, Vol. 171, Issue 2, 2011, pp. 178-185.

[24]. M. Tetseo, K. Gogoi, S. Kumar, A conceptual study on novel current mirror integrated cantilever (CMIC) mass sensor for micro-gram (µg) range sensing applications, *Microsystem Technologies*, Vol. 30, Issue 3, 2024, pp. 263-275.

[25]. A. T. Bradley, R. C. Jaeger, J. C. Suhling, K. J. O'Connor, Piezoresistive characteristics of short-channel MOSFETs on (100) silicon, *IEEE Transactions on Electron Devices*, Vol. 48, Issue 9, 2001, pp. 2009-2015.

[26]. P. K. Rathore, B. S. Panwar, J. Miao, C. C. Keng, A novel CMOS-MEMS integrated pressure sensing structure based on current mirror sensing technique, *Microelectronics International*, Vol. 32, Issue 2, 2015, pp. 81-95.

[27]. S. Kumar, P. K. Rathore, G. D. Ropmay, P. B. Gogoi, et al., Development of a current mirror-integrated pressure sensor using CMOS-MEMS cofabrication techniques, *Microelectronics International*, Vol. 35, Issue 4, 2018, pp. 203-210.

[28]. S. Kumar, G. D. Ropmay, B. S. Panwar, Fabrication and testing of PMOS current mirror-integrated MEMS

pressure transducer, *Sensor Review*, Vol. 40, Issue 2, 2020, pp. 141-151.

[29]. S. Kumar, G. D. Ropmay, B. S. Panwar, Design and simulation of a novel dual current mirror based CMOS-MEMS integrated pressure sensor, *IET Science, Measurement & Technology*, Vol. 15, Issue 3, 2021, pp. 268-278.

[30]. Y. J. Huang, C. W. Huang, F. C. Ku, M. C. Lin, et al., A CMOS cantilever-based label-free DNA SoC with improved sensitivity for hepatitis B virus detection, *IEEE Transactions on Biomedical Circuits and Systems*, Vol. 7, Issue 6, 2013, pp. 820-831.

[31]. K. W. Li, Y. K. Yen, Gentamicin drug monitoring for peritonitis patients by using a CMOS-BioMEMS-based microcantilever sensor, *Biosensors and Bioelectronics*, Vol. 130, 2019, pp. 420-426.

[32]. Y. K. Yen, C. Y. Lai, Portable real-time detection of Pb (II) using a CMOS MEMS-based nanomechanical sensing array modified with PEDOT: PSS, *Nanomaterials*, Vol. 10, Issue 12, 2020, 2454.

[33]. S. Shin, N. E. Lee, J. S. Park, S. S. Lee, et al., Piezoelectrically driven microtransducer mass sensors, *Integrated Ferroelectrics*, Vol. 80, Issue 1, 2006, pp. 355-362.

[34]. A. S. Sedra, K. C. Smith, Microelectronic Circuits (5th Ed.), *Oxford University Press*, New York, 2004.

[35]. M. Bao, Analysis and Design Principles of MEMS Devices, *Elsevier*, Amsterdam, 2005.

[36]. G. Cadet, M. Paredes, Convergence analysis and mesh optimization of finite element analysis related to helical springs, *Mechanics & Industry*, Vol. 25, 2024, 22.

[37]. T. Nguyen, T. Dinh, A. R. M. Foisal, M. T. Phan, et al., Advances in ultrasensitive piezoresistive sensors: From conventional to flexible and stretchable applications, *Materials Horizons*, Vol. 8, Issue 8, 2021, pp. 2123-2150.

[38]. H. Nyquist, Thermal agitation of electric charge in conductors, *Physical Review*, Vol. 32, Issue 1, 1928, pp. 110-113.

[39]. S. Liu, D. F. Wang, X. B. Chen, Highly sensitive mass sensing scheme via energy relocalization with a coupled three-beam array, *IEEE Sensors Journal*, Vol. 22, Issue 19, 2022, pp. 18400-18408.

[40]. J. Wei, S. Magnani, A. Rastegar, Suspended submicron silicon-beam for high sensitivity piezoresistive force sensing cantilevers, *Sensors and Actuators A: Physical*, Vol. 186, 2012, pp. 80-85.

[41]. M. Ahmed, M. M. Chitteboyina, S. Bhattacharya, MEMS force sensor in a flexible substrate using nichrome piezoresistors, *IEEE Sensors Journal*, Vol. 13, Issue 10, 2013, pp. 4081-4089.

[42]. D. Grech, A. Tarazona, P. G. R. Smith, S. P. Beeby, et al., A quasi-concertina force-displacement MEMS probe for measuring biomechanical properties, *Sensors and Actuators A: Physical*, Vol. 275, 2018, pp. 67-74.

[43]. T. C. Duc, J. Creemer, P. M. Sarro, Piezoresistive cantilever beam for force sensing in two dimensions, *IEEE Sensors Journal*, Vol. 7, Issue 1, 2007, pp. 96-104.

Published by International Frequency Sensor Association (IFSA) Publishing, S. L., 2026 (http://www.sensorsportal.com).

Sensors & Transducers, Vol. 273, Issue 2, June 2026, pp. 11-20

Sensors & Transducers

Published by IFSA Publishing, S. L., 2026
http://www.sensorsportal.com

An Intelligent Hybrid Analog–Digital Signal Conditioning Architecture for Automatic Multi-Sensor Temperature Recognition and Control

[1] Rawia Khalaf AL-KHAWALDEH, [1, *] Mohammed KHRAISAT, [1, 2] Tariq M. YOUNES, [2] Mohammad Tariq NASIR, [2] Osama NASHWAN

[1] Department of Mechatronic Engineering, Al-Balqa Applied University. Al-Salt, 19117, Jordan
[2] Electrical Engineering Department, Faculty of Engineering and Technology,
Applied Science Private University, Amman, Jordan
[1] Tel.: +962770356185
E-mail: mkhrisat@bau.edu.jo

Received: 13 Jan. 2026 /Revised:26 March 2026 /Accepted: 8 June 2026 /Published: 29 June 2026

Abstract: Temperature sensing is fundamental in various engineering applications, including industrial automation, HVAC systems, and biomedical instrumentation. Accurate temperature measurement requires signal-conditioning circuits to process the low-level, often nonlinear outputs of different types of temperature sensors. Traditional designs typically require manual wiring and predefined circuits for each sensor type, limiting flexibility and increasing complexity. This article presents the design and implementation of an integrated smart signal conditioning circuit based on a microcontroller. The system autonomously identifies the type of connected temperature sensor whether it is an NTC, PTC, RTD, or thermocouple by analyzing its resistance value and surrounding temperature. Once identified, the system automatically routes the sensor to the appropriate analog signal-conditioning path. Thermocouple signals are amplified using an AD620 instrumentation amplifier (gain ≈ 207.5) before analog-to-digital conversion, while RTD measurements are acquired through a precision voltage-divider interface and processed using a linear temperature-resistance model. This hybrid analog–digital architecture enables flexible multi-sensor integration without relying on dedicated digital converter modules. The proposed system significantly reduces the need for manual sensor configuration and wiring, allowing for adaptive interfacing and real-time measurement. Experimental validation and simulation (Proteus) demonstrate the reliability and accuracy of the system under various conditions. This work paves the way for intelligent, reconfigurable temperature sensing interfaces suited for future Internet of Things (IoT) and industrial applications.

Keywords: Microcontroller, Temperature sensor, Signal conditioning.

1. Introduction

Integrated solutions based on microcontrollers are gaining popularity in the conditioning of temperature sensor signals, as they offer a compact and flexible approach compared to discrete component designs [1, 2, 13]. These solutions typically provide an analog-to-digital converter (ADC) to convert the analog signal from the sensor to digital form, processing power to plan the sensor response, calibration management, and compensation for environmental effects [3, 4]. Furthermore, they often include standard communication interfaces (such as SPI or I2C), which facilitate the transfer of temperature data to other system components [5]. This integration reduces the space required on the circuit board, simplifies the design process, lowers the overall cost, and enhances accuracy and reliability with digital signal processing algorithms [6, 7, 11]. Although temperature sensors (platinum resistance, thermistors, and thermocouples) are widely used in industrial, medical, and environmental applications [8, 9, 20], their direct readings typically require dedicated signal conditioning circuits for each type to ensure compatibility with microcontroller inputs [10]. Based on this identification, the system automatically routes the sensor to the optimal analog signal conditioning circuit (amplification, filtering, compensation) and/or activates the appropriate digital processing algorithm within the microcontroller [14, 15]. This automatic switching mechanism is achieved using a programmable switching system or analog switches, eliminating the need for manual re-connection or hardware modification [16]. The main hypothesis of the research is that it is possible to reliably identify the type of temperature sensor through its resistance value and ambient temperature, thereby activating the optimal signal-conditioning path without manual intervention. To achieve this, the study will follow a mixed methodology that includes theoretical analysis of the working principles of sensors [17, 18] and signal conditioning [19]. This research contributes by providing a practical framework that simplifies the integration of multiple types of temperature sensors into electronic and digital systems, which is consistent with the requirements of sustainable and flexible electrical design. The proposed system is expected to have wide applications in industrial monitoring systems, heating, ventilation, and air conditioning (HVAC) systems, and sensor networks for the Industrial Internet of Things [12].

2. System Design and Implementation

This study presents the design and implementation of an intelligent system for conditioning temperature sensor signals based on an integrated microcontroller (Arduino Mega 2560). The system aims to achieve automatic recognition of the type of connected sensor (NTC/PTC thermistor, Pt100 platinum precision resistor, K-type thermocouple) and select the optimal signal-conditioning path without manual intervention, thereby increasing the flexibility and accuracy of measurement and control systems. The design was first validated through comprehensive simulation using Proteus 8 Professional software, followed by practical implementation and performance testing.

2.1. Design Methodology and Architecture

The system is based on a hybrid analog-digital architecture (Fig. 1). Dedicated analog signal conditioning circuits (voltage divider, instrumentation amplifier) condition the raw signal from the sensor, while the microcontroller handles the digital tasks: sensor recognition, dynamic calibration, computational processing of readings, and implementation of a closed-loop PID control algorithm to control the heating element.

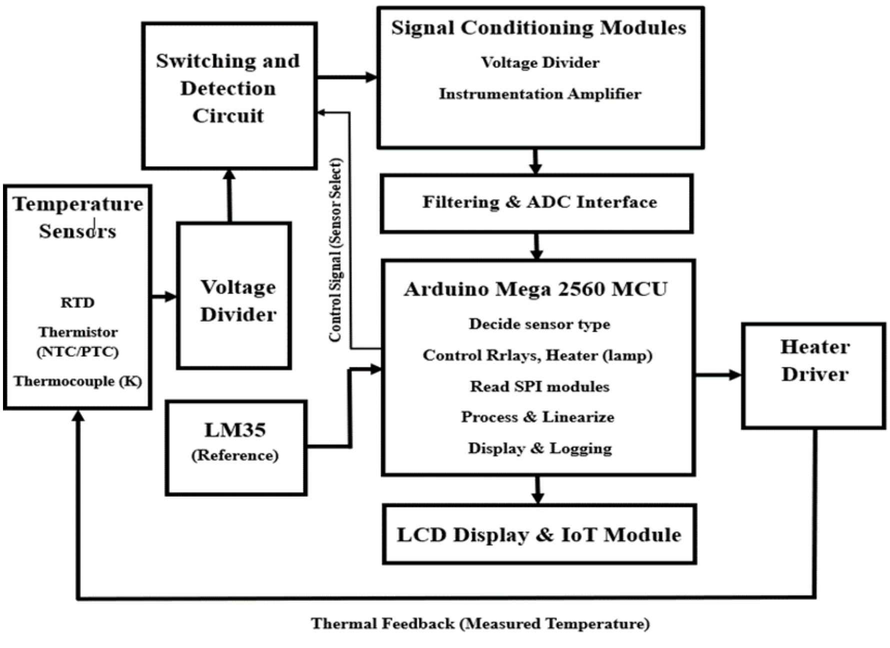

Fig. 1. Block diagram of the proposed system.

2.2. Analog Design and Signal Conditioning

2.2.1. Switching and Isolation Circuit

To ensure signal isolation and reduce power consumption, electromagnetic relays (SPST) are used for electrical isolation of the resistive sensors (NTC, PTC, and RTD). Each relay is operated via an NPN transistor (BC547) by a signal from the microcontroller, with diodes (1N4148) used to suppress the reverse voltage generated by the relay coils (Fig. 2).

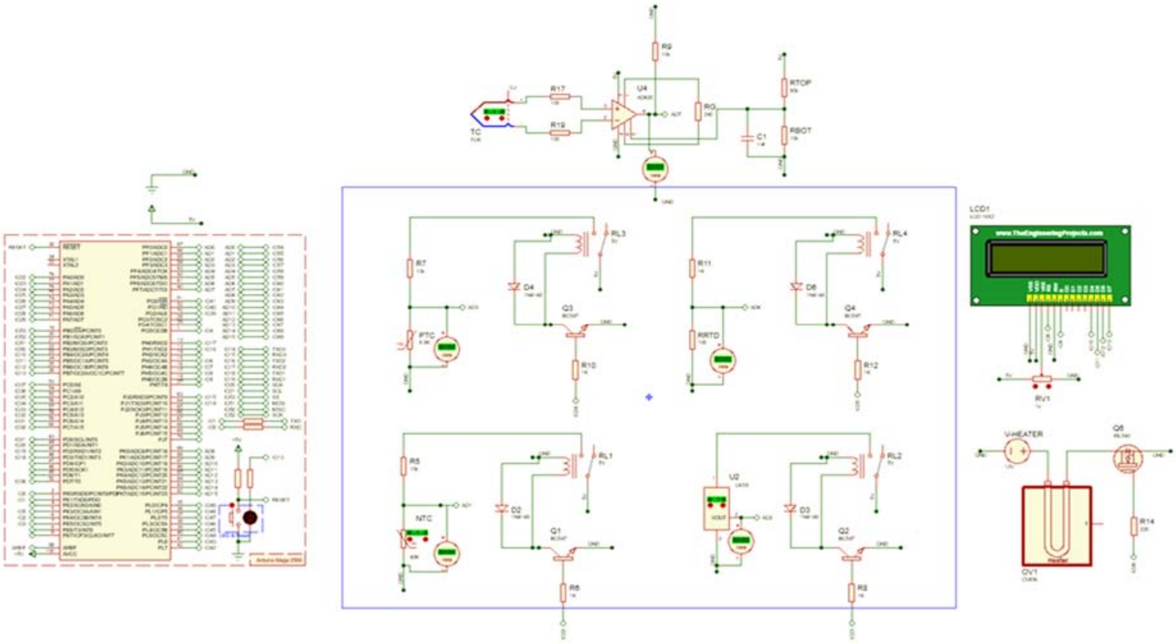

Fig. 2. Relay operating circuit using a BC547 transistor.

2.2.2. Thermocouple Signal Conditioning

Due to the low output voltage of the thermocouple (~41 microvolts/°C), an instrumentation amplifier (AD620) was used to boost the signal level. The amplifier gain (~207.5 times) was adjusted using an external resistor (240 ohms) to convert the thermocouple voltage range (0–30 millivolts) to a range suitable for the controller's analog-to-digital converter input (0–5 volts), Equation (1), Fig. 3.

$$G = 1 + \frac{49.4K\Omega}{Rg}, \quad (1)$$

where G is the gain of the instrumentation amplifier (dimensionless), R_g is the external gain-setting resistor (in ohms or kΩ), 49.4 kΩ is an internal factory-trimmed gain resistance value (in kilo-ohms) specific to the AD620 architecture.

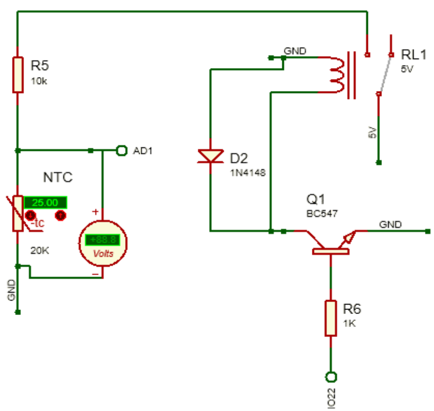

Fig. 3. Thermocouple signal conditioning circuit using an AD620 amplifier.

2.2.3. Reference Calibration Sensor

An LM35 sensor (with an accuracy of 10 mV/°C) is integrated as a standard reference for on-site calibration. The sensor is only activated during the calibration process via a dedicated relay, which reduces the effect of self-heating and provides an independent reference reading to compensate for offset errors of the active sensor.

2.3. Software Design and Algorithms

2.3.1. Automatic Sensor Recognition Algorithm

The algorithm sequentially activates the relays (each for 70 ms) and reads the corresponding output voltage. The sensor type is determined by comparing the measured value (ADC) that reflect the characteristic electrical properties of each type (Fig. 4).

2.3.2. Voltage-to-Temperature Conversion Model

Various mathematical models were implemented within the program: NTC thermistor: A beta (β) model was used to derive the temperature from the resistance. Pt100 platinum resistance: A linear approximation (0.385 Ω/°C) was used. Thermocouple: Calculation of temperature from amplified voltage using the Sea beck coefficient, with compensation for cold junction temperature (assumed to be 25 °C).

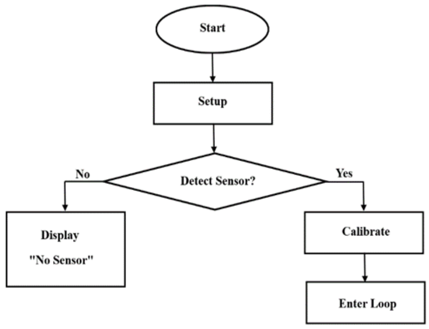

Fig. 4. Flowchart of the sensor recognition algorithm.

2.3.3. PID Control Algorithm

A digital proportional-integral-derivative (PID) controller was implemented to control a heating element via a PWM signal. The output signal (u (t)) is calculated based on the error (e(t)) between the desired and measured temperatures, Equation (2).

$$u(t) = K_p e(t) + K_i \int e(t)dt + K_d \frac{de(t)}{dt}, \quad (2)$$

where u(t) is the control signal (output of the controller), e(t) is the error signal (setpoint – measured variable), K_p is a proportional gain, K_i is an integral gain, K_d is a derivative gain, t is a time, τ is the dummy integration variable, K_p=40.0, K_i=0.3, K_d=20.0. The coefficients (K_p=40.0, K_i=0.3, K_d=20.0) were set experimentally to obtain a fast response with reduced overshoot.

2.4. Simulation and Verification Results

The complete system simulation in Proteus verified the basic functions:

1. Sensor recognition: The system accurately identified the type of sensor connected and displayed it on the LCD screen;
2. Dynamic calibration: The system calculated and compensated for an offset of +0.6 °C between the RTD reading and the LM35 reference reading;
3. Temperature control: The closed PID control loop maintained the temperature at the set point (30 °C) with remarkable stability, as the PWM duty cycle of the heating element is regulated in response to deviations (Fig. 5);
4. Signal integrity: All conditional signals remained within the safe range of the analog-to-digital converter inputs (0–5 V) with no interference between channels.

2.5. Practical Implementation and Performance Tests

The work presents an integrated system that solves the complexity associated with using multiple types of temperature sensors. The automatic recognition and calibration mechanism reduces the effort required for reconfiguration and increases the overall accuracy of the system. The results show that integrating custom analog signal conditioning with intelligent digital processing in a single microcontroller is a practical and cost-effective approach. This paves the way for industrial Internet of Things applications where flexibility and interoperability are critical. An intelligent signal conditioning system based on a microcontroller has been successfully designed and implemented. The system demonstrates the ability to automatically recognize different types of temperature sensors, perform on-site calibration using a reference sensor, and maintain precise temperature control via a PID algorithm. The solution combines the simplicity of integrated architecture with the flexibility of software configuration, making it a promising solution for a wide range of industrial and research applications.

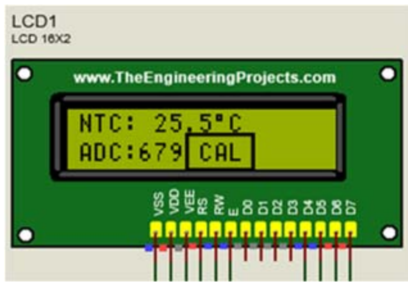

Fig. 5. Temperature response in the simulation showing PID control at a specific point (30 °C).

3. Results and Discussion

3.1. Experimental Validation Methodology

The performance of the proposed multi-sensor temperature control system was validated through comprehensive simulation using the Proteus Design Suite (v8.13), which provides virtual system modeling for physical components. The simulated platform included an Arduino Mega 2560 microcontroller and models of diverse thermal sensors: NTC and PTC thermistors, an RTD (Pt100), a K-type thermocouple, and an LM35 as a reference. A systematic experimental protocol was designed to test each system layer sequentially: automatic sensor detection, in-situ self-calibration, measurement, and closed-loop control using a Proportional-Integral-Derivative (PID) algorithm.

3.2. Sensor Performance and Automatic Detection

The system demonstrated high reliability in the automatic detection of the connected sensor type within 0.5 seconds of startup, utilizing an algorithm based on predefined analog input voltage thresholds. To prevent electrical crosstalk, each resistive sensor (NTC, PTC, RTD) was isolated using a dedicated SPST electromagnetic relay (RL1, RL3, RL4), which was activated only during its measurement cycle. Conversely, the thermocouple was permanently connected via an AD620 instrumentation amplifier with a gain of 207.5. The results for each sensor type, following the in-situ calibration routine using the LM35 reference, are detailed below. The calibration successfully compensated for component tolerances and simulation-specific offsets, ensuring high measurement accuracy (Fig. 6).

Table 1. Summary of system performance for each sensor type (accuracy, range, response time).

Block	Function
Temperature Sensors	Measure Temperature
Voltage Divider	Conditioning the signal output from the sensors to ensure it falls within a range appropriate for the MCU, converting the resistance or thermal signal into a voltage that can be easily interpreted.
Switching and Detection Circuit	Detects the connected sensor type based on voltage or resistance and switches the signal path to the corresponding conditioning circuit.
Signal Conditioning Modules	Enhancement, Selection, and Linear Transformation of the signal obtained from the sensors to guarantee precise accuracy in the measurements.
Arduino Mega 2560 MCU	Central unit for reading signals, performing calibration, and controlling heater via PWM, and transistor data to the display and Internet of Things (IoT).
LCD Display & IoT Module	Displays readings and supports external monitoring.
LM35 (Reference Sensor)	Used for temperature calibration and comparison.
Heater Driver	Controls the heater's on/off operation based on microcontroller (MCU) commands, which are received from sensors, the PID controller, and the PWM interface.
Filtering & ADC Interface	Filters noise and sends conditioned analog signals to the microcontroller's ADC input.

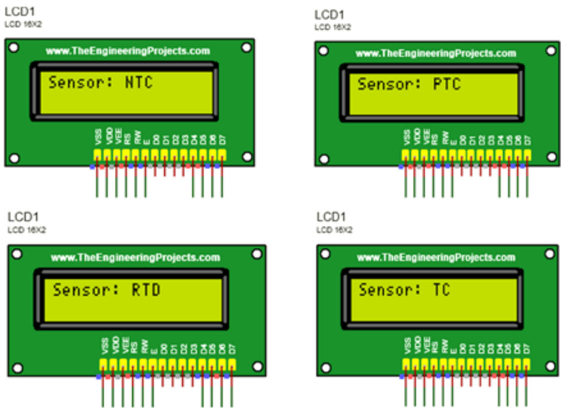

Fig. 6. Sensor Detection Success across All Types.

3.2.1 NTC Thermistor Results

The NTC interface, utilizing the Beta-parameter equation (β=3950), achieved a measurement accuracy within ±0.2 °C across the 20–40 °C test range after calibration (Table 2). The signal chain –from the voltage divider output through ADC conversion to the final temperature calculation –showed excellent agreement with theoretical expectations, confirming the robustness of the chosen model for the operational range (Fig. 7).

The analog input A1 was connected to the NTC thermistor with a nominal resistance of 20k ohm at 25 °C and a voltage divider with a 10k ohm resistance in series with the thermistor. The processed volume was recorded at the ADC of the Arduino, and the Beta-parameter model was employed by the firmware to calculate the temperature. The results of the experiment in the entire operation range are presented in Table 2 and relate the actual temperature, the output voltage, ADC value, and the temperature measured after the calibration of the LM35-based calibration.

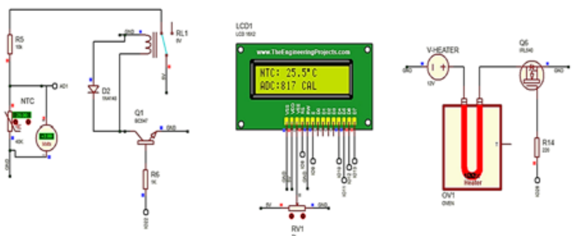

Fig. 7. The operational circuit with RL1 in a closed state, the NTC linked to A1, the LCD display indicating "NTC: 25.5 °C CAL", and the heater activated.

The results have shown that the NTC interface circuit, with the conversion algorithm of the firmware and the calibration process, is remarkably accurate (within the range of ±0.2 °C) across the entire test range. The fact that the minor fixed offset is added to the code (+0.12 °C) is an additional correction of minor mismatches at the simulation level, thus providing maximum consistency to the reference.

Table 2. A Result NTC Sensor Data from Proteus Simulation.

True Temp (°C)	R_{NTC} $(K\Omega)$	V_{out} (V)	Measured Temp (°C)
20.0	28.22	3.48	20.1
25.0	20.00	3.31	25.5
30.0	14.90	2.98	30.2
35.0	11.39	2.63	35.1
40.0	8.85	2.31	40.2

3.2.2. PTC Thermistor Results

Using a linear approximation model (temperature coefficient α=0.0075/°C), the PTC subsystem also maintained an accuracy of approximately ±0.2 °C within the 20–40 °C range (Table 3). This confirms the adequacy of a linear model for the limited temperature span of this application, while acknowledging that a more complex model would be necessary for wider operational ranges (Fig. 8).

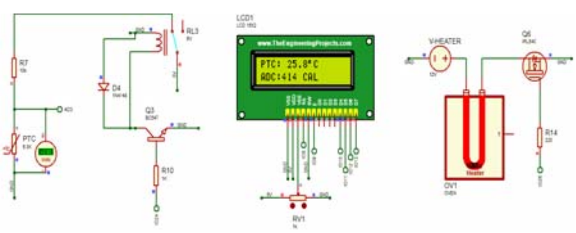

Fig. 8. The operational circuit with RL3 in a closed state, the PTC linked to A3, the LCD display indicating "PTC: 25.8 °C CAL", and the heater activated.

The data in Table 3 supports the idea that the PTC interface depicts the effectiveness of the linear model within the identified range of operations (20–40 °C). Beyond this range, the nonlinear properties of the PTC would demand a more advanced model, but at the parameters of this system, the chosen methodology can be proven efficient and accurate.

Table 3. A Result PTC Sensor Data from Proteus Simulation.

True Temp (°C)	R_{PTC} $(K\Omega)$	V_{out} (V)	Measured Temp (°C)
20.0	6.61	1.97	20.1
25.0	6.80	2.02	25.8
25.8	6.83	2.03	26.1
30.0	6.99	2.07	30.2
35.0	7.16	2.11	35.1
40.0	7.33	2.15	40.2

3.2.3. RTD (Pt100) Results

The RTD interface demonstrated high precision, with errors within ±0.2 °C across a broader range of 0–100 °C when using a linear conversion model (Table 4). The inherent linearity of the Pt100 sensor makes this approach both efficient and accurate for precision applications within this system's scope [22].

Table 4. A Result RTD Sensor Data from Proteus Simulation.

True Temp (°C)	R_{RTD} (Ω)	V_{out} (V)	Measured Temp (°C)
0.0	100	0.452	0.9
20.0	107.8	0.507	25.5
25.0	109.5	0.515	26.0
30.0	111.6	0.525	30.9
50.0	119.4	0.559	50.8
75.0	129.0	0.599	77.1
100.0	138.5	0.638	99.2

Table 4 and Fig. 9 confirm that RTD interface is accurate (±0.2 °C) within the operational range up to 100, which proves that the linear model is applicable to the desired operational range (0-100 °C). The linearity of Pt100 RTD is very high and therefore it is especially applicable in precision applications and the adopted strategy is efficient and accurate.

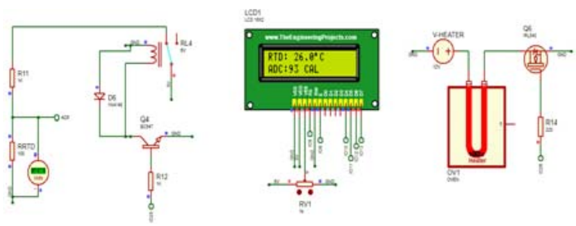

Fig. 9. The RTD subcircuit with RL4 closed, the voltage at AD6 measured as 0.45 V, and the LCD displaying “RTD: 26.0 °C CAL”, confirming successful detection, calibration, and measurement.

3.2.4. K-Type Thermocouple Results

Despite the thermocouple's low output signal (~41 µV/°C); the AD620 amplifier stage enabled reliable measurement. After applying cold-junction compensation (25 °C) and a software calibration offset (*tc_offset*), the system achieved an accuracy within ±0.3 °C in the 20–50 °C range (Table 5 and Fig. 10).

The K-type thermocouple generates a See beck voltage of approximately 41 µV/°C. To make this signal measurable by the Arduino’s 10-bit ADC, it is amplified using an AD620 instrumentation amplifier with a gain of 207.5 times, set by a 240 Ω resistor. The amplified signal is connected directly to analog input A7. The firmware computes temperature from the amplified voltage using the See beck coefficient and a fixed cold-junction compensation of 25 °C. Table 5 presents the experimental data across the operational range, correlating true temperature, amplified voltage, ADC value, and measured temperature after LM35-based calibration.

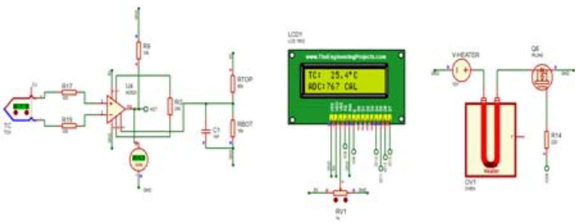

Fig. 10. Thermocouple Operational State in Proteus Simulation.

Table 5. A Result Thermocouple Data from Proteus Simulation.

True Temp (°C)	V_{AMP} (V)	Measured Temp (°C)
20.0	2.80	21.1
25.0	3.45	25.4
26.0	3.74	26.2
30.0	4.20	30.1
50.0	5.50	50.3

However, this discrepancy is resolved by the calibration offset (tc_offset) applied in the code, which compensates for the difference between the theoretical and simulated behavior, ensuring zero steady-state error.

3.3. Discussion of Engineering Challenges and Solutions

Several key challenges were overcome during the design: Preventing interference between sensors: Solved using a time-shifting strategy based on relays, which electrically isolates each sensor when not in use. Amplification of weak thermocouple signals: Solved using an instrumentation amplifier (AD620) with precisely calculated gain to raise the signal level to the appropriate range for the analog-to-digital converter. Nonlinearity in the response of some sensors: Addressed by implementing appropriate mathematical models (such as the beta equation for NTC) in the firmware. Precise heating control: Avoided the use of bang-bang control in favor of PWM technology using MOSFETs, which enabled smooth proportional control and better PID performance.

3.4. Comparison of Performance to Conventional System

Performance of the proposed system was compared to those of conventional single-sensor temperature control systems, which are usually present in laboratories and industries in order to assess the innovation and practical value of the proposed system. It contains a comparison of five main aspects such as sensor flexibility, ability to calibrate, precision of control, efficiency in development and system intelligence.

Table 6. Performance Comparison between Proposed System and Conventional Approaches.

Feature	Conventional system	Proposed system
Sensor support	Single sensor type (only lm35 or only thermocouple)	Multi-sensor support**:** NTC, PTC, RTD, k-type Thermocouple, LM35
Sensor detection	Manual configuration required	Automatic detection via relay-based switching and software logic
Calibration	Factory calibration only; no in-situ adjustment	Real-time in-situ calibration using LM35 as reference
Control strategy	On/off control (relay-based)	Proportional PID control via MOSFET (IRL540) and PWM
Accuracy	±1.0 °C to ±2.0 °C (no correction)	±0.3 °C or better after calibration
Development workflow	Hardware prototype, firmware test, iteration	Full co-simulation in proteus (firmware validated before physical build)
User feedback	Basic led or no display	Real-time LCD showing sensor type, temperature, ADC value, and calibration status
Scalability	Fixed functionality	Modular architecture, easy to add new sensors or actuators

Multi-Sensor Intelligence: Traditional systems would need manual rewiring and change of code when using other types of sensors. The suggested system, in contrast, recognizes the attached sensor automatically and sets the acquisition and processing chain to suit the sensor [21], getting rid of the human error and improving the usability. Dynamic Calibration: Unlike many low-cost systems, which use factory calibration (which drifts with time), this system uses live calibration on an LM35 reference during start. This counterbalances component tolerances, aging and environmental variations, making it accurate in the long term. High-quality Thermal Control: Designs that are more conventional retain the use of electromechanical relays to control heaters, and this leads to ON/OFF (bang-bang) behavior with oscillations of ±2-3 °C. The suggested system is based on PWM-controlled MOSFET that allows efficient power regulation and minimization of steady-state error to < ±0.3 °C. Simulation to Implementation Workflow: Proteus enables full simulation of both circuit and firmware allowing a significant reduction in development time and cost. Wiring, Logic, or Time errors are also identified early as compared to the traditional methods, which would require physical prototyping to verify their validity. Improved Diagnostic Capacity: The LCD offers detailed operating information that is invaluable in debug and verification capabilities not implemented in simple temperature controllers [20]. Limitations and Trade-offs: Flexibility and accuracy are more important to the system than ultra-low cost, since it requires a relay, an instrumentation amplifier (AD620) and a microcontroller with several analog inputs. The calibration procedure presupposes ambient conditions at start up (cold-junction compensation at 25 °C), which can be sources of small error in harsh conditions. However, in educational, laboratory, and mid-precision industrial applications, the proposed system provides a substantial improvement of flexibility, stability, and user-friendliness to the traditional single-purpose temperature regulators.

3.7. Problems Experienced and Engineering Relies

The design of a single multi sensor temperature control system in a simulated environment posed many interconnected problems of a certain engineering nature. These were analog circuit design, sensor physics, microcontroller interfacing and real-time control logic. The combination of hardware innovation and firmware intelligence was used to solve each challenge and produced a unified and functionally sound virtual prototype. The increasing number of analog sensors all attached to the same microcontroller was one of the major challenges in ensuring that there was no cross-interference between them. Assuming that all sensors were left constantly powered, their voltage divider networks would be loaded between each other, biasing ADC readings and doing away with accuracy. To address this, a time division-multiplexing strategy implemented a relay based strategy. All resistive sensors – NTC, PTC and RTD – are interconnected with respective SPST electromagnetic relay (RL1, RL3 and RL4, respectively). Digital pin pins 22, 24 and 25 of the Arduino Mega 2560 through BC547 NPN transistors, drive these relays. The firmware only activates one of the relays during operation with a short window of 70ms to stabilize the circuit before reading the ADC value. This will guarantee electrical isolation, crosstalk removal, and will allow effective automatic sensing detection.

The second major challenge was the very low production output voltage of the K-type thermocouple that produces approximately 41 μV per degree Celsius. These signals are many times less than the resolution of the 10-bits ADC that is available on the Arduino (which has a minimum step of about 4.88 mV). Hard connection would give insignificant readings. The answer was to combine an AD620 instrumentation amplifier with a 240 Ω in the gain-setting position with 240 gain-setting resistor, which gave an approximate 207.5 gain. This converts the thermocouple signal to 0–5 V range that can be converted to ADC. Another capacitor, 1 μF at the amplifier output, additional filters the noise at the high frequency, and signals are stored. The thermocouple always has a connection unlike the switched sensors since the AD620 has a high input impedance and buffering ability.

Another impeding factor was the nonlinear characteristics of the temperature sensors. An example is the NTC thermistor whereby the resistance-temperature relationship is exponential and cannot be represented by simple linear models. The firmware responds to this by using a simplified version of the Steinhart-Hart equation, the Beta-parameter equation, to plot resistance versus temperature within the operating range. On the other hand, PTC sensor was represented through a linear approximation with the temperature coefficient (α = 0.0075/°C), supplemented by small empirical offsets (+0.12 °C for NTC, +0.37 °C for PTC, etc.) to correct for residual discrepancies observed in simulation.

Another source of error that was expected was component tolerances and system drift. A small variation in reference resistors or ADC offset can add up to serious temperature errors. In response to this, an in-situ calibration mechanism was created whereby the LM35 IC sensor was used as a constant reference. When starting up, when the sensor is detected, the system briefly switches relay RL1 to energize the LM35 and measures its temperature which is automatically accurate at ±0.5 °C and then measures the active sensor and calculates an offset correction. This compensation is also retained and used in all the next measurements, and the hardware imperfections are corrected. To provide actuator control, a basic choice was to eliminate the usual habit of using a relay to switch the heater, which only allows the crude ON/OFF (bang-bang) control. Rather, a low-side switch made of an IRL540 N-channel MOSFET was used as driven by PWM on digital pin 26. This allows real proportionate control of the heater power, which is critical to the stability, and accuracy of the PID algorithm. The logic-level gate driving capability of the MOSFET is compatible with the Arduino 5 V output, and a 220 Ω gate resistor helps to restrict inrush current and safeguard the microcontroller pin.

Lastly, the inductive characteristic of relay coils posed the risk of spikes of voltages during deactivation, which would be detrimental to the driving transistors or microcontrollers. This was reduced by a 1N4148 fly back diode across the coils of a relay operated in reverse parallel which allowed the back-EMF current to conduct a safe path. Additionally, a 1 kΩ base resistor was included in each BC547 driver stage to limit base current and ensure the transistor operates safely in saturation. Combined with other engineering solutions, there has been a holistic design strategy in which accuracy, adaptability, and robustness are key elements. The system perceives every challenge with a designed, physics-conscious answer, which guarantees the reliable multi-sensor activities, the accuracy of thermal management, and complete confirmation in a simulated environment, which is a strong basis of possible physical implementation.

6. Conclusion

This research presented the successful design and implementation of an integrated intelligent system for conditioning and controlling temperature sensor signals, based on a microcontroller. The system demonstrates the ability to automatically recognize different types of sensors (NTC, PTC, RTD, and thermocouple), perform self-calibration on site using a reference sensor, and maintain precise temperature control using a digital PID algorithm. Comprehensive verification through simulation has proven the feasibility and reliability of the proposed architecture, achieving measurement accuracy better than ±0.3 °C and stable control. The solution combines the flexibility of multi-sensor support with the efficiency of a simulation-first design methodology, making it a practical solution for cost-limited measurement and control applications in educational, research, and industrial fields.

Recommendations for Future Research

Physical experimental verification: Build a physical prototype and test performance under real operating conditions, including the effects of noise and electromagnetic interference. Improve sensor recognition: Explore more powerful algorithms (machine learning) to improve the reliability of distinguishing between sensors with similar characteristics. Integration with the Internet of Things: Add a wireless communication module (such as Wi-Fi or LoRa) to enable remote monitoring and control, transforming the system into a smart node within a sensor network. Development of a graphical user interface: Design a computer or mobile application to facilitate system configuration and data display and analysis. Expand the range of supported sensors: Integrate additional sensor types (such as DS18B20 digital sensors or humidity and pressure sensors) to create a complete environmental monitoring system.

References

[1]. E. Burian, Micropower active optical position sensor for decimeter-range sensing gaps, in *Proceedings of the IEEE Sensors Conference*, 2023, pp. 1-3.

[2]. M. A. P. Pertijs, K. A. A. Makinwa, J. H. Huijsing, A CMOS smart temperature sensor with a 3σ inaccuracy of ±0.1 °C from -55 °C to 125 °C, *IEEE Journal of Solid-State Circuits*, Vol. 40, Issue 12, 2005, pp. 2805-2815.

[3]. M. A. K. Alia, T. Al Mograb, Investigation of an acoustic temperature transducer and its application for heater temperature measurement, *American Journal of Applied Sciences*, Vol. 4, Issue 5, 2007, pp. 294-299.

[4]. F. Sebastiano, et al., A low-voltage mobility-based frequency reference for crystal-less ULP radios, *IEEE Journal of Solid-State Circuits*, Vol. 44, Issue 7, 2009, pp. 2002-2009.

[5]. Y. Wang, V. Chodavarapu, Differential wide temperature range CMOS interface circuit for capacitive MEMS pressure sensors, *Sensors*, Vol. 15, Issue 2, 2015, pp. 4253-4263.

[6]. J. Li, Y. Lin, N. Ning, Q. Yu, A +0.44 °C/−0.4 °C inaccuracy temperature sensor with multi-threshold MOSFET-based sensing element and CMOS thyristor-based VCO, *IEEE Transactions on Circuits and Systems I: Regular Papers*, Vol. 68, Issue 3, 2021, pp. 1102-1113.

[7]. K.-C. Lin, M. Dandin, Capacitance sensor array for Lab-on-CMOS applications using a passive RFID interface, *Preprints.org*, 2026, 10.64898/ 2026.02.05.704137.

[8]. A. Mahar, et al., iThermoGraph: IoT-integrated graphene-based thermocouple for real-time temperature monitoring, in *Proceedings of the IEEE International Conference on Flexible and Printable Sensors and Systems (FLEPS)*, 2025, pp. 1-4.

[9]. H. Kappert, et al., A high temperature SOI-CMOS chipset focusing sensor electronics for operating temperatures up to 300 °C, *Journal of Microelectronics and Electronic Packaging*, Vol. 19, Issue 1, 2022, pp. 1-7.

[10]. C.-C. Chen, C.-L. Chen, Y. Lin, All-digital time-domain CMOS smart temperature sensor with on-chip linearity enhancement, *Sensors*, Vol. 16, Issue 2, 2016, 176.

[11]. C. Eder, V. Valente, N. Donaldson, A. Demosthenous, A CMOS smart temperature and humidity sensor with combined readout, *Sensors*, Vol. 14, Issue 9, 2014, pp. 17192-17211.

[12]. Z. Feng, H. Ye, Y. Lu, H. Zhang, et al., Flexible intelligent thermal management systems: Sensing devices, signals, and applications, *Nano Energy*, Vol. 138, 2025, 110842.

[13]. J. Yang, et al., A low-power differential temperature sensor with chopped cascode transistors and switched-capacitor integration, *Electronics*, Vol. 14, Issue 12, 2025, 2381.

[14]. W. Liu, J. Dai, Design of attitude sensor acquisition system based on STM32, in *Proceedings of the 5th International Conference on Instrumentation and Measurement, Computer, Communication and Control (IMCCC)*, 2015.

[15]. F. Nan, C. Zeng, H. Shen, L. Lin, Calibration of integrated low-cost environmental sensors for urban air temperature based on machine learning, *Sensors*, Vol. 25, Issue 11, 2025, 3398.

[16]. M. A. M. Alkhedher, T. M. Y. Younes, H. A. M. Hajeir, Programmable wiring system for reconfigurable devices, Patent US12244310B2, *United States*, 2025.

[17]. Y. Tao, T. Yu, Z. Hu, J. Yang, Highly integrated soft stress-temperature dual-mode sensor array based on impedance-modulated signal, *Measurement*, Vol. 259, 2026, 119759.

[18]. C. Xu, X. Hao, P. Pei, T. Wei, et al., Research on time constant test of thermocouples based on QNN-PID controller, *Sensors*, Vol. 25, Issue 12, 2025, 3819.

[19]. R. Qi, et al., Design of the PID temperature controller for an alkaline electrolysis system with time delays, *arXiv*, 2022, arXiv:2210.00801.

[20]. B. Neji, N. Ferko, R. Ghandour, A. S. Karar, et al., Micro-fabricated RTD based sensor for breathing analysis and monitoring, *Sensors*, Vol. 21, Issue 1, 2021, 318.

[21]. T. Sun, W. M. Tsang, Micro-fabricated skin-like ALN/Polyimide/PDMS sensor for obstructive sleep apnea monitoring, in *Proceedings of the 33rd IEEE International Conference on Micro Electro Mechanical Systems (MEMS)*, 2020, pp. 477-480.

[22]. M. Cai, Z. Zeng, Q. Xiang, S. Wu, et al., Design of multi-channel high-speed and high-precision digital receiver based on multi-FPGA, in *Proceedings of the 4th China International SAR Symposium (CISS)*, 2023, pp. 1-5.

[23]. J. Amorebieta, et al., Sensitivity-optimized strongly coupled multicore fiber-based thermometer, *Optics & Laser Technology*, Vol. 145, 2022, 107532.

Published by International Frequency Sensor Association (IFSA) Publishing, S. L., 2026 (http://www.sensorsportal.com).

Handbook
of Thermometry and Nanothermometry

S. Yatsyshyn, B. Stadnyk, Ya. Lutsyk, L. Buniak

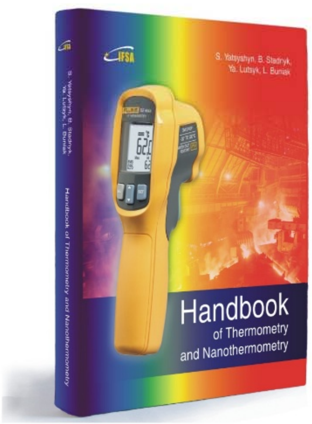

The Handbook of Thermometry and Nanothermometry presents and explains of main catchwords in the field of temperature measurements and nanomeasurements. This the first, well illustrated in full color, encyclopedia contains more than 800 articles (vocabulary entries) in thermometry and nanotermometry, and covers nearly every type of temperature measurement device and principles. At the end of book the authors provide a useful list of references for further information.

Written by experts, the book at the first place is destined for all who are not acquainted enough with specificity of temperature measurement but are interested in it and study literary sources in this realm. The authors tried to enter maximally on catchwords list the issues, which refer directly or indirectly to thermometry as well as to nanothermometry. The last one is the most modern chapter of thermometry and simultaneously of nanometrology. *The Handbook of Thermometry and Nanothermometry* is a 'must have' guide for both beginners and experienced practitioners who want to learn more about temperature measurements in various applications: engineers, students, researchers, physicists and chemists of all disciplines. In addition, this book will influence the next decade or more of road design in the nanothermometry.

Hardcover: ISBN 978-84-606-7518-1
e-Book: ISBN 978-84-606-7852-6

Order: http://www.sensorsportal.com/HTML/BOOKSTORE/Thermometry.htm

Sensors & Transducers, Vol. 273, Issue 2, June 2026, pp. 21-29

Sensors & Transducers

Published by IFSA Publishing, S. L., 2026

http://www.sensorsportal.com

A Study on SiC-MEMS Based Peripheral MOSFET Embedded and Current Mirror Integrated Pressure Sensor for High-Temperature Applications

[1, *] Gaurav KUMAR, [1] Menuvolu TETSEO, [1] Kalpana GOGOI, [2] Shashi KUMAR, [1] Pradeep Kumar RATHORE, [3] Kulwant SINGH, [4] Shankar DUTTA and [5] Lolit Kumar SINGH

[1] Department of Electronics and Communication Engineering, National Institute of Technology Meghalaya, Sohra, 793108, Meghalaya, India

[2] Micron Technology Operation India LLP, Hyderabad, India

[3] Department of Industry 4.0, Skill Faculty Engineering & Technology, Shri Vishwakarma Skill University, Palwal, Haryana, India

[4] Micro-Electro-Mechanical System Division, Solid State Physics Laboratory, Defence Research & Development Organisation (DRDO), Delhi, India

[5] Department of Electronics and Communication Engineering, National Institute of Technology Manipur, Imphal, India

Tel.: +91 9418580400

[*] Gaurav.kumar@nitm.ac.in

Received: 17 Feb. 2026 /Revised: 23 March 2026 /Accepted: 15 May 2026 /Published: 29 June 2026

Abstract: This paper presents a design and simulation study of SiC-MEMS pressure sensors featuring an embedded peripheral MOSFET and an integrated current-mirror for high temperature applications. The proposed pressure sensor structures employ square and circular shaped strain sensing MOSFETs embedded on the periphery of square and circular SiC diaphragms, respectively. The MOSFETs are configured as a resistively loaded current mirror configuration. Pressure-induced strain is detected through the piezoresistive behaviour of 4H-SiC n-channel MOSFET devices. The mechanical and electrical behaviour of the proposed sensors was simulated using COMSOL Multiphysics and TSPICE software over pressure and temperature ranges of 0 – 10 MPa and 25 – 400 °C, respectively. The simulated pressure sensitivities for square and circular sensors were found to be 0.2 mV/MPa and 0.4 mV/MPa, respectively, at 25 °C which increased to 27.86 mV/MPa and 62.66 mV/MPa at 400 °C. The temperature sensitivities of proposed square and circular shaped pressure sensors were found to be 0.65 mV/ °C and 1.49 mV/ °C, respectively, at an applied pressure of 10 MPa. The simulation results underscore the critical role of channel geometry in improving sensor sensitivity, paving the way for robust 4H-SiC MOS-based pressure sensors for harsh environments.

Keywords: Silicon carbide, MOSFET, MEMS, Pressure sensor, Piezoresistivity, Current mirror, Diaphragms.

1. Introduction

Pressure is a critical physical parameter widely utilized in consumer electronics, medical, aerospace, automotive, industrial and defence applications [1]. Advancements in semiconductor and Micro-Electro-Mechanical Systems (MEMS) technologies have enabled the integration of complex mechanical components such as beams, flexures, linkages, sensing units, and actuators onto a single microchip [2-7].

Among MEMS structures, the diaphragm is the most fundamental micromechanical element and is widely used in pressure sensors. When subjected to pressure, a diaphragm deflects and this deflection can be measured by piezoresistive [8], piezoelectric [9], capacitive [10], or optical methods [11]. However, each technique has its limitations, especially under harsh environmental conditions [12]. The MOSFET embedded sensing technique enables the development of CMOS-MEMS integrated sensors by offering a novel transduction mechanism based on the piezoresistive characteristics of MOSFETs [13].

Researchers from all across the world are attempting to optimise silicon transistors for pressure measurement in order to boost sensitivity and reduce device size and minimize the mechanical and electrical faults [14-16]. However, high temperatures have an impact on silicon device performance, limiting their use in extremely harsh environments [17]. MEMS pressure sensors based on silicon carbide (SiC) have become a possible substitute for silicon because of their low intrinsic carrier concentration, strong breakdown field strength, and broad bandgap (3 eV), which make them appropriate for high temperature applications [18]. The piezoresistive properties of SiC have been widely explored by researchers for pressure sensing applications in harsh environments [19-21].

In our earlier work [22], a conceptual and simulation study was conducted on a SiC-MEMS pressure sensor integrating a conventional rectangular MOSFET-based strain sensing element, a current mirror readout circuit and a SiC diaphragm, representing one of the earliest reports on SiC-based MOSFET embedded pressure sensors with current mirror readout. The sensor employed two smaller strain sensing MOSFETs at the diaphragm's edge and centre to sense tensile and compressive stresses under applied pressure. This work extends our previous study by proposing pressure sensors with a single square or circular MOSFET at the periphery of square or circular SiC diaphragms to exploit maximum edge stresses. This paper presents background and related work in Section 1, sensor structure and operation in Section 2, followed by simulation results in Section 3, design of mask layout and fabrication steps in Section 4, and finally concludes in Section 5.

2. Sensor Structure and Working Principle

This study investigates two pressure sensor structures that employ square and circular shaped strain sensing MOSFETs embedded on the periphery of square and circular SiC diaphragms, respectively. The MOSFETs are arranged in a current mirror configuration with resistive loads, as shown in Fig. 1(a) and 1(b). Fig. 1(c) and 1(d) present the cross-sectional views of square and circular strain-sensitive MOSFETs integrated along the edges of the SiC diaphragms. Identical current-mirror pairs (M1–M2) are used in each design, with M1 as the reference and sensing transistor, M2, is integrated on a flexible SiC diaphragm that bends when external pressure is applied, modulating carrier mobility in the channel and consequently altering the drain current. This variation produces a pressure-dependent output voltage across the drains of the current-mirror circuit. Table 1 presents the fundamental governing equations of the proposed SiC-MEMS based peripheral MOSFET embedded and current mirror integrated pressure sensors.

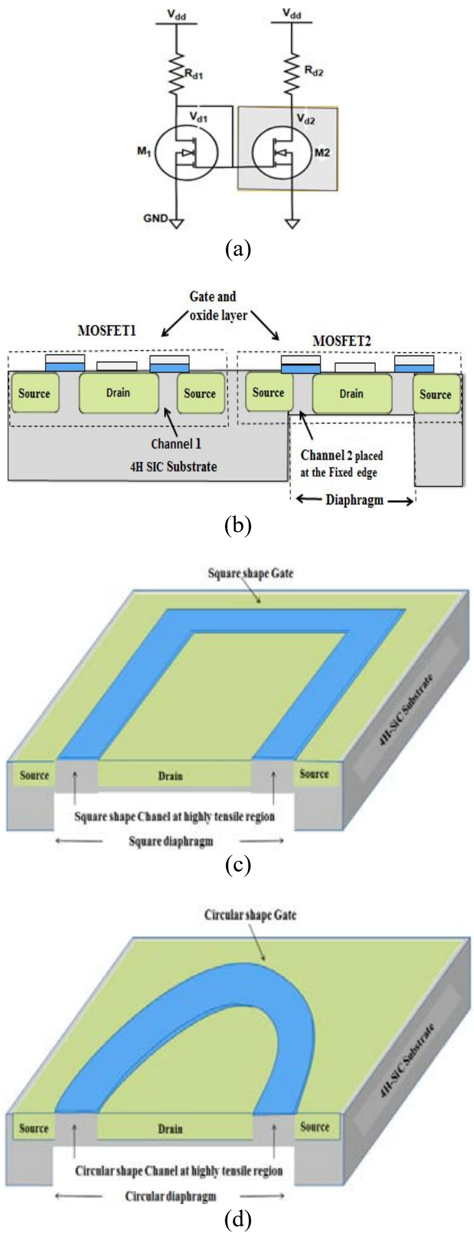

Fig. 1. (a) Schematic of a resistively loaded n-channel MOSFET current mirror circuit with the reference transistor M1 and the pressure-sensitive transistor M2, (b) Cross-sectional view of the SiC-based MOSFET integrated pressure sensor structure, (c) Cross-sectional view of the square shaped MOSFET-based sensor, (d) Cross-sectional view of the circular shaped MOSFET-based sensor.

Table 1. Fundamental governing equations of the proposed SiC-MEMS based peripheral MOSFET embedded and current mirror integrated pressure sensors.

A. Mechanical pressure sensing elements: Square and circular diaphragms [23]		
Diaphragm shape	**Maximum displacement**	**Maximum stress**
Square	$0.26pa^4\frac{(1-\nu^2)}{Eh^3}$	$1.23p\frac{a^2}{h^2}$
Circular	$0.19pa^4\frac{(1-\nu^2)}{Eh^3}$	$0.75p\frac{a^2}{h^2}$
B. Transduction mechanism: Piezoresistive effect in MOSFET [24]		
$\frac{\Delta\mu}{\mu} = -\frac{\Delta R}{R} = -(\pi_l\sigma_l + \pi_t\sigma_t)$		
C. Current mirror readout circuit		
$V_{OUT} = V_{D1} - V_{D2} = (I_{D2} - I_{D1})R_D$, $I_{D1} = \mu C_{ox}\frac{W}{L}\frac{(V_{gs} - V_t)^2}{2}$, $I_{D2} = (\mu + \Delta\mu)C_{ox}\frac{W}{L}\frac{(V_{gs} - V_t)^2}{2}$, where p is the applied pressure, a is the side length or radius and h indicates the thickness of square and circular diaphragm, E and ν denotes the Young's modulus and Poisson's ratio of the diaphragm material, μ and R are the initial electron mobility and channel resistance, Δμ and ΔR are the changes in electron mobility and channel resistance under applied pressure, π_l, π_t, σ_l and σ_t denotes the longitudinal and transverse piezoresistive and stress components, RD is the drain resistance, ID1, ID2, VD1 and VD2 are the drain current and voltages of reference and pressure sensing MOSFETs.		

The design and simulation parameters used for the proposed SiC-MEMS pressure sensor embedded peripheral MOSFET and integrated current mirror are given in Table 2. In the first pressure sensing structure, a square shaped SiC strain sensing MOSFET with its channel integrated along the periphery of a square SiC diaphragm. Similarly, for the second sensor structure, a circular shaped SiC strain sensing MOSFET with its channel integrated along the periphery of circular SiC diaphragm. The simulations of mechanical and electrical performance were carried out using COMSOL Multiphysics and TSPICE.

3. Results and Discussion

To investigate the piezoresistive behaviour of square and circular shaped n-channel SiC MOSFET pressure sensing structures, a three-dimensional finite element model consisting of an n-channel MOSFET equivalent piezoresistive embedded in SiC diaphragm was developed using COMSOL Multiphysics. The temperature-dependent electrical behavior of the n-channel 4H-SiC MOSFET, as reported in [26], was assumed to align with standard current-mirror-based pressure sensing designs. At room temperature, a voltage equivalent to the MOSFET Early voltage was applied across the corresponding piezoresistor, and this voltage was used exclusively to simulate the sensor's piezoresistive behaviour in COMSOL Multiphysics. To evaluate the device response under applied stress, pressure was applied on the diaphragm. Fig. 2(a) illustrates the three-dimensional square-shaped pressure sensing structure modelled in COMSOL Multiphysics, while Fig. 2(b) depicts the corresponding stress distribution in the square diaphragm under externally applied pressure of 10 MPa. The stress profile is visualized using a color gradient, where purple represents regions of minimum stress and red indicates areas of maximum stress. Similarly, Fig. 3 shows the three-dimensional circular-shaped pressure-sensing structure and stress distribution in the circular diaphragm subjected to 10 MPa of applied pressure.

Table 2. Parameters used for design and simulation of the proposed SiC-MEMS based pressure sensor featuring a peripheral embedded MOSFET and a current-mirror readout circuit.

Parameter	**Unit**	**Square Shape**	**Circular Shape**
A. Parameters for analyzing Piezoresistive Effects in N-Channel 4H-SiC MOSFETs using COMSOL Multiphysics.			
Diaphragm dimensions (side/diameter, thickness)	μm	100, 2.5	110, 2.5
MOSFET equivalent piezoresistor value	kΩ	13852	13852
Piezoresistive coefficients [25] ($\times 10^{-11}$)	Pa^{-1}	$\pi_{11} = -3.4$, $\pi_{12} = 6.15$	$\pi_{11} = -3.4$, $\pi_{12} = 6.15$
B. Parameters for analyzing electrical behavior of Current Mirror Design using TSpice software.			
MOSFET dimensions (L, W)	μm	10, 300	10, 300
Early voltage	(V/μm)	33	33
Oxide capacitance (Cox)	fF/μm^2	4.425	4.425
Gate Oxide thickness (tox)	nm	20	20
Threshold Voltage(Vth)	V	2.69	2.69
Carrier mobility (μ)	cm^2/Vs	0.0248	0.0248
Gate-to-source voltage, VGS	V	20	20
Drain resistor, RD	kΩ	10	10
Reference current, I_{ref}	μA	23.8255	23.8255

The simulation results reveal that the maximum stress is concentrated around the clamped edges of the diaphragm, reaching 5661 MPa for the square diaphragm and 5371 MPa for the circular diaphragm. This confirms that the square diaphragm experiences greater stress concentration at its fixed boundaries under the applied pressure. To assess the accuracy and reliability of the simulation results for the 4H-SiC MOSFET-based piezoresistive sensor, a mesh convergence analysis was performed in COMSOL Multiphysics for both circular and square piezoresistor configurations under a uniform applied pressure of 10 MPa.

Nine different mesh sizes were employed to assess model sensitivity and convergence. The simulation results for the square and circular geometries are summarized in Table 3. Fig. 4 shows the variation in resistance of square and circular MOSFET-equivalent piezoresistors with different default mesh settings in COMSOL Multiphysics. In both cases, the resistance values are nearly saturated as the mesh is refined from finer to extremely fine. Based on this convergence, the finer mesh setting was chosen for simulations to balance accuracy and computational efficiency.

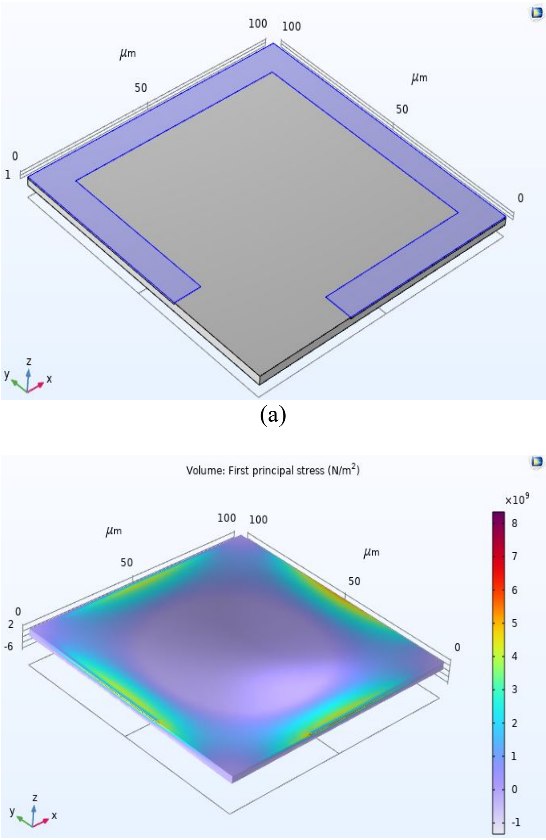

(a)

(b)

Fig. 2. (a) Three-dimensional square shaped pressure sensing structure integrated with a square shaped MOSFET equivalent piezoresistor, and (b) Stress distribution at an applied pressure of 10 MPa.

Fig. 5(a) depicts channel resistance versus applied pressure (0–10 MPa) for square and circular 4H-SiC MOSFETs. MOSFET M1, located at the fixed edge, exhibits a constant channel resistance of 13.85 MΩ, indicating no pressure sensitivity. In contrast, MOSFET M2 devices with square and circular channels, embedded near the fixed edge, experience longitudinal channel stress under applied pressure, resulting in pressure-dependent resistance reduction. At 10 MPa, the channel resistance decreases to 13.70 MΩ for the square channel and 13.56 MΩ for the circular channel. Fig. 5(b) depicts the effect of externally applied pressure on the channel mobility of the current mirror transistor (M2), whereas the reference transistor (M1) retains a constant mobility of 0.0248 cm²/V·s, indicating no pressure dependence. In contrast, the pressure-sensitive MOSFETs M2 with square and circular channels exhibit a noticeable increase in channel mobility with rising pressure, reaching 0.0251 cm²/V·s and 0.0253 cm²/V·s, respectively. The simulated drain current and channel resistance under zero pressure show good agreement with COMSOL results. The pressure response of M2 was further analysed using FEM modelling. For input pressure of 10 MPa, an increase of nearly 0.2 µA is observed in the drain current for the square shaped channel and 0.41 µA for the circular channel configuration, which are then converted to voltage signals using the drain resistance R_D, as shown in Fig. 1(a).

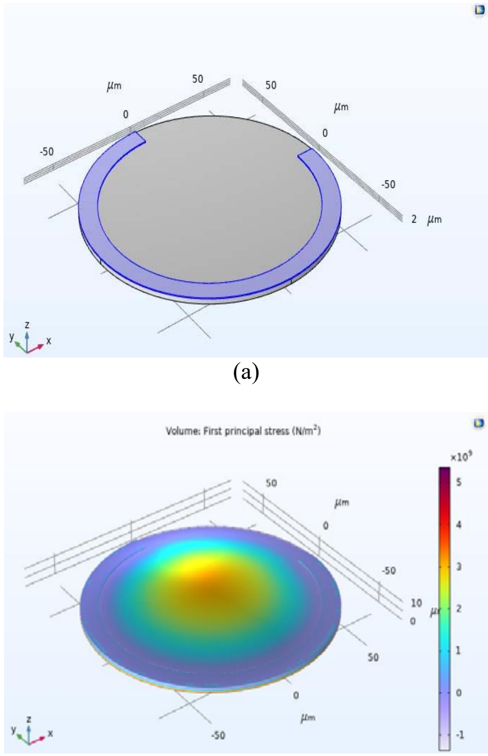

(a)

(b)

Fig. 3. (a) Three-dimensional circular shaped pressure sensing structure integrated with a circular shaped MOSFET equivalent piezoresistor, and (b) Mechanical stress distribution under an applied pressure of 10 MPa.

Table 3. Results of mesh analysis for circular and square-shaped MOSFET equivalent piezoresistor.

Default mesh size in COMSOL Multiphysics	MOSFET equivalent piezoresistance (MΩ)	
	Circular shaped	Square shaped
Extremely coarse	13.347	13.70
Extra coarse	13.362	13.741
Coarser	13.415	13.768
Coarse	13.510	13.809
Normal	13.560	13.839
Fine	13.670	13.855
Finer	13.728	13.8601
Extra fine	13.745	13.86302
Extremely fine	13.758	13.86417

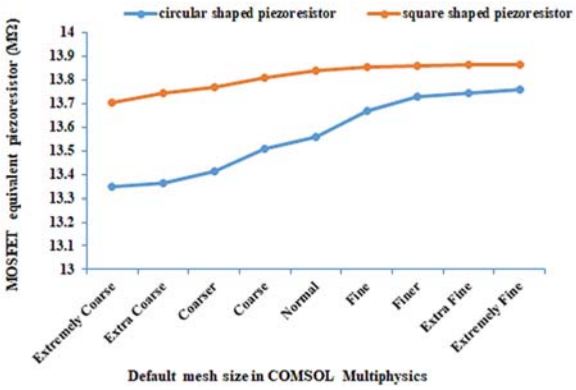

Fig. 4. Variation in MOSFET equivalent piezoresistance as a function of mesh size for square and circular shaped piezoresistors.

As illustrated in Fig. 6, the drain output voltages of both the reference and pressure-sensitive MOSFETs change in response to the applied pressure for square and circular channel geometries placed near the diaphragm's edge, The drain voltage exhibits a continuous decline as the applied pressure rises to 10 MPa. Under ambient conditions (25 °C and 10 MPa), the differential output voltages $V_{D1} - V_{D2}$ for the square and circular peripheral MOS devices are approximately 2 mV and 4.17 mV, respectively. Fig. 7 presents the output response of the proposed peripheral MOS-embedded SiC-MEMS pressure sensors at a raised temperature of 400 °C. Due to the excellent temperature endurance and robustness of 4H-SiC in extreme environments, the proposed sensor has an almost linear voltage response with increasing temperature under constant pressure conditions.

The output voltages of the square and circular shaped peripheral MOSFET embedded pressure sensors reach approximately 278.5 mV and 626.6 mV, respectively. This consistent increase in output voltage with temperature indicates reliable device operation and confirms its ability to maintain stable performance at elevated temperatures, thereby validating the suitability of the proposed design for harsh-environment sensing applications. Figs. 8 and 9 illustrate the output voltage response of the square and circular shaped SiC MOSFET-based pressure sensors as a function of input pressure applied in the range of 0 to 10 MPa over a temperature span of 25 °C to 400 °C. The results show that the sensor's output voltage exhibits a linear dependence on input applied pressure across the full range of temperature from 25 °C to 400 °C.

4. Proposed Mask Layout and Fabrication Process Flow

This section proposes design of mask layout and step by step fabrication process flow for the development of proposed 4H-SiC MOSFET-based pressure sensors. As illustrated in Figs. 10, the fabrication of proposed SiC based pressure sensors employ six-mask-layer design, following a "CMOS-First" and "MEMS-Last" integration strategy. The proposed pressure sensor chip, with dimensions of 620 × 620 µm, was designed using K-Layout software. The fabrication process flow for the proposed pressure sensors was designed based on established literature on fabrication of SiC based MOSFET and bulk micromachining techniques of SiC substrate [26–28]. Fig. 11. illustrates the sequential fabrication process of the proposed 4H-SiC n-channel MOSFET device.

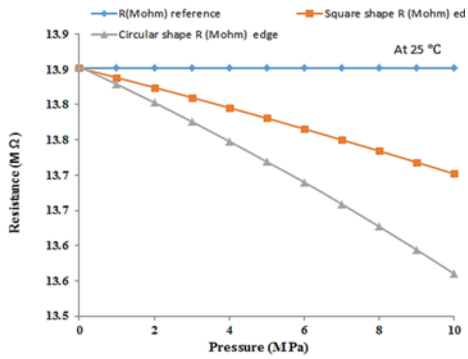

(a)

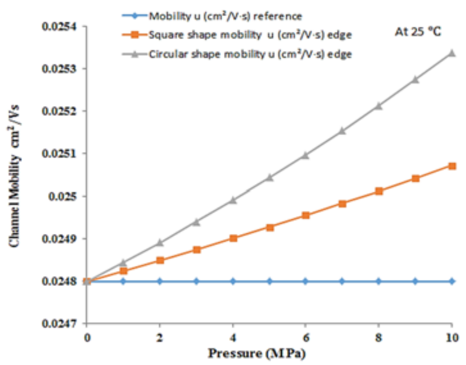

(b)

Fig. 5. Pressure-dependent characteristics showing (a) channel resistance and (b) carrier mobility for square- and circular shaped sensing MOSFETs as a function of pressure.

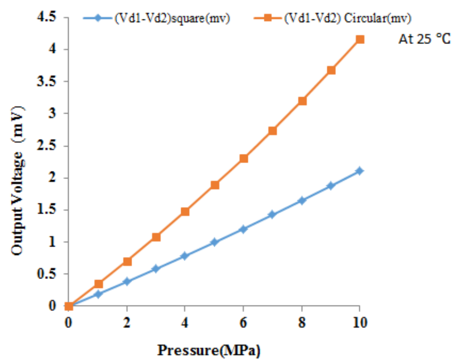

Fig. 6. Pressure-dependent output voltage characteristics at 25 °C, exhibiting pressure sensitivities of approximately 0.21 and 0.41 mV/MPa, respectively, for the square and circular shaped SiC MOS based pressure sensors as a function of pressure.

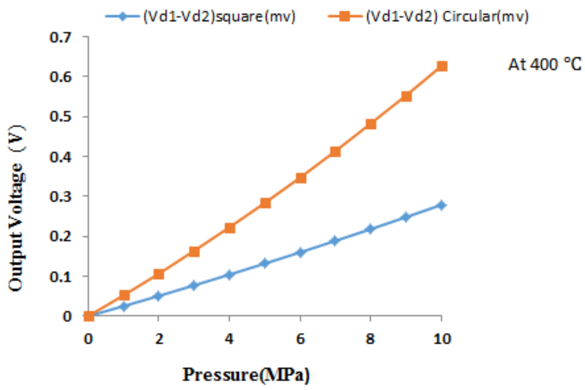

Fig. 7. Output voltage characteristics of square and circular SiC MOSFET-based pressure sensors at 400 °C, showing pressure sensitivities of approximately 27.86 and 62.62 mV/MPa, respectively.

The details of the proposed fabrication process flow are outlined below:

a) The fabrication of the sensor begins with a properly cleaned p-type 4H-SiC substrate;
b) A thick SiO_2 field oxide layer is deposited to provide surface isolation;
c) The first photolithography step defines the source and drain regions;
d) Arsenic ion implantation is performed to achieve n-type doping in these regions;
e) Dopant activation is carried out through post-implantation annealing, during which a carbon cap is employed to prevent surface degradation;
f) The carbon cap is subsequently removed;
g) A thin gate oxide is grown by thermal oxidation'
h) The second photolithography step patterns the contact vias for the source and drain, followed by Nb/Ni deposition to form low-resistance ohmic contacts;
i) Source and drain contacts are formed using a lift-off process;
j) Metal silicidation is performed to further reduce contact resistance;
k) An aluminum layer is deposited over the structure;
l) The third photolithography step patterns the aluminum layer to form the gate electrode and contact pads for the source, drain and gate;
m) An interlayer SiO_2 dielectric is deposited to electrically isolate the metal layers;
n) The fourth photolithography step, followed by dielectric etching, opens the contact windows;
o) A second aluminum layer is deposited for final metallization;
p) Photoresist is applied to both sides of the wafer;
q) The fifth photolithography step defines the backside oxide window to enable diaphragm formation;
r) The diaphragm is realized through backside bulk micromachining of the 4H-SiC substrate;
s) Photoresist is removed from both sides of the wafer;
t) The sixth photolithography step patterns the top metal interconnects and contact pads.

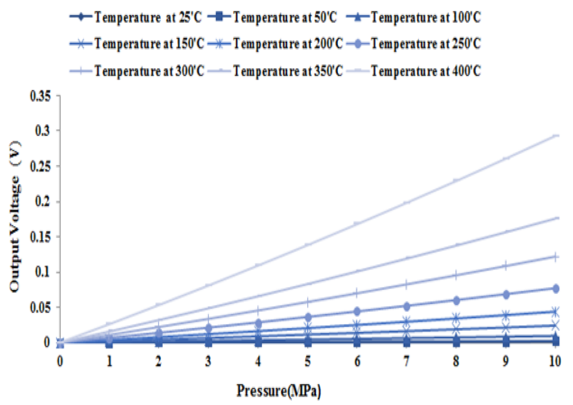

Fig. 8. Variation in the output voltage of square shaped pressure sensor as a function of applied pressure at various temperatures ranging from 25 **°C** to 400 **°C**.

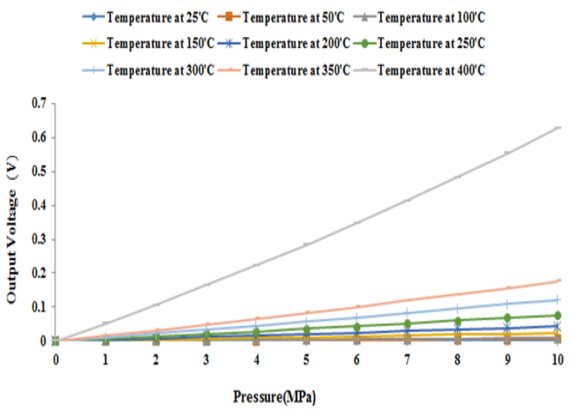

Fig. 9. Variation in the output voltage of circular shaped pressure sensor as a function of applied pressure at various temperatures ranging from 25 °C to 400 °C.

The proposed sensors exhibit competitive sensitivity, demonstrating their suitability for high-temperature pressure sensing. Table 4 compares their sensitivity with previously reported works, highlighting improved performance. Table 5 summarizes important parameters such as chip size, operating pressure range, full-scale output, linearity deviation, and sensitivity at both room temperature and 400 °C.

The observed improvement in sensitivity at elevated temperatures can be attributed to temperature-dependent device characteristics. At higher temperatures, reduced interface trap occupancy and diminished Coulomb scattering enhance the effective channel mobility, as reported in [29–33]. Furthermore, the decrease in threshold voltage with increasing temperature leads to a higher drain current, which collectively contributes to the enhanced sensitivity.

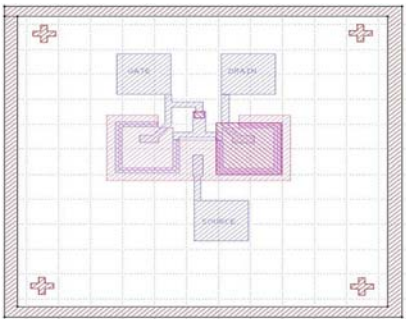

(a)

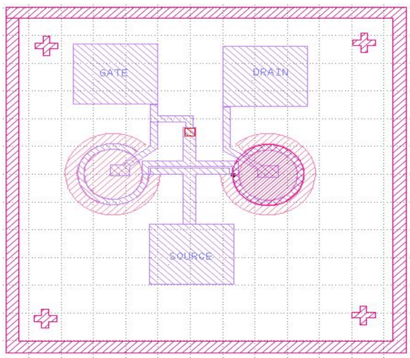

(b)

Fig. 10. Mask layout design of the proposed square and circular shaped SiC MOSFET embedded pressure sensor featuring an integrated current mirror configuration.

Table 4. Comparison of present work with SiC based pressure sensors reported in literature.

Ref.	Sensitivity (mV/MPa)	Readout circuit	Temperatur e
[34]	15.6	Wheatstone Bridge	30 °C
[35]	3.4	Wheatstone Bridge	500 °C
[36]	13.4	Wheatstone Bridge	600 °C
[37]	2	Wheatstone Bridge	400 °C
This work	27.86 and 62.62	Current mirror	400 °C

5. Conclusions

This article describes the design and simulation based study of a 4H-SiC MEMS pressure sensor integrated with n-channel MOSFETs using square and circular shaped channel geometries connected in a current mirror configuration. The proposed pressure sensor structures employ square and circular shaped strain sensing MOSFETs embedded on the periphery of square and circular SiC diaphragms, respectively. The sensor converts strain-induced variations into electrical signals by exploiting the piezoresistive properties of 4H-SiC, achieving linear response over a pressure range of 0 – 10 MPa and temperatures up to 400 °C. Simulation results show enhanced pressure sensitivity for the circular-channel design and reduced temperature sensitivity for the square-channel configuration. The CMOS compatible design ensures robust performance in harsh environments, which clearly indicates its potential use in high-temperature applications for the aerospace, automotive, petrochemical, nuclear, and oil & gas sectors.

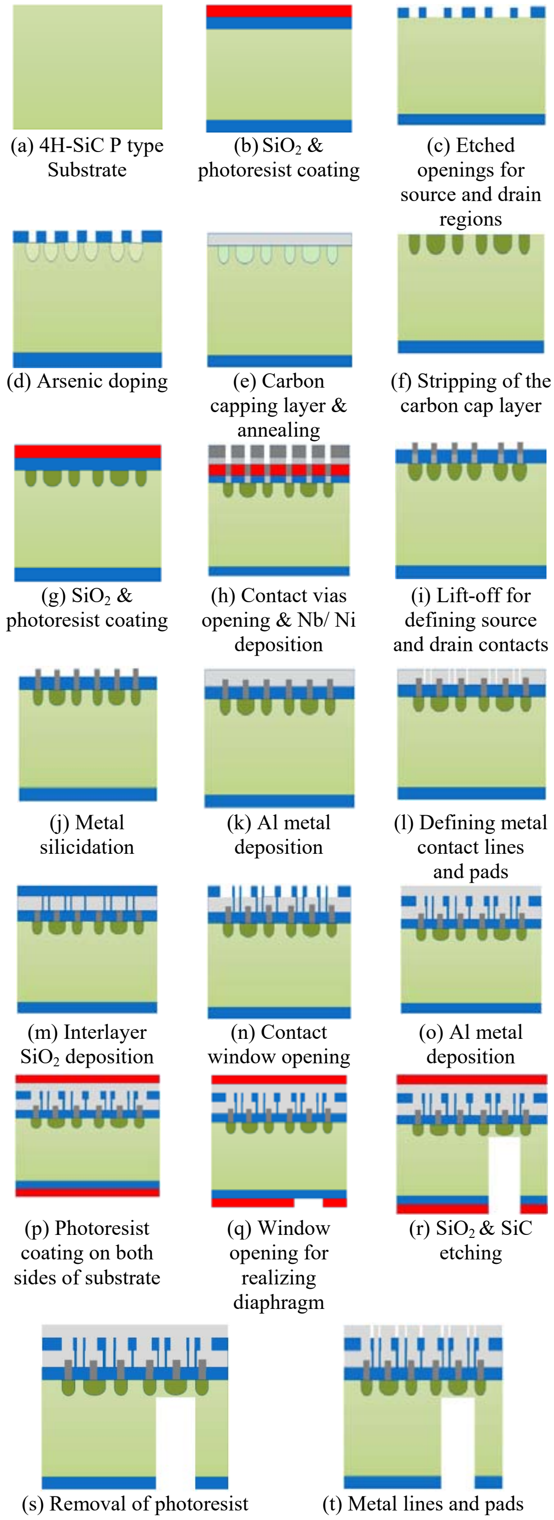

Fig. 11. Design of proposed fabrication process flow of the proposed n-channel 4H-SiC MOSFET based pressure sensor incorporating square and circular channel structures in a current mirror configuration.

Table 5. Key parameters of square and circular shaped SiC-MEMS based Peripheral MOSFET Embedded and Current Mirror Integrated Pressure Sensors.

Parameter	Unit	Square Shape	Circular Shape
A. General Sensor Parameters			
Chip area	μm^2	620 × 620	620 × 620
Pressure range	MPa	0-10	0-10
B. Output Characteristics at Different Temperatures			
FSO value measured at 25 °C	mV	2	4.17
FSO value measured at 400 °C	mV	278.5	626.6
Linearity error in FSO at 25 °C	%	2.29	4.14
Linearity error in FSO at 400 °C	%	2.36	4.07
Pressure sensitivity at 25 °C	mV/MPa	0.20	0.416
Pressure sensitivity at 400 °C	mV/MPa	27.86	62.66
C. Thermal Sensitivity and Errors			
Temperature sensitivity at 10 MPa	mV/ °C	0.65	1.49
Error in temperature sensitivity at 1 MPa	μV/ °C	8.27	25.1
Error in temperature sensitivity at 10 MPa	μV/ °C	17.1	64

Acknowledgements

The authors gratefully acknowledge support provided through Project Grant (DFTM/07/3603/ DIA-CoE, MZU/MEMS/P-03). The authors also acknowledge the National Institute of Technology Meghalaya for providing institute overhead funds from the DRDO-sponsored project for the payment of publication fees.

References

[1]. X. Han, M. Huang, Z. Wu, Y. Gao, et al., Advances in high performance MEMS pressure sensors: Design, fabrication and packaging, *Microsystems & Nanoengineering*, Vol. 9, Issue 1, 2023, 156.

[2]. E. B. Mansouri, L. M. Middelburg, R. H. Poelma, G. Q. Zhang, et al., High-resolution MEMS inertial sensor combining large proof-mass and integrated capacitive transduction, *Microsystems & Nanoengineering*, Vol. 5, Issue 1, 2019, 60.

[3]. X. He, D. Li, H. Zhou, X. Hui, et al., Theoretical and experimental studies on MEMS variable cross-section cantilever beams for vibration energy harvesting, *Micromachines*, Vol. 12, Issue 7, 2021, 772.

[4]. S. Liao, H. Wang, Z. Li, Design, assembly and simulation of flexure-based modular mechanisms, *Machines*, Vol. 10, Issue 6, 2022, 421.

[5]. X. P. S. Su, H. S. Yang, Design of compliant microleverage mechanisms, *Sensors and Actuators A: Physical*, Vol. 87, Issue 3, 2001, pp. 146-156.

[6]. A. S. Algamili, M. H. Khir, J. O. Dennis, A. Y. Ahmed, et al., A review of actuation and sensing mechanisms in MEMS-based sensor devices, *Nanoscale Research Letters*, Vol. 16, Issue 1, 2021, 16.

[7]. S. Jena, A. Gupta, Review on pressure sensors: A perspective from mechanical to micro-electro-mechanical systems, *Sensor Review*, Vol. 41, Issue 3, 2021, pp. 320-329.

[8]. R. Devi, S. S. Gill, B. Singh, Quantitative analysis of MEMS piezoresistive squared diaphragm pressure sensor for biomedical applications, *Measurement: Sensors*, Vol. 24, 2022, 100522.

[9]. A. Kumar, A. Varghese, A. Sharma, M. Prasad, et al., Recent development and futuristic applications of MEMS based piezoelectric microphones, *Sensors and Actuators A: Physical*, Vol. 347, 2022, 113877.

[10]. K. B. Balavalad, B. G. Sheeparamatti, A critical review of MEMS capacitive pressure sensors, *Sensors & Transducers*, Vol. 187, Issue 4, 2015, pp. 120-129.

[11]. Y. Ge, M. Wang, H. Yan, The principle and architectures of optical stress sensors and the progress on the development of microbend optical sensors, *Advanced Optical Materials*, Vol. 9, Issue 10, 2021, 2001693.

[12]. L. M. Middelburg, W. D. Driel, G. Q. Zhang, From Si towards SiC technology for harsh environment sensing, in Sensor Systems Simulations: From Concept to Solution (W. D. Driel, O. Pyper, C. Schumann, Eds.), *Springer*, Cham, 2020, pp. 1-15.

[13]. N. Wacker, H. Richter, CoMPact modeling of CMOS transistors under uniaxial stress, in *Proceedings of the SAFE Workshop*, 2019, pp. 179-181.

[14]. N. Hafez, S. Haas, K. U. Loebel, D. Reuter, Characterization of MOS transistors as an electromechanical transducer for stress, *Physica Status Solidi A*, Vol. 216, Issue 19, 2019, 1700680.

[15]. M. Basov, Pressure sensor with novel electrical circuit utilizing bipolar junction transistor, in *Proceedings of the IEEE Sensors Conference*, 2021, pp. 1-4.

[16]. L. Ramirez, F. Fruett, Multi-terminal piezo-MOSFET sensor for stress measurements in silicon, in *Proceedings of the 31st Symposium on Integrated Circuits and Systems Design (SBCCI)*, 2018, pp. 1-6.

[17]. W. D. Driel, O. Pyper, C. Schumann, Sensor Systems Simulations: From Concept to Solution, *Springer*, Cham, 2020.

[18]. Q. Zhang, Y. Liu, H. Li, J. Wang, et al., A review of SiC sensor applications in high-temperature and radiation extreme environments, *Sensors*, Vol. 24, Issue 23, 2024, 7731.

[19]. R. Wu, H. Chen, Y. Zhou, Y. Guo, et al., Advances in silicon carbides and their MEMS pressure sensors for high temperature and pressure applications, *ACS Applied Materials & Interfaces*, Vol. 17, Issue 18, 2025, pp. 26117-26155.

[20]. H. P. Phan, D. V. Dao, K. Nakamura, S. Dimitrijev, et al., The piezoresistive effect of SiC for MEMS sensors at high temperatures: A review, *Journal of Microelectromechanical Systems*, Vol. 24, Issue 6, 2015, pp. 1663-1677.

[21]. M. A. Fraga, H. Furlan, R. S. Pessoa, M. J. M. T. Massi, Wide bandgap semiconductor thin films for piezoelectric and piezoresistive MEMS sensors applied at high temperatures: An overview, *Microsystem Technologies*, Vol. 20, Issue 1, 2014, pp. 9-21.

[22]. G. Kumar, S. Kumar, M. Tetseo, K. Gogoi, et al., Analytical study on the SiC-MOSFET current mirror integrated MEMS pressure sensor for harsh environment applications, *Microsystem Technologies*, Vol. 31, Issue 9, 2025, pp. 2657-2667.

[23]. M. Bao, Analysis and Design Principles of MEMS Devices, *Elsevier*, Amsterdam, 2005.

[24]. T. Sugiura, N. Takahashi, N. Nakano, The piezoresistive mobility modeling for cubic and hexagonal silicon carbide crystals, *Journal of Applied Physics*, Vol. 127, Issue 24, 2020, 245105.

[25]. B. Tian, H. Shang, D. Wang, Y. Liu, et al., Investigation on piezoresistive effect of n-type 4H-SiC based on all-SiC pressure sensors, *IEEE Sensors Journal*, Vol. 22, Issue 7, 2022, pp. 6435-6441.

[26]. D. Kimoto, Characterization and modeling of SiC integrated circuits for harsh environment, PhD Thesis, *Kyoto University*, Kyoto, 2017.

[27]. S. Tanaka, K. Rajanna, T. Abe, M. Esashi, Deep reactive ion etching of silicon carbide, *Journal of Vacuum Science & Technology B*, Vol. 19, Issue 6, 2001, pp. 2173-2176.

[28]. Q. Wang, R. Zhang, Q. Chen, R. Duan, A review of femtosecond laser processing of silicon carbide, *Micromachines*, Vol. 15, Issue 5, 2024, 639.

[29]. S. Das, Y. Zheng, A. Ahyi, M. A. Kuroda, et al., Study of carrier mobilities in 4H-SiC MOSFETs using Hall analysis, *Materials*, Vol. 15, Issue 19, 2022, 6736.

[30]. R. R. Rao, S. Balaji, K. Matocha, V. Tilak, An approach to model temperature effects of interface traps in 4H-SiC, *Materials Science Forum*, Vol. 556, 2007, pp. 497-500.

[31]. S. Das, D. J. Lichtenwalner, S. R. Stein, S. H. Ryu, Characterization of interface trap and mobility degradation in SiC MOS devices using gated Hall measurements, *Solid State Phenomena*, Vol. 375, 2025, pp. 49-53.

[32]. S. Potbhare, Modeling and characterization of 4H-SiC MOSFETs: High field, high temperature, and transient effects, PhD Thesis, *University of Maryland*, College Park, 2008.

[33]. P. Fiorenza, F. Giannazzo, F. Roccaforte, Characterization of SiO2/4H-SiC interfaces in 4H-SiC MOSFETs: A review, *Energies*, Vol. 12, Issue 12, 2019, 2310.

[34]. H. Shang, B. Tian, D. Wang, Y. Liu, et al., Development of all-SiC absolute pressure sensor based on sealed cavity structure, *IEEE Sensors Journal*, Vol. 21, Issue 24, 2021, pp. 27308-27314.

[35]. X. Fang, W. Chen, G. Xin, Z. Libo, et al., Development of a 4H-SiC piezoresistive pressure sensor for high temperature applications, in *Proceedings of the 14th IEEE International Conference on Nano/Micro Engineered and Molecular Systems (NEMS)*, 2019, pp. 105-109.

[36]. T. Akiyama, T. Briand, N. F. Rooij, Piezoresistive n-type 4H-SiC pressure sensor with membrane formed by mechanical milling, in *Proceedings of the IEEE Sensors Conference*, 2011, pp. 222-225.

[37]. G. Wieczorek, B. Schellin, E. Obermeier, G. Fagnani, et al., SiC based pressure sensor for high-temperature environments, in *Proceedings of the IEEE Sensors Conference*, 2007, pp. 748-751.

Published by International Frequency Sensor Association (IFSA) Publishing, S. L., 2026 (http://www.sensorsportal.com).

Parvej Ahmad Alvi

IFSA

MEMS Pressure Sensors:

Fabrication and Technologic Process Optimization

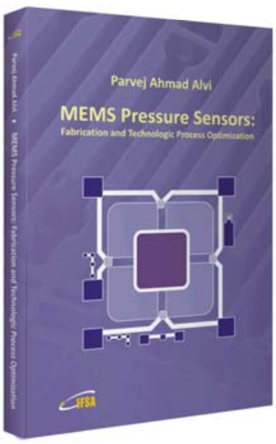

So far, no book has described the step by step fabrication process sequence along with flow chart for fabrication of micro pressure sensors, and therefore, the book has been written taking into account various aspects of fabrication and designing of the pressure sensors as well as fabrication process optimization. A complete experimental detail before and after each step of fabrication of the sensor has also been discussed. This leads to the uniqueness of the book.

Features include:

A complete detail of designing and fabrication of MEMS based pressure sensor.

- Step by step fabrication and process optimization sequence along with flow chart, which is not discussed in other books.
- Description of novel technique (lateral front side etching technique) in terms of chip size reduction and fabrication cost reduction, and comparative study on both the techniques (i.e. Front Side Normal Etching Technology and Front Side Lateral Etching Technology) for the fabrication of thin membrane.
- Discussion on issues of sealing of conical tiny cavity; because the range of pressure applied (i.e. greater or less than atmospheric pressure) can be decided by methodology of sealing of tiny cavity.
- A complete theoretical detail regarding aspects of designing and fabrication, and experimental results before and after each step of fabrication.

MEMS Pressure Sensors: Fabrication and Process Optimization will greatly benefit undergraduate and postgraduate students of MEMS and NEMS courses. Process engineers and technologists in the microelectronics industry including MEMS-based sensors manufacturers.

Hardcover: ISBN 978-84-616-2207-8
e-Book: ISBN 978-84-616-2438-6

Order: http://www.sensorsportal.com/HTML/BOOKSTORE/MEMS_Pressure_Sensors.htm

Sensors & Transducers, Vol. 273, Issue 2, June 2026, pp. 30-38

Sensors & Transducers
Published by IFSA Publishing, S. L., 2026
http://www.sensorsportal.com

Vehicle Localization Based on Roadside Object Detection Using YOLOv8

Takayoshi YOKOTA
Center for Data Science and Artificial Intelligence Education, Institute of Science Tokyo,
2 Chome-12-1 Ookayama, Meguro-ku, Tokyo 152-8550, Japan
Tel.: + 81 3 5734 2651
E-mail: yokota@dsai.isct.ac.jp

Received: 7 April 2026 /Revised: 13 May 2026 /Accepted: 10 June 2026 /Published: 29 June 2026

Abstract: This article proposes a vehicle localization method that enhances MEMS sensor-based self-localization by incorporating roadside object detections obtained from on-board camera images. Although conventional MEMS-based approaches have achieved meter-level accuracy, their performance degrades on roads with limited surface variations, leading to reduced robustness. To overcome this limitation, roadside objects such as traffic lights, traffic signs, and poles are detected using a fine-tuned YOLOv8m model and utilized as visual landmarks. The spatial configurations of the detected bounding boxes are matched with a reference dataset associated with RTK-GNSS positions, enabling correction of accumulated localization errors. This approach reduces dependency on road surface features and improves localization stability in diverse urban environments. Experimental results using real-world driving data demonstrate that the proposed method achieves improved robustness and maintains localization errors within approximately 3.13 m (mean), 0.42 m (median), 12.6 m (RMSE), and 111.8 m (maximum) under challenging conditions.

Keywords: Vehicle localization, MEMS sensors. RTK-GNSS, Object detection, YOLOv8m, Bounding box.

1. Introduction

Among vehicle localization algorithms [5–19], previous studies have applied cross-correlation to signals obtained from MEMS sensors to identify the best match with reference data recorded together with precise RTK-GNSS measurements [1, 2]. Although such approaches can achieve meter-level accuracy, their performance may degrade on smooth roads with limited surface variations, occasionally resulting in position errors of up to 10 m.

To compensate for this limitation, camera images captured during driving are exploited to extract additional environmental information. In this study, YOLOv8m, developed by Ultralytics [3], is applied to video sequences to detect roadside objects. The spatial distribution of the detected objects within each frame is then used as supplementary information for vehicle localization. YOLOv8 provides several model variants (v8n, v8s, v8m, v8l, and v8x) with different model sizes and computational costs. Among them, YOLOv8m offers a good balance between accuracy and computational efficiency, making it suitable for on-board applications, which are the target scenario of this study.

Since the standard 80 classes provided in the COCO dataset are insufficient to represent roadside landmarks relevant to localization, additional training data were collected and annotated. These data include traffic lights, traffic signs, trees, and other roadside structures.

Although many studies have utilized camera or LiDAR data for vehicle localization [4], relatively few have focused on self-localization methods that rely primarily on on-board sensors without external infrastructure. This work aims to bridge this gap by integrating visual landmark information with MEMS-sensor-based localization. This article is an extended version of the conference paper [1].

2. Vehicle Localization Algorithm Using Roadside Object Detection

Fig. 1 illustrates the overall processing flow. A video sequence captured by an on-board camera is processed using YOLOv8m, and the resulting object detections can be time-synchronized with measurements obtained from MEMS sensors, if available; however, no MEMS sensors are used in this study. The original COCO-80 label plays only a minor role in this study because many roadside objects suitable as landmarks are not included in the standard classes.

Therefore, YOLOv8m was fine-tuned using a custom dataset comprising seven classes of roadside objects: traffic lights, traffic signs, variable message signs (VMS), poles, trees, pedestrian bridges, and towers.

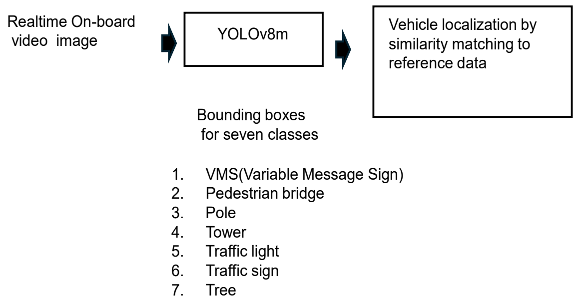

Fig. 1. Pipeline of the proposed vehicle localization method. YOLOv8m detects seven classes of roadside objects from real-time video images, and the vehicle position is estimated by similarity matching with reference data based on the detected bounding boxes.

$$\mathrm{Similarity}(F_i, F_j) = \frac{1}{\max(N_i, N_j)} \times \sum_{\substack{l \le N_i \\ m \le N_j,\, c_l = c_m}} \max\left\{\alpha\, e^{-\beta_1(|x_l - x_m| + |y_l - y_m|)} + (1-\alpha)\, e^{-\beta_2(|w_l - w_m| + |h_l - h_m|)}\right\} \tag{1}$$

The dataset was constructed from video recordings captured for approximately 40 minutes along an arterial road in Edogawa-ku, Tokyo, on August 20, 2024. Frames were sampled at 30-second intervals, resulting in a total of 76 images (60 for training and 16 for validation).

To compensate for the limited dataset size, data augmentation techniques provided by YOLOv8m – such as flipping, rotation, noise injection, and contrast adjustment – were applied, expanding the training set to 660 images (i.e., each original image was augmented to approximately ten images).

The model was trained for 600 epochs with a batch size of 8 on a desktop PC equipped with an NVIDIA RTX 4060 GPU. The dataset consists of 660 images, resulting in approximately 83 iterations per epoch with a batch size of 8. The training data were shuffled at the beginning of each epoch. The trained YOLOv8m model was then applied to recorded video frames. For each detected object, the bounding box parameters (x, y, w, h) and the corresponding class label were obtained. The timestamp for each frame was computed from the video metadata based on a frame rate of 29.97 fps and the video start time.

3. Matching the Bounding Boxes to the Reference Data

Bounding-box matching was performed using the similarity criterion defined in Eq. (1), which is computationally more efficient than pixel-level image correlation. To estimate the position of vehicles, the similarity between the bounding-box layouts of a target frame and those stored in a reference dataset was evaluated. Each reference frame contained a set of bounding boxes detected by the fine-tuned YOLOv8m model, along with the corresponding RTK-GNSS position. For each pair of frames, bounding boxes with identical class labels were matched. The similarity score was computed based on the positional and size differences between corresponding bounding boxes. The reference frame with the highest similarity score was selected as the most probable vehicle position, and the associated RTK-GNSS coordinates were adopted as the estimated position.

Let F_i and F_j denote image frames with frame indices i and j, respectively. N_i and N_j represent the numbers of bounding boxes in frames F_i and F_j.

The class labels of the bounding boxes are denoted by c_l and c_m, and l and m are indices of bounding boxes in each frame. The similarity function is defined as follows: The parameters were empirically determined as $\alpha = 0.7$, $\beta_1 = 0.002$, and $\beta_2 = 0.005$. The variables (x_l, y_l) denote the coordinates of the bounding-box l's center, while w_l and h_l represent the width and height of the bounding box l. All values are normalized by the image resolution of 960×540(original resolution: 1920×1080).

Although other similarity measures, such as Intersection over Union (IoU), could be used, the proposed greedy similarity function was adopted for computational efficiency, as it relies only on positional and size differences between bounding boxes.

4. Test Field and Experimental Setup

Field experiments were conducted on August 20, 2024, in Edogawa-ku, Tokyo, along National Route 14, also known as Shin-Ohashi-dori. A satellite image of the test course is shown in Fig. 2, where the evaluation section is indicated by a yellow arrow. The length of the evaluation section was approximately 1.75 km, and the travel time was about 300 s. The test vehicle was a Toyota Noah, a 2-liter, five-door minivan equipped with a GoPro HERO12 camera to capture video data during driving. Ground-truth vehicle positions were obtained using an RTK-GNSS receiver (u-blox ZED-F9P) [20], operating at 10 Hz with centimeter-level accuracy. Figs. 3 and 4 show the test vehicle and the RTK-GNSS receiver, respectively. The built-in electronic image stabilization function of the GoPro HERO12 was enabled.

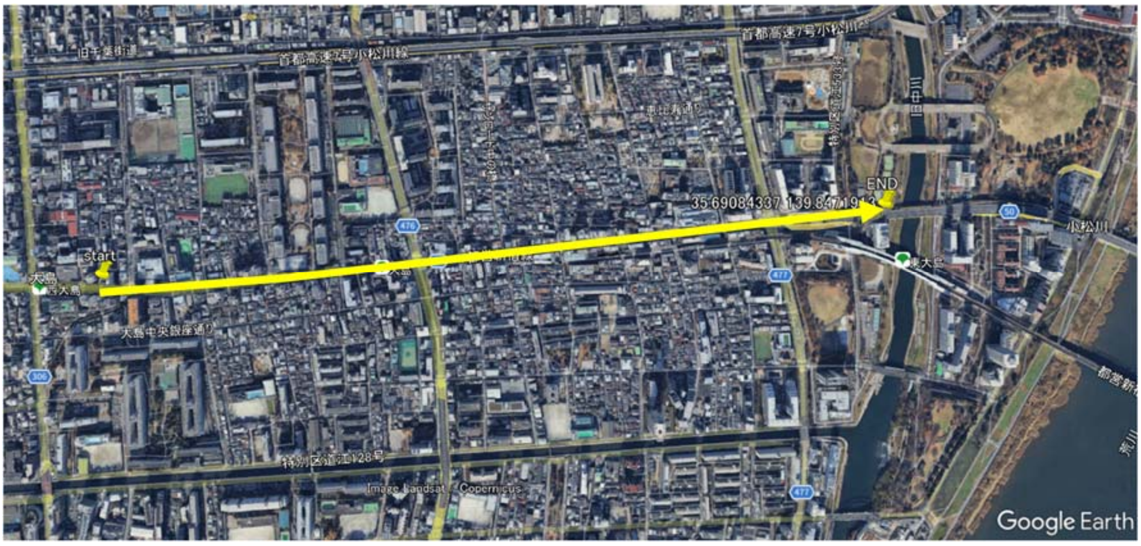

Fig. 2. Field test course. National road route 14 in Edogawa-ku, Tokyo, known as “Shin-ohashi-dori’. The length of the evaluation section is 1.75 km and is indicated by yellow arrow.

Fig. 3. Vehicle used for data collection (Toyota Noah, 2.0 L, 7-passenger capacity).

Fig. 4. RTK-GNSS receiver module (u-blox ZED-F9P) used for ground-truth position measurement in the field experiments.

Data acquisition for the section indicated by the yellow arrow was performed twice by driving along a circular course that included this section. The total travel time for the entire course was approximately 40 minutes. RTK-GNSS data, video images, and MEMS sensor data were acquired; however, the MEMS sensor data were not used in this article.

5. Details of Processing

5.1. Summary of YOLOv8m Training

Before presenting the vehicle localization results, a summary of the YOLOv8m training and validation process is provided. In the training phase of

YOLOv8m, still images were extracted from GoPro HERO12 video footage at 30-second intervals. The total number of images is 76. These images were divided into 60 training and 16 validation samples, and annotations were created using the cloud-based tool Label Studio [21].

Fig. 5 shows how the acquired images were used as training and validation data. The dataset was split into training (60 images) and validation (16 images) sets. Data augmentation increased the training dataset to 660 images.

Seven classes were defined as typical roadside objects: variable message signs (VMS), pedestrian bridges, poles, traffic lights, traffic signs, and trees. The frequency of each class in the training dataset is summarized in Fig. 6. As shown in the figure, the dataset is highly imbalanced, with the pole class being significantly overrepresented compared to the others. This imbalance is inherent to roadside environments and was therefore not corrected in this study.

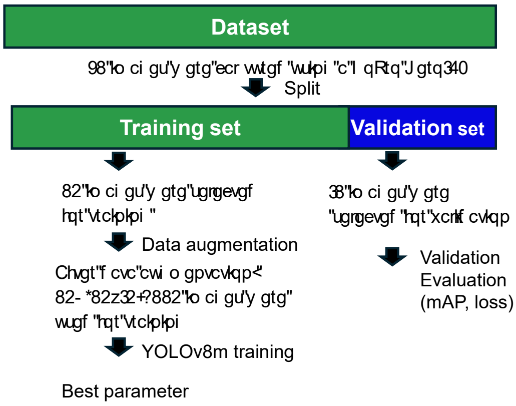

Fig. 5. Dataset preparation and training pipeline. The dataset was split into training (60 images) and validation (16 images) sets. Data augmentation increased the training data to 660 images. YOLOv8m was used for training and evaluation.

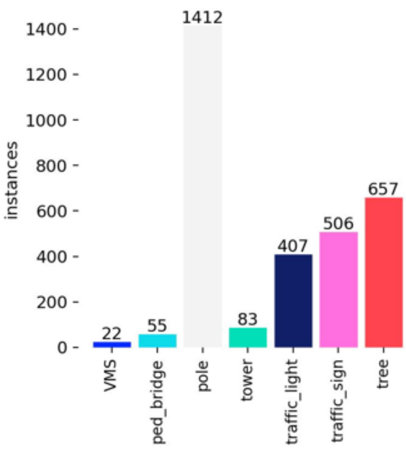

Fig. 6. Number of instances for each object class in the training dataset. The distribution is highly imbalanced, with the pole class being significantly more frequent than the other classes.

Despite this imbalance, the proposed method is applied to vehicle localization.

Table 1 shows the confusion matrix. Taking the pole class as an example, 21 out of 38 instances were correctly detected in the validation dataset, corresponding to a recall of approximately 55 %. In contrast, traffic signs were detected accurately (10 out of 10 instances). Overall, the object detection performance is limited, mainly due to the small dataset size and significant class imbalance. Although these issues are difficult to resolve, vehicle localization is performed using the detection results as they are.

Table 1. Confusion matrix of YOLOv8m object detection results on the validation dataset. A substantial number of objects, particularly poles, are misclassified as background, indicating a high false-negative rate. This degradation in performance is mainly attributed to dataset imbalance and the inherent difficulty of detecting small and thin objects.

Truth \ Prediction	VMS	ped_bridge	pole	tower	traffic_light	traffic_sign	tree	background
VMS								
ped_bridge		1						3
pole			21	1				14
tower								3
traffic_light					7			9
traffic_sign						10		6
tree							9	8
background		1	17	3	3		5	

Fig. 7 shows the training and validation loss curves over 600 epochs. The box regression loss (box_loss), classification loss (cls_loss), and distribution focal loss (dfl_loss) are presented for both the training and validation datasets. The training losses decrease steadily, while the validation losses exhibit slight fluctuations and gradually stabilize, indicating reasonable generalization performance given the limited dataset size. To examine the convergence behavior of YOLOv8m, the model was trained for up to 600 epochs. However, slight overfitting was observed after approximately 400 epochs. Therefore, considering computational efficiency, the model parameters corresponding to the best validation performance within the first 400 epochs were used for the vehicle localization step, as they provide comparable performance while reducing training cost.

5.2. Object Detection

Examples of object detection are shown in Figs. 8a, 8b, and Figs. 9a, 9b. After fine-tuning, the COCO-80 classes are rarely detected, while the newly defined seven classes become dominant.

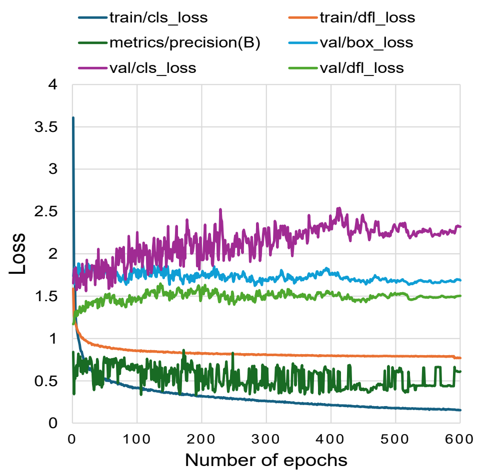

Fig. 7. Training and validation loss curves and precision during training. The training losses decrease steadily, while the validation losses remain higher and fluctuate, indicating possible overfitting. The precision gradually improves and stabilizes as training progresses.

Fig. 8a. YOLO detected image of the start point of the evaluation course. The first trip at 11:32:54.

Fig. 8b. YOLO detected image of the start point of the evaluation course. The first trip at 12:00:20.3.

Although the training is not perfect, the detection performance was moderately effective. The system outputs YOLOv8m object detection results in the form of bounding box attributes, including the class, width, height, and the x- and y-coordinates of the center position. YOLOv8m is sufficiently fast to detect objects in 29.97 fps HD video with a resolution of 1920 × 1080 pixels, while the images are downsampled to 960 × 540 for efficient processing.

Figs. 8a and 8b show snapshots of the video images captured at the same location but at different times of day and during different trips. The detected bounding boxes are overlaid on the images. Figs. 9a and 9b show the corresponding bounding-box-only representations. Since the images differ only in transient objects such as vehicles, the bounding-box representations remain highly similar. Consequently, the spatial layouts of the bounding boxes are also highly similar, leading to a high similarity in their spatial distributions. The proposed similarity matching procedure operates on these bounding-box representations rather than raw pixel data, eliminating the need for pixel-wise processing and enabling efficient computation.

Fig. 9a. YOLO detected bounding box only image of the start point of the evaluation course. The second trip at 11:32:54.

Fig. 9b. YOLO detected bounding box only image of the start point of the evaluation course. The second trip at 12:00:20.3.

To generate reference data, object detection results during the reference data acquisition phase are augmented with precise location information (latitude and longitude) and accurate time stamps, as illustrated in Fig. 10. The latitude and longitude are estimated by interpolating the 10 Hz RTK-GNSS data to match the 29.97 Hz video sampling rate. The interpolated positions are then associated with the corresponding YOLO-detected objects, forming a time-aligned reference dataset.

Since RTK-GNSS provides more accurate timestamps than the video camera, the alignment is performed using the GNSS timestamps. A precise calibration is subsequently applied to refine the alignment.

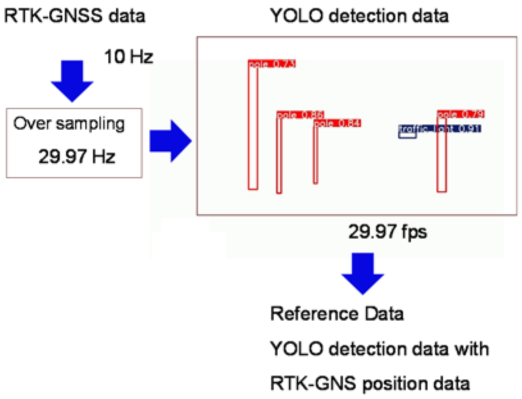

Fig. 10. Overview of the mapping process between object detection results and video frames. Detected roadside objects (left) are associated with corresponding bounding boxes in the video frames (center), which are sampled at 29.97 fps. This temporal alignment enables the conversion of detection results into a continuous time series for subsequent matching and localization.

6. Results and Discussion

6.1. Results of Similarity Matching

The results of bounding-box similarity matching are shown in Figs. 11a and 11b, which illustrate the relationship between the running times of the target vehicle and the reference vehicle. Each point represents a correspondence obtained by matching objects using the proposed similarity function, where the best similarity is selected for each time step of the target vehicle. The matching is performed frame by frame. The solid line indicates the estimated temporal alignment between the two vehicles derived from these correspondences. The step-like structure reflects differences in vehicle motion, such as stop-and-go behavior, and the dispersion of points indicates matching uncertainty. Despite the presence of outliers, the overall trend accurately captures the temporal alignment between the two vehicles. Fig. 11a shows the result using the best YOLOv8m weights after 100 epochs, whereas Fig. 11b presents the result using the best YOLOv8m weights after 400 epochs. The results are comparable, indicating that 100 epochs are sufficient to achieve reliable estimation of the temporal difference between the reference and target vehicles.

Fig. 11c presents the result after applying a median filter to the result of Fig. 11b.

Fig. 12 shows the ground truth of the temporal difference between the reference and target vehicles obtained using RTK-GNSS. Both vehicles were equipped with RTK-GNSS, and their precise positions were used to compute the temporal difference when they were at the same location. The sampling rate of RTK-GNSS was 10 Hz, whereas the video frame rate was 29.97 fps. Therefore, interpolation and oversampling were applied to obtain location data at 29.97 Hz.

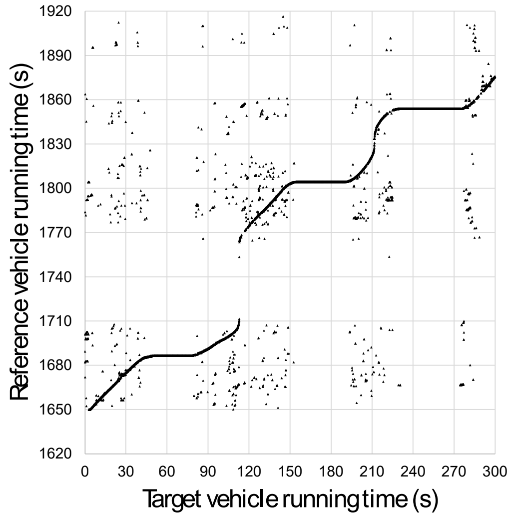

Fig. 11a. Results of bounding-box similarity matching using the best model obtained after 100 epochs.

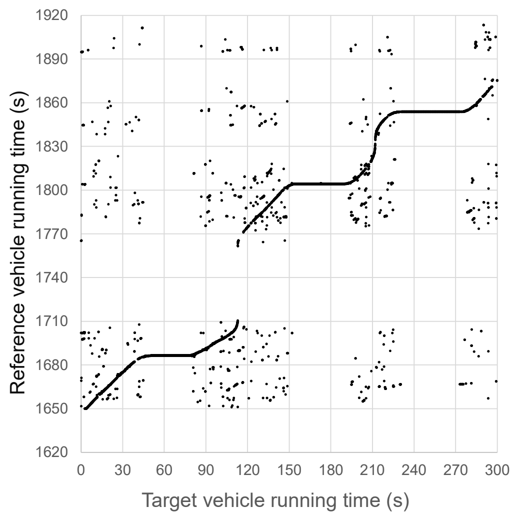

Fig. 11b. Results of bounding-box similarity matching using the best model obtained after 400 epochs.

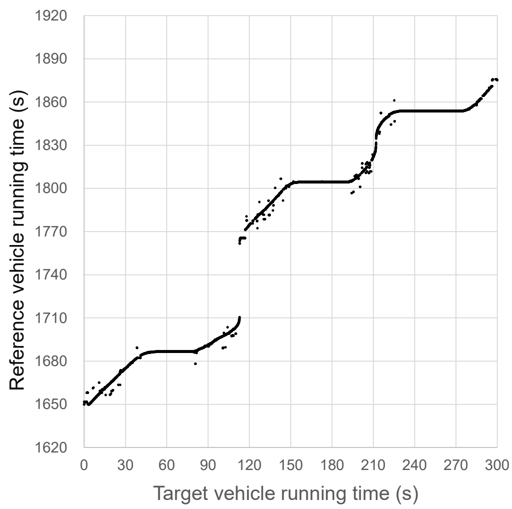

Fig. 11c. Results after median filtering of the bounding-box similarity matching using the best model obtained after 400 epochs.

By comparing Figs. 11a and 11b with Fig. 12, it can be observed that the temporal difference is estimated with high accuracy, although some spike noise remains.

6.2. Results of Location Estimation

Fig. 13 shows the results of position estimation. Fig. 14 shows the cumulative distribution of the position error. The error distribution exhibits higher kurtosis than a Gaussian distribution, with approximately 84.4 % of the errors within 2 m, 92.7 % within 5 m, and 95 % within 10 m, while a small number of outliers exceeding 20 m are observed.

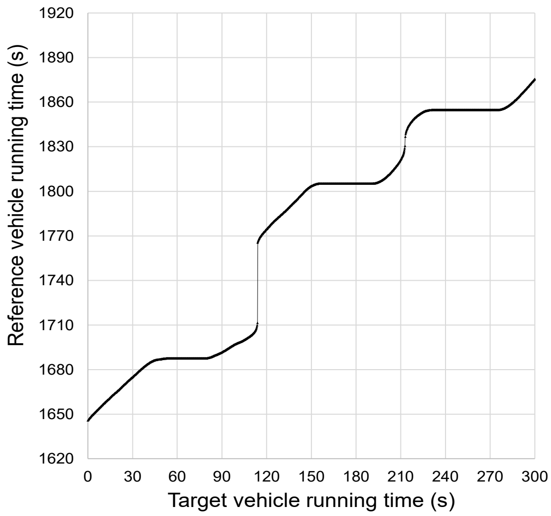

Fig. 12. Ground truth of the temporal difference between the target and reference vehicles.

Table 2 summarizes the error statistics. Although occasional large-error spikes are observed, the overall error distribution remains narrow.

Fig. 15 shows the directional distribution of the position error. The position errors in the east–west and north–south directions are concentrated near the origin, while larger errors exhibit a correlated trend in both directions, reflecting the constraint of the reference trajectory along the road geometry.

The maximum error is mainly caused by occasional spike errors in the similarity matching of detected object frames. In most cases, the error remains within several meters, demonstrating the effectiveness of the proposed method. These spike errors can be mitigated by integrating a dead-reckoning approach.

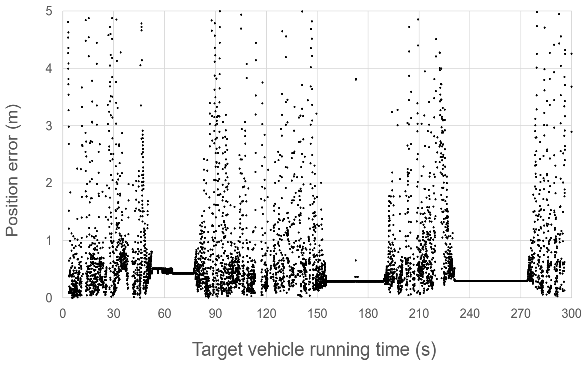

Fig. 13. Position error over time for the target vehicle. The horizontal axis represents the running time of the target vehicle, while the vertical axis shows the position error with respect to the reference trajectory. The error remains within several meters for most of the duration, with occasional spikes caused by mismatches in object detection.

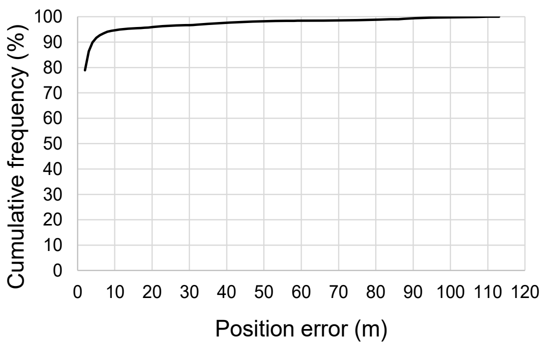

Fig. 14. Cumulative distribution of position error. Approximately 84.4 % of the errors are within 2 m, 92.7 % within 5 m, and 95 % within 10 m, while a small number of outliers exceeding 20 m are observed.

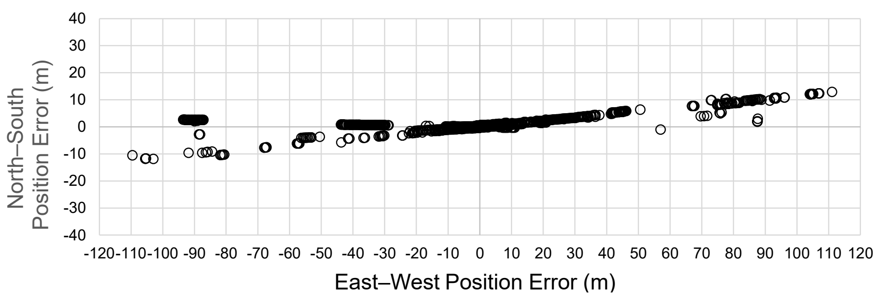

Fig. 15. Scatter plot of east–west and north–south position errors. Most errors are concentrated near the origin, while larger errors exhibit a correlated trend in both directions, reflecting the constraint of the reference trajectory along the road geometry.

Although dead reckoning inherently accumulates errors over time, its combination with the proposed method, which provides reliable absolute position estimates, can significantly enhance localization robustness and stability. Moreover, integrating a MEMS sensor-based localization algorithm can further compensate for the limitations of the proposed approach.

Table 2. Summary of the position estimation error.

Average error	3.13 m
Median error	0.42 m
RMSE	12.6 m
Max error	111.8 m

7. Conclusions

This article presents a vehicle localization algorithm based on the spatial arrangement of bounding boxes obtained from on-board camera images. In an experiment conducted on a 1.7 km arterial road section, the results demonstrate that incorporating roadside object detections improves localization robustness under challenging conditions. The estimated location error was 3.13 m on average, with approximately 84.4 % of errors within 2 m, 92.7 % within 5 m.

The proposed approach can also be extended to pedestrian localization scenarios where only camera images are available. Consequently, the method has the potential to support navigation in GNSS-denied environments, such as urban canyons and mountainous regions, provided that suitable visual landmarks are available.

Future improvements in YOLO training and model optimization are expected to further enhance the reliability and accuracy of the position estimation.

Acknowledgements

This work was supported in part by JSPS KAKENHI Grant Number JP25K15360.

References

[1]. T. Yokota, Roadside object detection-based vehicle localization, in *Proceedings of the 6th Winter IFSA Conference on Automation, Robotics & Communications for Industry 4.0/5.0/6.0 (ARCI)*, 2026, pp. 20-23.

[2]. T. Yokota, Vehicle localization algorithm with lane discrimination based on inertial and geomagnetic sensor data for GNSS-denied environments and its evaluation for different vehicles and drivers, *Sensors & Transducers*, Vol. 268, Issue 1, 2025, pp. 19-27.

[3]. Ultralytics, YOLOv8, https://github.com/ultralytics/ultralytics

[4]. S. Li, H. S. Yoon, Vehicle localization in 3D world coordinates using a single camera at traffic intersection, *Sensors*, Vol. 23, Issue 7, 2023, 3661.

[5]. T. Yokota, Network-wide vehicle localization algorithm based on MEMS sensor data, *Sensors & Transducers*, Vol. 265, Issue 12, 2024, pp. 17-26.

[6]. T. Yokota, Vehicle localization by correlated MEMS sensor data with velocity compensation, in *Proceedings of the 26th IEEE International Conference on Intelligent Transportation Systems (ITSC)*, 2023, pp. 2999-3004.

[7]. T. Yokota, T. Yamagiwa, Vehicle localization by optimally weighted use of MEMS sensor data, in *Proceedings of the 3rd IFSA Winter Conference on Automation, Robotics & Communications for Industry (ARCI)*, 2023, pp. 79-84.

[8]. T. Yamagiwa, T. Yokota, Vehicle localization method based on MEMS sensor data comprising pressure, acceleration and angular velocity, in *Proceedings of the IEEE International Conference on Mechatronics and Automation (ICMA)*, 2022, pp. 748-753.

[9]. T. Yokota, Vehicle localization by altitude data matching in spatial domain and its fusion with dead reckoning, *International Journal of Mechatronics and Automation*, Vol. 8, Issue 4, 2021, pp. 208-216.

[10]. T. Yokota, Vehicle localization by dynamic programming from altitude and yaw rate time series acquired by MEMS sensor, *SICE Journal of Control, Measurement, and System Integration*, Vol. 14, Issue 1, 2021, pp. 78-88.

[11]. T. Yokota, Vehicle localization based on MEMS sensor data, in *Proceedings of the 60th Annual Conference of the Society of Instrument and Control Engineers of Japan (SICE)*, 2021, pp. 1105-1110.

[12]. T. Yokota, Localization algorithm based on altitude time series in GNSS-denied environments, in *Proceedings of the 59th Annual Conference of the Society of Instrument and Control Engineers of Japan (SICE)*, 2020, pp. 985-990.

[13]. T. Yokota, Y. Hashimoto, T. Yamamoto, H. Yoshii, Fast and robust map-matching algorithm based on a global measure and dynamic programming for sparse probe data, *IET Intelligent Transport Systems*, Vol. 13, Issue 11, 2019, pp. 1613-1623.

[14]. J. Tsurushiro, T. Nagaosa, Vehicle localization using its vibration caused by road surface roughness, in *Proceedings of the IEEE International Conference on Vehicular Electronics and Safety (ICVES)*, 2015, pp. 164-169.

[15]. A. J. Dean, R. D. Martini, S. N. Brennan, Terrain-based road vehicle localization using particle filters, *Vehicle System Dynamics*, Vol. 49, Issue 8, 2011, pp. 1209-1223.

[16]. E. Laftchiev, C. Lagoa, S. Brennan, Terrain-based vehicle localization from real-time data using dynamical models, in *Proceedings of the 51st IEEE Annual Conference on Decision and Control (CDC)*, 2012, pp. 3366-3371.

[17]. J. Gim, C. Ahn, Ground feature-based vehicle positioning, in *Proceedings of the 59th Annual Conference of the Society of Instrument and Control Engineers of Japan (SICE)*, 2020, pp. 983-984.

[18]. J. Gim, C. Ahn, IMU-based virtual road profile sensor for vehicle localization, *Sensors*, Vol. 18, Issue 10, 2018, 3477.

[19]. X. Qu, B. Soheilian, N. Paparoditis, Landmark-based localization in urban environment, *ISPRS Journal of Photogrammetry and Remote Sensing*, Vol. 140, 2018, pp. 90-103.

[20]. u-blox, ZED-F9P GNSS module, https://www.u-blox.com/en/product/zed-f9p-module

[21]. HumanSignal, Label Studio, https://labelstud.i

Published by International Frequency Sensor Association (IFSA) Publishing, S. L., 2026 (http://www.sensorsportal.com).

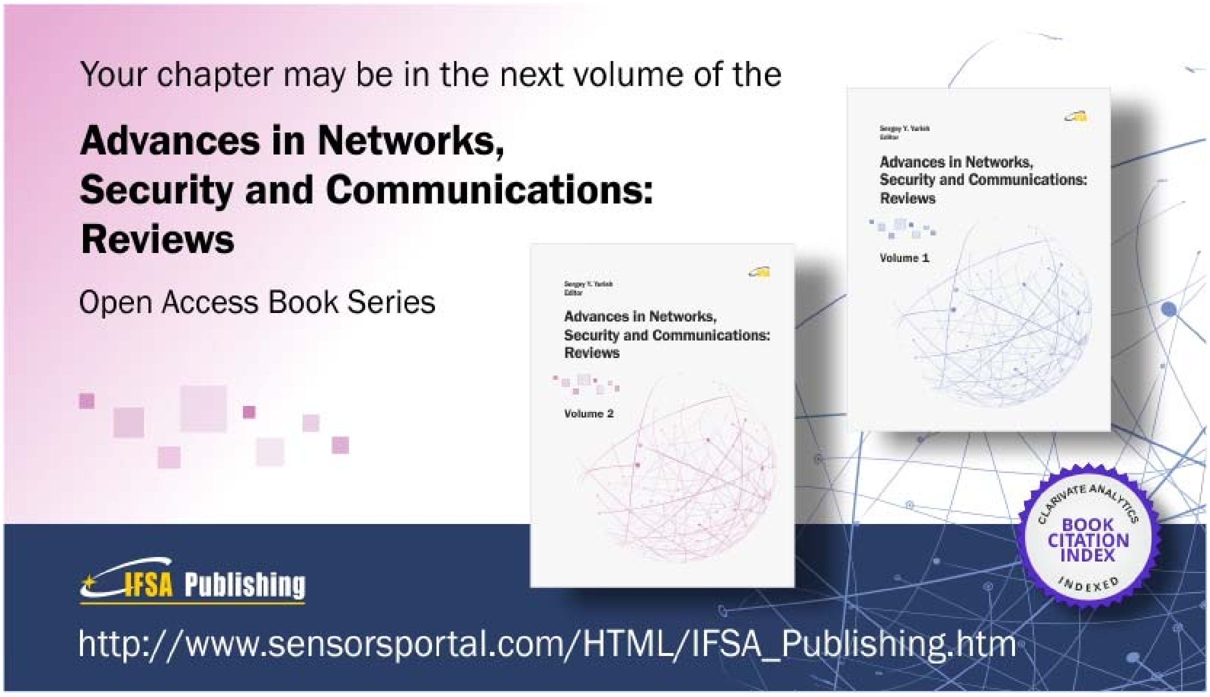

Sensors & Transducers, Vol. 273, Issue 2, June 2026, pp. 39-49

Sensors & Transducers
Published by IFSA Publishing, S. L., 2026
http://www.sensorsportal.com

Automated Mission Planning for Mobile Robots Using Building Information Modeling (BIM) and Digital Twins

**[1] Annamria ARNOUK, [1] Martin BEHM, [1] Christian BORCK,
[2] Tim HOFFMANN, [2] Florian DIETRICH, [2] Matthias MELZER,
and [2, *] Jan DÜNNWEBER**
[1] Brandenburgische Technische Universität Cottbus – Senftenberg, Germany
[2] Ostbayerische Technische Hochschule Regensburg, Germany
[2] Tel.: +49 941 943-7186
[*] E-mail: jan.duennweber@oth-regensburg.de

Received: 8 April 2026 /Revised: 20 May 2026 /Accepted: 5 June 2026 /Published: 29 June 2026

Abstract: This article presents a conceptual framework for automated mission planning of mobile robots in smart factory environments, integrating Building Information Modeling (BIM) with industrial digital twins. Our first contribution is BIM2Robot, an open-source framework that systematically transforms building models, given in a standards-compliant IFC description, into a ROS-compatible topological navigation graph including a geometric environment model and an executable mission plan, enabling Automated Guided Vehicles (AGVs) to be deployed in the described building without manual waypoint definitions. The second contribution is the Assembly Twin, a production digital twin built on NVIDIA Omniverse that integrates design and process data from PLM and ALM platforms, real-time sensor streams via the Adaptive Framework for Optical Sensors (AFOS), and AI-based assembly monitoring via the Confirmation and Tacit Data System (CTDS). The Assembly Twin provides real-time worker guidance through extended reality interfaces and continuously tracks workbench states and production progress. The integration of both systems establishes a closed loop between production intelligence and robot navigation: When the Assembly Twin detects a production disruption, such as an unexpected workbench failure, it runs a script provided by the BIM2Robot framework that generates an updated mission plan and reroutes the affected AGV(s) autonomously. Relying on open standards including IFC, USD and OPC UA, the combined framework is adaptable and accommodates continuous changes in the workplace layout. Generating robot code directly from a building model eliminates the need for manual reconfiguration. Combined with a live digital twin of the assembly hall, AGVs benefit from a continuously synchronized understanding of both the static geometry and the dynamic production state, enabling context-aware navigation decisions that transcend purely geometric path planning.

Keywords: Robot motion planning, Digital twins, Assembly automation, Building Information Modeling (BIM), Robot Operating System (ROS 2), Robot programming methodology, Code generation.

1. Introduction

In modern smart factories, manual and automated manufacturing processes are deeply intertwined to ensure high efficiency, quality, and flexibility. Central to this environment are interconnected workbenches that serve as pre- and end-assembly stations, including integrated quality control. At these stations, operators are supported by worker guidance systems utilizing smart sensors, machine vision, and digital twins to execute complex assembly tasks. To sustain this production process, a seamless flow of inbound and outbound components is required, which is typically facilitated by Automated Guided Vehicles (AGVs) handling the intralogistics between workbenches.

However, maintaining continuous operation in such dynamic environments poses significant challenges, particularly when the manufacturing process is impacted by unforeseen events. Two frequently occurring scenarios highlight the limitations of current static production systems:

First, unexpected failures can disrupt the workflow. If a workbench goes offline unexpectedly – for example, due to a broken tool – the production process must be rerouted dynamically. Components currently in transit or waiting must be swiftly transferred to alternative workbenches via AGVs to minimize idle times and prevent bottlenecks.

Second, the concept of a living shopfloor introduces continuous spatial and logistical changes. Modifications in the shopfloor layout directly influence intralogistics. Consequently, AGVs and mobile robots must autonomously find new routes to meet their objectives. This requires the system to constantly update and understand environmental models and contextual data to identify the exact start and goal locations of components, as well as the newly designated stations for assembly and warehousing.

To address these scenarios, this article proposes a novel framework that bridges the gap between dynamic production management and robot spatial planning by combining two approaches to automation: the Assembly Twin, implemented via NVIDIA Omniverse, and the open-source framework Robot BIM (BIM2Robot). While the Omniverse-based Assembly Twin acts as the cognitive core for the production process – managing real-time workbench states, worker guidance, and the dynamic rerouting of tasks – BIM2Robot provides the semantic and geometric understanding of the facility. By automatically translating standardized Building Information Models (IFC) and spatial annotations into ROS-compatible mission plans, the system ensures that AGVs can instantly adapt to living shopfloor changes.

In combination, the two technologies establish a resilient, fully synchronized manufacturing environment where both the production logic and the ROS-driven mobile robots act on a shared, real-time understanding of the factory floor. This article integrates and extends two prior conference papers. The first introduced the Assembly Twin as a production digital twin for real-time worker guidance and workbench monitoring [1]. The second presented BIM2Robot as a code generation framework for IFC-based robot navigation [2].

The remainder of this article is organized as follows. In Section 2, we discuss related work on factory automation with digital twins and on indoor path planning for robots. Section 3 uses the case study of producing aircraft drives to highlight features of our Omniverse-based Assembly Twin. In Section 4, we explain how BIM2Robot facilitates automatic path planning in a factory hall. Section 5 shows how an automated factory benefits when a digital twin is combined with a robot mission plan derived from the building description, using failure recovery as a possible use case. Finally, in Section 6 we conclude the article with an outlook on future work.

2. Related Work

Manufacturing digital twins have evolved into connected components of immersive environments referred to as the industrial metaverse. Siemens connected its Xcelerator platform with NVIDIA Omniverse in 2022 [3] and later added OpenUSD [4] support to Teamcenter X, letting engineering teams collaborate in a shared 3D environment [5]. Dassault Systèmes follows a different path with its 3DEXPERIENCE platform, where the DELMIA division provides virtual manufacturing planning and process optimization across the product lifecycle [6]. Where Siemens uses OpenUSD [4] as its interoperability layer, Dassault relies on IFC and STEP. NVIDIA Omniverse serves as a platform for physically accurate digital twins. Its USD (Universal Scene Description [4]) scene graph lets assets from CAD, BIM, and simulation tools be combined [7].

2.1. Digital Twins in Manufacturing

A virtual commissioning methodology was proposed to integrate digital twins into a flow-shop manufacturing system, validating digital-twin-driven reactive scheduling in response to machine breakdowns before physical deployment [8]. Furthermore, fourteen open-source digital twin frameworks were compared, showing that no single framework covers all needs, so practitioners often combine multiple frameworks [9]. Among these, Eclipse BaSyx implements the Asset Administration Shell aligned with RAMI 4.0, which is relevant here, as our earlier RAMI4.0-based asset combination [10] took a similar layered approach to connect sensing and context generation to the visualization layer.

XR-based worker guidance in manual assembly is closely related to the architecture presented in this article. XR applications across assembly stages were reviewed from a human-centric Industry 5.0 perspective, mapping benefits at the operator, enterprise, and industry level [11]. For tracking assembly progress without manual input, YOLO-based object detection was combined with pose estimation to recognize repetitive worker actions, achieving 92.8 % recognition accuracy [12]. Zero-shot or few-shot models extend this capability by generalizing unseen objects without retraining, relying only on reference images and CAD models. This property is relevant for high-variability production where components change frequently.

Our architecture builds on two research threads from the COCKPIT4.0 and DIREKT projects. A modular pipeline for mixed reality environments was built to structure visualization assets from different sources into reusable workflows [11]. Furthermore, a RAMI4.0-based asset combination was proposed to connect AFOS, CTDS, EAS, and VIS as coordinated assets for operating a digital twin in human-centered assembly [8]. Building on this RAMI4.0-based asset combination, our earlier work advanced this foundation toward an Omniverse-based Assembly Twin for manual assembly. The study did not redefine the RAMI4.0 architecture itself; rather, it transferred this earlier conceptual basis into a concrete digital-twin environment centered on NVIDIA Omniverse, with a particular focus on the visualization layer. Its added contribution was the real-time integration of design and production data streams, the organization of assembly states through USD scene hierarchies and sublayers, and the coupling of AI-based tracking with XR-based worker guidance. A twin for manual production, as both works showed, requires a pipeline with sensing, context interpretation, and operator feedback. We extend this toward the industrial metaverse with USD-based scene composition, synchronized design and production twins, and XR-based guidance. To keep the spatial model current, the Environment Acquisition System (EAS) [8], a mobile robot equipped with LiDAR, acceleration, and RGBD sensors, is used. The joint use case of component commissioning across multiple workstations with load-dependent rerouting requires both this up-to-date spatial model and robot navigation between stations. For this purpose, we consider the derivation of navigation plans from BIM data.

2.2. BIM and Robot Path Planning

Mobile robots increasingly reduce the reliance on manual labor in logistics [13]. Transferring existing robotic solutions to new facilities, however, remains a persistent challenge, as environmental models, navigation graphs, and waypoint structures are typically tied to specific floor layouts and require substantial redesign effort when the environment changes [14].

BIM data provides structured sources of environmental information for robotic systems. In the construction domain, sensor data has been aligned with geometric information from IFC files to improve robot localization accuracy [15], and IFC-based semantic building models have been used to support robot task planning and execution in built environments [16].

More recent work demonstrates that the direct generation of robot-specific navigation maps from BIM data reduces computational overhead, compared to traditional SLAM-based navigation. BIM data also include high-level semantic descriptions of building structures, thereby enabling robots to navigate with greater autonomy [17]. Object detection techniques have also been integrated with BIM data to initialize pathfinding strategies in unknown environments [18], and ontology-based building models have been proposed to categorize building elements and their functionality for inspection tasks [19].

Beyond the BIM domain, digital building twins, created, e.g., via 3D laser scanning, have been applied to support indoor localization across multiple user platforms, demonstrating the broader relevance of semantically enriched environment models for robot navigation [20]. Model-driven approaches to robot programming have demonstrated the potential of generating application code directly from formal models [21].

In contrast to these concepts, where BIM data serves as a supplementary geometric information source or requires manual enrichment of building elements with robot-specific instructions, BIM2Robot uses the standardized building model itself as the primary source for new robot applications. Building on our previously proposed concept [22], the framework systematically transforms IFC descriptions into topological navigation graphs, geometric environment models, and executable mission plans through a structured parsing pipeline. BIM2Robot bridges the gap between descriptive building models and executable robot programs without requiring proprietary map files or waypoint definition.

3. Assembly Twin: Our Architecture for Digital Twins in Manual Assembly

Our proposed assembly digital twin architecture is shown in Fig. 1.

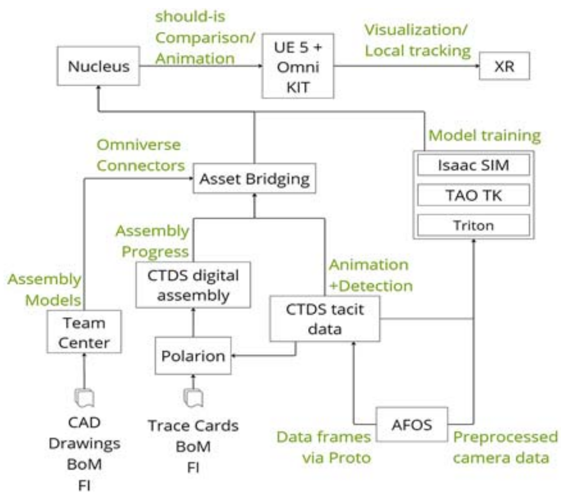

Fig. 1. Reference architecture.

3.1. Methodology for Real-Time Integration of Design and Production Digital Twins

All technological components are built around NVIDIA Omniverse as the central integration environment [23].

3.1.1. Technological Framework

The main components of our Assembly Twin are Omniverse Nucleus [24], Omniverse Kit, used for project-specific extensions [25], and software-specific connectors that enable synchronization between heterogeneous tools and data sources [26].

Sensor data is acquired via the Adaptive Framework for Optical Sensors (AFOS) [10]. The Confirmation and Tacit Data System (CTDS) processes assembly progress and implicit signals like time expenditure.

At the design level, BIM authoring environments, such as Autodesk Revit [27], can be integrated through Omniverse connectors. Connector-based synchronization is particularly relevant, since changes in the BIM model can be propagated to Omniverse applications.

Augmented reality (AR) and extended reality (XR) interfaces are available to factory workers and can close the loop between digital planning and physical execution. This is helpful for validating manual steps or for guiding workers based on operator behavior.

3.1.2. Data Acquisition and Transfer Pipeline

Our data integration pipeline is shown in Fig. 2. We explain its components using motor assembly as an example. Production-related information such as composition rules, Computer-Aided Design (CAD) models, and bills of materials (BOM) are retrieved from cloud-based Product Lifecycle Management (PLM) platforms, such as Teamcenter, and from Application Lifecycle Management (ALM) platforms, such as Polarion, through dedicated Omniverse connectors. Additional inputs include post-processed simulation models and animation sequences generated in Visual Components, 3ds Max, or Blender. Scanned physical prototypes can also be integrated into the pipeline.

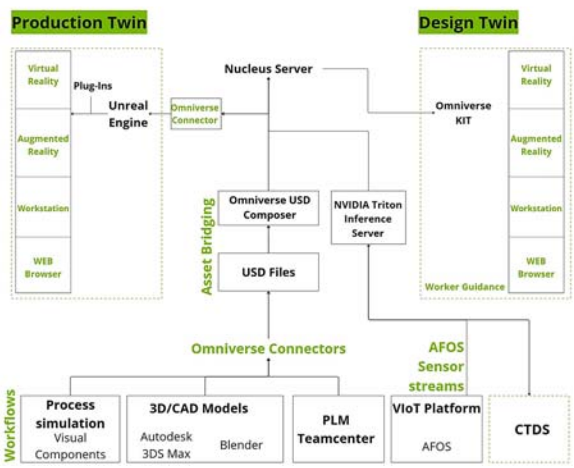

Fig. 2. Modular frameworks for mixed reality environments.

At the physical workspace level, the Adaptive Framework for Optical Sensors (AFOS) as a visual IoT platform provides a decentralized infrastructure for the integration of a strategically positioned camera system on the workbench consisting of two Orbbec Femto Bolt RGBD cameras. It also enables the creation of distributed data pipelines to allow real-time big data preprocessing of the camera streams including data fusion, e.g. for colored point cloud creation, multi-camera synchronization and the publication of the result to other applications via gRPC (Remote Procedure Calls). These data streams, combined with CAD assets from Teamcenter, feed into the Confirmation and Tacit Data Acquisition System (CTDS), which employs deep learning models to track worker actions and identify assembly deviations. Afterward, structured data flows into a centralized database optimized for cross-disciplinary collaboration. The high-fidelity digital twin, rendered in real-time, serves as the backbone of this knowledge base, delivering it to the operator through XR-enabled devices. The assembly information from Polarion is compared in order to check the sequence of the activities performed.

At the same time, the system automatically records the best fitting activities or delays from workers, improving the ideal time needed for each step and identifying when it takes too long, which helps to continuously improve the workflow using data. Beyond operational guidance, the digital environment serves as an immersive training platform, enabling operators to rehearse tasks in a risk-free virtual setting, thereby accelerating skill acquisition and increasing task confidence.

The same pipeline is used for the design digital twin and the production digital twin, with significant differences in the data feed and features, as shown in Table 1.

Table 1. Functional comparison between design and production digital twins.

Feature	Design Digital Twin	Production Digital Twin
Phase	conceptual/ pre-production	in-operation/ execution
Source of Data	PLM, ALM (Fitting Instructions), EAS (environment scan)	AFOS + CTDS (real-time sensor & ML input), ALM (Trace Cards)
Purpose	Simulation, Layout validation	Process validation, live monitoring
Dynamics	Static or versioned (e.g. planned state)	Dynamic and continuously updated
Usage	Virtual commissioning, planning	Monitoring, feedback, worker assistance

3.2. Automated Compositing

We present an overview of the detection logic for assembly monitoring, USD-Sublayer configuration and stage control via Extensions, bridging the gap between digital representations and manual execution. As an example, we discuss the assembly of electric aircraft propulsion systems for a hybrid engine stator.

3.2.1. Use Case Description: Digital Twin for Hybrid Aircraft Drive Assembly

The Nucleus Workstation serves as our local Omniverse server, which represents all application objects using the standard USD format and gives us access to the control infrastructure. It enables collaborative interactions with USD assets through tools like USD Composer, Isaac Sim and various third-party applications through dedicated connectors and custom extensions. The Omniverse USD API wrappers allow us to aggregate diverse data sources into a multi-layered USD hierarchy, as illustrated in Fig. 3. Modular Scene composition in Omniverse Composer. Layers stack assets, animations, or modifications, with higher layers overriding lower ones where necessary to assemble a cohesive scene.

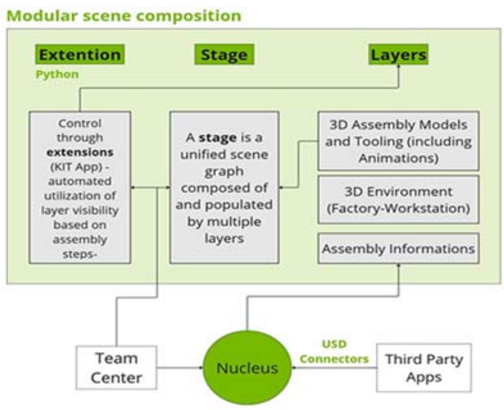

Fig. 3. Modular Scene composition in Omniverse Composer.

The USD structure mirrors the physical assembly hierarchy: Each assembly level is represented as an Xform, which is a scene node controlling the position, rotation and scale of its children. Mechanical relationships are reflected via nesting. In the aircraft use case, e.g., screw tightening operations are nested within the motor subassembly. Sublayers define assembly progression (“aircraft base frame installed”) and bundle the 3D models required for each step. This modular approach supports animation integration (e.g. training systems toggling sublayer visibility to guide assembly workflows) and environmental elements (e.g. workbenches, manufacturing floors to support XR training environments and increase immersion), which are added as compressed payloads to balance detail and performance. Additionally, fitting instructions extracted from trace cards outlining the assembly steps can be integrated as custom USD metadata, including positioning and textual information in USD format.

Our architecture clearly separates design concerns encompassing CAD data, assembly logic, and animation workflows, from operating aspects driven by sensor inputs, contextual inference, and operator guidance.

3.2.2. Increased Factory Performance with AGVs

Each workbench display presents the relevant 3D views of the aircraft drive to the respective workers without requiring their intervention. The assignment of assembly stages to the workers is configured in our worker assistance system built upon the Omniverse USD Composer App Template (from the “kit-app-template”toolkit[1]) with KIT extensions [28-30].

These extensions facilitate the end-to-end monitoring of the aircraft drive assembly, and also the cooperation between automated guided vehicles (AGVs) and our Assembly Twin. AGVs are provided with stage position data from the factory OPC UA server and send back their locations, allowing their visualization within the 3D scene in real time.

While the Assembly Twin monitors AGVs, it does not maintain a spatial model of the factory from which navigation plans for the AGVs are derived from. Such plans that govern how AGVs physically move, which doors are passed, and which rooms are traversed must be provided by an external system.

Despite the added complexity, the use of AGVs is worth considering since they significantly contribute to the performance of processes such as component commissioning, which is time-critical in the aircraft drive assembly use case. The AGVs distribute parts across pre-assembly and end-assembly workstations taking the current machine loads into account. The real-time visualization of this process allows operators and facility managers to observe this load-balancing behavior within the digital twin. Adapting to layout changes requires deriving new, executable navigation programs reflecting the physical reconfiguration. Generating such routes from a revised floor plan is outside the scope of the Assembly Twin.

The visualization remains continuously synchronized with the factory workflows, as the KIT event message bus toggles the relevant sublayers to reflect the corresponding transition, whenever the completion of a step is detected. The fitting instructions for the following step are then rendered using the Omni.UI API, and the corresponding assembly-state animation is initiated.

3.2.3. AI-Powered Guidance

The AI-based guidance subsystem provides operators and facility managers with a live view of the assembly state at each workstation, including the steps required for completion and real-time feedback during the assembly process. Zero-shot and few-shot models allow process-agnostic analysis, reducing the need for

[1] Version 106.5-109.3

retraining when components or assembly sequences change. The AI-powered action detection and worker guidance components are shown in the right part of the architecture diagram in Fig. 4.

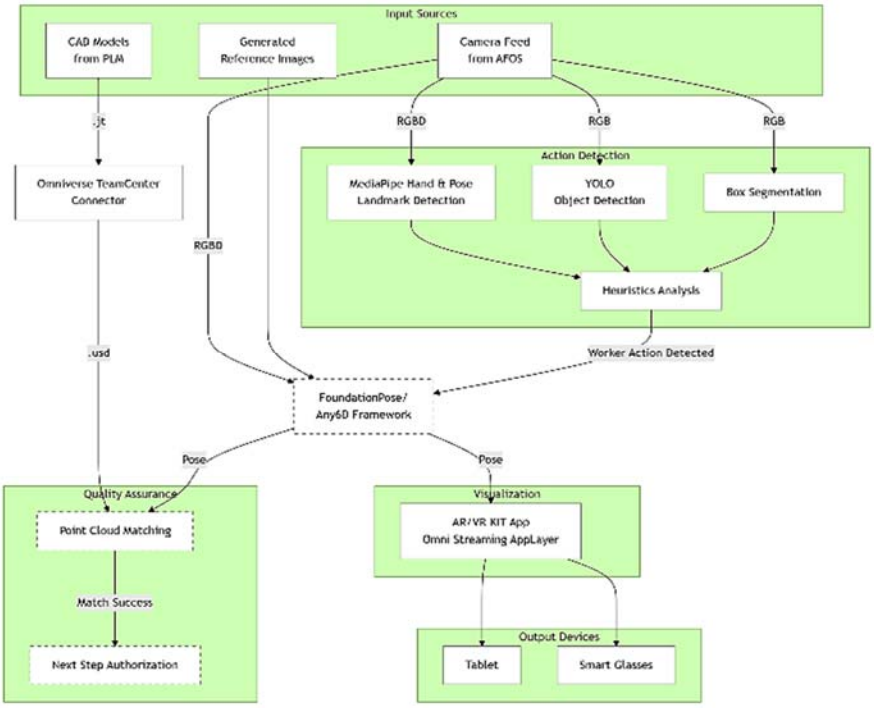

Fig. 4. AI-Powered Assembly Twin Components.

When a worker begins an action, MediaPipe Hands [31] detects the corresponding state transition. For reliable action detection, our movement tracking includes lift-off distances, workbench zones, hip-to-arm distances, and wrist-elbow-shoulder angle ratios. From this data, observed movements are classified. Hand proximity to commission boxes indicates, e.g., grasping events.

Object detection is performed with YOLO11 to verify that the required components have been retrieved from the commission boxes and are present at the workbench. Pose estimation based on FoundationPose [32] complements the object detection by providing continuous 6D tracking of components, including partly occluded objects, under variable lighting conditions. FoundationPose requires an initial bounding box and a CAD model in OBJ format for each target object. To eliminate the need for a manual initialization, we use Any6D [33] in combination with FoundationPose, SAM2 segmentation [34] and InstantMesh mesh generation [35], allowing us to start from an anchor RGBD image instead of a CAD model.

Accurate pose estimates are a prerequisite for AR-based assembly guidance, where virtual overlays are registered to physical components in real time. Our AR interface works with tablets, smart glasses, and VR headsets.

In the targeted component commissioning scenario with multiple workstations, the same tracking pipeline can operate at each station independently, as the zero, few-shot and model-free approaches do not require station-specific training data.

As Fig. 4 shows, not only the worker movements (tracked by the MediaPipe Hands) but also the aforementioned components, AFOS and CTDS (Section 3.1), provide input from cameras and other sensors to our guidance system. To orchestrate the multiple AI models involved, we use the NVIDIA Triton Inference Server [36]. AFOS packages camera streams together with the static reference data including CAD files, initial bounding boxes and anchor images. CTDS receives this bundled input, recognizes objects and assembly states and eventually submits inference requests to the Triton server via gRPC. The server executes the models and returns results in the protobuf format [37, 38]. Triton enables concurrent model execution and dynamic batching, which improves throughput and efficiency.

4. BIM2Robot: Keeping AGVs Up-to-Date with the Factory Environment

BIM2Robot complements the Assembly Twin presented in Section 3. We developed this open-source framework independently of NVIDIA Omniverse. However, it proves particularly valuable in automated factory environments such as the shopfloor scenario which we described above to introduce our Assembly Twin.

4.1. Sideloading the Robot Workplace

While the Assembly Twin seamlessly integrates animated visualization with operating procedures, BIM2Robot separates the static environment in the form of a building model from these dynamic processes. BIM2Robot can generate navigation plans from building models, but has no awareness of why a reroute is needed. The Assembly Twin can detect production disruptions and manage workflows, but cannot autonomously translate a production event into updated robot navigation. This directly addresses the gap identified in Section 3.2.2: the Assembly Twin coordinates AGV destinations but cannot supply the underlying navigation plan. BIM2Robot fills this role by deriving executable routes from the building's IFC description, providing the spatial navigation layer that the Assembly Twin relies on but does not contain itself.

BIM2Robot takes IFC-formatted building description files, as they are commonly used in architecture, as input for a conversion pipeline that tokenizes the contained data and re-interprets the resulting token stream as a robot-compatible navigation plan that ROS-compliant AGVs can execute. When these AGVs are deployed to an automated factory, detailed workplace layout information is transferred or "sideloaded" into assembly scenarios like the one described in Section 3.

Unlike additional sensors or cameras, which merely produce more data or alternative views, BIM2Robot generates executable source code for robot tasks directly from the workplace description. This generated source code enables the rapid development of new AGV applications which can go beyond load balancing in an assembly process, such as the one described above. BIM2Robot includes its own GUI for IFC manipulation (shown in Fig. 5) and task authoring: users can interactively select relevant spaces in a factory and integrate robot tasks with the IFC file as mission entities, e.g., the origin and destination of a transportation task, in the form of annotations. With its GUI BIM2Robot supports a human-in-the-loop workflow for task specifications outside the standard manufacturing procedures. These robot tasks may include:

- **Facility inspection:** robots regularly scan technical rooms, record sensor values, and check conditions. Our GUI supports assigning inspection tasks to specific rooms and linking them to the mission;
- **Intralogistics and supply-chain operations:** robots move safely through warehouses and production halls, recognize doors, walls, and paths from the BIM model, and support order picking, material transport, empty-container return, automatic inventory scans and cleanup.

The second gap from Section 3.2.2 is addressed here as well: when the shopfloor is reconfigured, re-running the BIM2Robot pipeline on the updated IFC file produces a revised topological graph and a new mission plan that immediately reflects the new layout.

4.2. The BIM2Robot Translation Pipeline

The BIM2Robot framework is organized as a pipeline-based system that processes a mission-annotated IFC building model and derives multiple robot-compatible outputs. The architecture separates (i) task authoring within the IFC model, (ii) structured parsing and conversion, and (iii) the generation of deployable representations for robotic execution. Fig. 6 summarizes these components and data flow.

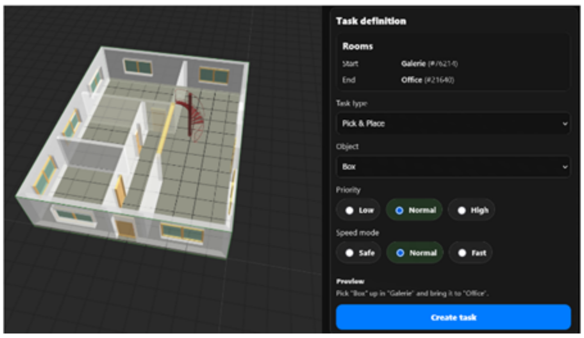

Fig. 5. The BIM2Robot GUI / IFC Editor.

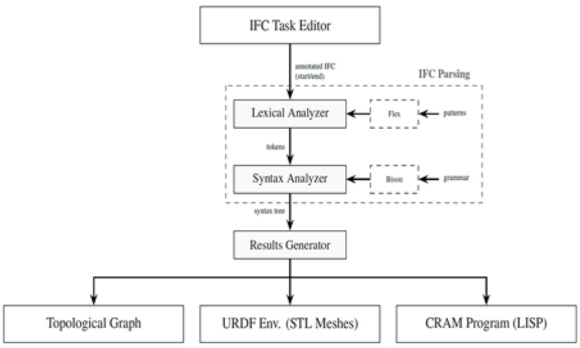

Fig. 6. The BIM2Robot IFC conversion pipeline.

The system workflow starts with the integration of robot tasks added by the users as annotations in the IFC building model. Using our GUI, users can open the IFC Task Editor as a context menu for any entity shown in a building, and assign task-related annotations such as start and target markers, task types, and execution parameters to process elements marked previously. These graphical editing steps result in an annotated IFC file that serves as the input for the subsequent processing steps.

The IFC data is a single source of truth, containing both the architectural building description and the robot-specific task definitions. No separate task description files or external mission specifications are required, as all task-relevant information is embedded in the BIM model.

The pipeline is organized as a classical parsing process consisting of lexical analysis, syntax analysis, and result generation. During this process, relevant IFC entities such as spaces, boundaries, and task annotations are identified, structured, and mapped into an internal representation that serves as a common basis for all subsequent outputs. The lexical and syntactic analysis stages are implemented using the GNU tools Flex and Bison[2] (as we have shown in a concept paper before [22]). Our design is inspired by compiler construction and allows the conversion pipeline to remain independent of specific robotic frameworks (i.e., it is forward compatible with future ROS versions) while ensuring that both geometric information and task-related annotations are consistently interpreted.

In the last processing step, three robot-compatible outputs are produced:

1. A topological graph of the robot workspace capturing rooms as nodes and doors or passages as edges. This graph represents the spatial connectivity of the environment and serves as a high-level navigation structure independent of metric planning;
2. A geometric environment model formatted as a URDF description with associated STL meshes. This representation enables the use of the building geometry in simulation and collision checking in physics-based environments or robot simulators;
3. A LISP program (with ROS library extensions), which encodes the mission logic derived from the task annotations in the form of an abstract syntax tree. This functional code comprises high-level instructions that can be executed using the Cognitive Robot Abstract Machine library (CRAM [39]) and the roslisp[3] interpreter for controlling the robot application.

By separating these outputs, the architecture allows each representation to evolve independently while remaining consistent through a shared source model.

4.3. Methodology

We now examine the BIM2Robot components comprising the data transformation pipeline [22].

4.3.1. Task Encoding

In the first step, robot task-related information, such as start and target locations, e.g. for filming, are added as semantic annotations, allowing the building model to serve as a unified source of structural and task data. Robot task specifications are thus defined at a high level of abstraction and independently of any specific robot platform or execution framework.

The interpretation of the task annotations and their transformation into robot-compatible representations are addressed in the subsequent processing steps.

4.3.2. Token Streaming and Parsing

During token streaming, the IFC file is processed sequentially by a lexical analyzer, which we implemented via GNU Flex[4].

The IFC analyzer (and the other BIM2Robot components) are available via github[5].

Relevant constructs are identified in the textual IFC representation and translated into a stream of symbolic tokens representing spatial entities, relationships, and task annotations. This step abstracts from the original IFC syntax and isolates information required for robotic navigation and task execution.

The token stream is then passed to a syntax analyzer implemented with Bison. Based on a predefined grammar, the tokens are combined into a structured intermediate representation that encodes containment relations, connectivity between spaces, and references to task-relevant locations. This representation preserves the logical structure of the environment while remaining independent of the IFC file format. By specifying a different grammar, users may also switch to a USD[6] building description, as used internally by Omniverse's visualization components. Thus, BIM2Robot can be used with Omniverse (as we show in Section 5) or independently.

4.3.3. Output Representations

The first output is a topological graph, such as the one shown in Fig. 7. Here, rooms are nodes and passable connections are edges. This graph captures the navigational structure of the building and serves as a high-level abstraction for route selection. Internally, the graph is stored as an adjacency matrix, but it can be stored in a comma-separated file and plotted using, e.g., GNUPlot.

A geometric environment model is derived in the form of a URDF description as the second output, including associated mesh files (see Fig. 8). This representation provides collision geometry and spatial context for simulation and execution, enabling the use of standard robotic tools for animated experiments with virtual robots in ROS-compliant simulation software.

---

[2] https://www.gnu.org/software/bison
[3] https://wiki.ros.org/roslisp
[4] https://westes.github.io/flex/manual
[5] github.com/TimMHoffmann/digital-building-models-to-cram
[6] https://openusd.org

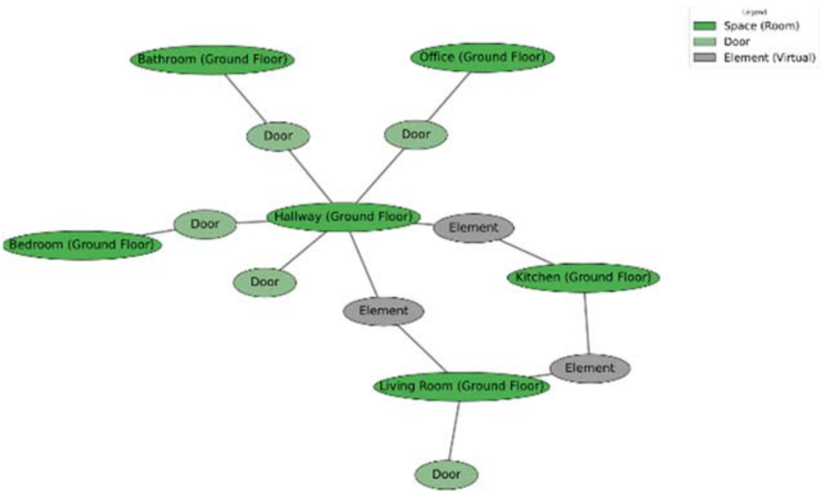

Fig. 7. Topology of the floor of the building from Fig. 5.

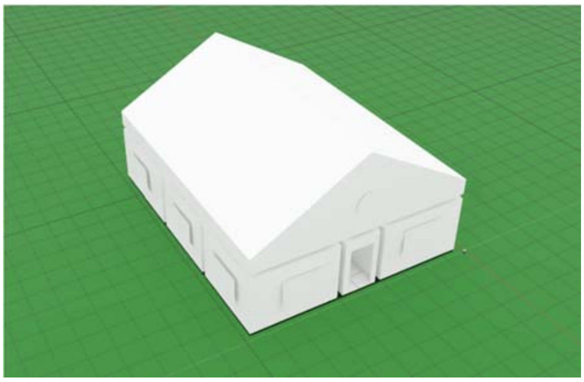

Fig. 8. URDF-based geometric environment model used.

The third output is functional code that encodes task logic derived from the annotated building model, in the form of an executable program for a ROS-compliant robot. Using the structural information from the topological graph and the geometric reference frame of the environment model, the CRAM layer synthesizes executable robot actions such as navigation between rooms or task-specific operations at defined locations.

5. Toward a Unified Framework: Integrating BIM-Based Navigation and Digital Twin-Driven Assembly

BIM2Robot excels at transforming standardized building descriptions into executable robot navigation plans, providing a semantically rich, geometry-aware model of the factory floor that can be easily updated whenever the physical environment changes by re-running the appropriate script. The Assembly Twin, on the other hand, delivers real-time awareness of the production process, monitoring workbench states, guiding workers through complex assembly tasks, and managing the dynamic rerouting of components in response to live production events.

5.1. Complementary Capabilities

These strengths are complementary. Where BIM2Robot understands space, the Assembly Twin understands the process. Both technologies keep humans in the loop: in the case of BIM2Robot, typically software developers, and in the Assembly Twin, typically factory workers. By combining both technologies, we gain what neither system offers alone: a closed loop between production intelligence and spatial navigation, a shared environment model that is simultaneously process-aware and geometrically precise, and the ability to autonomously adapt to both production disruptions and shopfloor layout changes without manual intervention.

5.2. Conceptual Framework Architecture

The proposed framework is structured around a shared data model in which workbenches, storage locations, AGVs, and assembly tasks are consistently referenced across both systems. Workbench identifiers used in the Assembly Twin must correspond directly to spatial entities annotated in the IFC model, as this alignment is the technical prerequisite that makes event-driven communication between the two layers possible. Both layers retain their own internal logic and interact exclusively through defined interfaces, requiring no centralized controller.

5.3. Scenario Walkthrough

To illustrate how the framework operates at runtime, consider the following scenario: a workbench goes offline unexpectedly due to a tool failure. The Assembly Twin detects the failure via AFOS and CTDS monitoring, identifies all components currently queued for the affected workbench, and issues an event message containing the workbench identifier and rerouting priority to BIM2Robot. BIM2Robot queries the topological graph, determines a viable alternative workbench, and returns an updated ROS-compatible mission plan. The affected AGVs are rerouted accordingly while the Assembly Twin updates the Omniverse visualization to reflect the new production state in real time.

6. Limits and Perspectives

The framework presented here lays the conceptual foundation for an event-driven integration of production intelligence and robot navigation, with practical implementation and experimental validation remaining as the next steps. Event communication requires that workbench identifiers are uniquely mapped to IFC entities. In practice, IFC models are not always kept up to date with the physical shopfloor state, and discrepancies between the building model and the actual layout would result in incorrect navigation plans without the system detecting the inconsistency. Ensuring continuous synchronization between the IFC model and the physical environment is therefore a central focus of the planned implementation work. The integration of dynamic obstacle detection into BIM-derived navigation plans is a natural extension for future work, as is the formalization of the criteria by which BIM2Robot selects an alternative workbench, such as shortest route, available capacity, or task priority. Once the framework is fully implemented, BIM2Robot scripts will no longer be called manually. A production event such as a workbench failure will then automatically trigger a complete navigation replanning and AGV rerouting.

7. Conclusion

This article proposes a conceptual framework that combines BIM2Robot and the Assembly Twin to establish a closed loop between production intelligence and robot navigation. Using an example scenario, we have illustrated how the combined framework enables autonomous adaptation to both unexpected production disruptions and continuous shopfloor layout changes. The reliance on open standards such as IFC, ROS, and OPC UA ensures interoperability and reduces dependence on proprietary infrastructure.

References

[1]. A. Arnouk, N. Behm, C. Borck, Architecture for digital twins in manual assembly within the industrial metaverse, in *Proceedings of the 6th IFSA Winter Conference on Automation, Robotics & Communications for Industry 4.0/5.0/6.0 (ARCI)*, 2026, pp. 5-12.

[2]. T. Hoffmann, F. Dietrich, M. Melzer, J. Dünnweber, A code generation framework for indoor robot applications based on building information modeling (BIM), in *Proceedings of the 6th IFSA Winter Conference on Automation, Robotics & Communications for Industry 4.0/5.0/6.0 (ARCI)*, 2026, pp. 40-44.

[3]. NVIDIA, Siemens and NVIDIA to enable industrial metaverse, 2022, https://nvidianews.nvidia.com/news/siemens-and-nvidia-to-enable-industrial-metaverse

[4]. OpenUSD, Introduction to USD – Universal Scene Description 26.03 documentation, https://openusd.org/release/intro.html

[5]. NVIDIA, NVIDIA announces Omniverse Cloud APIs to power wave of industrial digital twin software tools, 2024, https://nvidianews.nvidia.com/news/omniverse-cloud-apis-industrial-digital-twin

[6]. Dassault Systèmes, Virtual twin experiences for manufacturing industries, https://www.3ds.com/virtual-twin/manufacturing-industries

[7]. NVIDIA, NVIDIA Omniverse for physical AI, https://www.nvidia.com/en-us/omniverse/

[8]. G. Barbieri, A. Bertuzzi, A. Capriotti, L. Ragazzini, et al., A virtual commissioning based methodology to integrate digital twins into manufacturing systems, *Production Engineering Research and Development*, Vol. 15, Issue 3-4, 2021, pp. 397-412.

[9]. S. Gil, P. H. Mikkelsen, C. Gomes, P. G. Larsen, Survey on open-source digital twin frameworks – A case study approach, *Software: Practice and Experience*, Vol. 54, Issue 6, 2024, pp. 929-960.

[10]. R. Schmitt, C. Borck, M. Behm, J. Böhnke, Approach of an asset combination based on RAMI4.0 for the digital transformation and operation of a digital twin, *Procedia CIRP*, Vol. 130, 2024, pp. 724-729.

[11]. B. Wang, L. Zheng, Y. Wang, W. Fang, et al., Towards the Industry 5.0 frontier: Review and prospect of XR in product assembly, *Journal of Manufacturing Systems*, Vol. 74, 2024, pp. 777-811.

[12]. C. Chen, T. Wang, D. Li, J. Hong, Repetitive assembly action recognition based on object detection and pose estimation, *Journal of Manufacturing Systems*, Vol. 55, 2020, pp. 325-333.

[13]. G. Fragapane, R. De Koster, F. Sgarbossa, J. O. Strandhagen, Planning and control of autonomous mobile robots for intralogistics: Literature review and research agenda, *European Journal of Operational Research*, Vol. 294, Issue 2, 2021, pp. 405-426.

[14]. Í. R. Da Costa Barros, T. P. Nascimento, Robotic mobile fulfillment systems: A survey on recent developments and research opportunities, *Robotics and Autonomous Systems*, Vol. 137, 2021, 103729.

[15]. M. S. Moura, C. Rizzo, D. Serrano, BIM-based localization and mapping for mobile robots in construction, in *Proceedings of the IEEE International Conference on Autonomous Robot Systems and Competitions (ICARSC)*, 2021, pp. 12-18.

[16]. K. Kim, M. Peavy, BIM-based semantic building world modeling for robot task planning and execution in built environments, *Automation in Construction*, Vol. 138, 2022, 104247.

[17]. R. G. Braga, M. O. Tahir, S. Karimi, U. Dah-Achinanon, et al., Intuitive BIM-aided robotic navigation and assets localization with semantic user interfaces, *Frontiers in Robotics and AI*, Vol. 12, 2025, 1548684.

[18]. X. Zhao, C. C. Cheah, BIM-based indoor mobile robot initialization for construction automation using object detection, *Automation in Construction*, Vol. 146, 2023, 104647.

[19]. F. Bahreini, M. Nasrollahi, A. Taher, A. Hammad, Ontology for BIM-based robotic navigation and inspection tasks, *Buildings*, Vol. 14, Issue 8, 2024, 2274.

[20]. M. Kümpel, J. Dech, Semantic digital twins for omni-channel localisation, *IFAC-PapersOnLine*, Vol. 59, Issue 10, 2025, pp. 613-618.

[21]. S. Ebert, J. Mey, R. Schöne, S. Götz, et al., Distributed Petri nets for model-driven verifiable robotic applications in ROS, *Innovations in Systems and Software Engineering*, Vol. 20, Issue 4, 2024, pp. 531-557.

[22]. T. Hoffmann, M. Melzer, J. Dünnweber, Telling robots to do what we want them to, in *Proceedings of the IEEE International Conference on Control, Mechatronics and Automation (ICCMA)*, 2025, pp. 69-75.

[23]. NVIDIA GTC 2024: AI and robotics innovations overview, 2024, https://www.researchgate.net/publication/386442028_NVIDIA_GTC_2024_AI_AND_ROBOTICS_INNOVATIONS_OVERVIEW

[24]. Nucleus overview – Omniverse Nucleus, https://docs.omniverse.nvidia.com/nucleus/latest/index.html

[25]. Introduction – Omniverse Developer overview, https://docs.omniverse.nvidia.com/dev-overview/latest/index.html

[26]. USD connections overview – Omniverse Connect, https://docs.omniverse.nvidia.com/connect/latest/index.html

[27]. Revit – Omniverse Connect, https://docs.omniverse.nvidia.com/connect/latest/revit.html

[28]. NVIDIA Omniverse, kit-app-template, https://github.com/NVIDIA-Omniverse/kit-app-template

[29]. Overview – Omniverse Kit, https://docs.omniverse.nvidia.com/kit/docs/kit-manual/latest/guide/kit_overview.html

[30]. API (python) – Omniverse Kit, https://docs.omniverse.nvidia.com/kit/docs/kit-manual/109.0.3/API.html

[31]. F. Zhang, V. Bazarevsky, A. Vakunov, A. Tkachenka, et al., MediaPipe Hands: On-device real-time hand tracking, *arXiv*, 2020, arXiv:2006.10214.

[32]. B. Wen, W. Yang, J. Kautz, S. Birchfield, FoundationPose: Unified 6D pose estimation and tracking of novel objects, in *Proceedings of the IEEE/CVF Conference on Computer Vision and Pattern Recognition (CVPR)*, 2024, pp. 17868-17879.

[33]. T. Lee, B. Wen, M. Kang, G. Kang, et al., Any6D: Model-free 6D pose estimation of novel objects, arXiv, 2025, arXiv:2503.18673.

[34]. N. Ravi, V. Gabeur, Y.-T. Hu, R. Hu, et al., SAM 2: Segment anything in images and videos, *arXiv*, 2024, arXiv:2408.00714.

[35]. J. Xu, W. Cheng, Y. Gao, X. Wang, et al., InstantMesh: Efficient 3D mesh generation from a single image with sparse-view large reconstruction models, *arXiv*, 2024, arXiv:2404.07191.

[36]. Triton inference server: An optimized cloud and edge inferencing solution, https://github.com/triton-inference-server/server

[37]. Triton Inference Server, Inference protocols, https://github.com/triton-inference-server/server/blob/main/docs/customization_guide/inference_protocols.md

[38]. Triton Inference Server, Client source code, https://github.com/triton-inference-server/client/tree/main/src

[39]. L. Mösenlechner, M. Beetz, M. Tenorth, CRAM – A cognitive robot abstract machine for everyday manipulation in human environments, in *Proceedings of the IEEE/RSJ International Conference on Intelligent Robots and Systems (IROS)*, 2010, pp. 1012-1017.

Published by International Frequency Sensor Association (IFSA) Publishing, S. L., 2026 (http://www.sensorsportal.com).

Advances in Robotics and Automatic Control: Reviews

Sergey Y. Yurish, Editor

Industrial robots offer many benefits, including cost reduction, increased rate of operation and improving quality, along with improved manufacturing efficiency and flexibility. The demand for industrial robotics is majorly observed in industries such as automotive, electrical & electronics, chemical, rubber & plastics, machinery, metals, food & beverages, precision & optics, and others. In its turn, industrial automation control market will witness considerable growth during the same period with the growing demand of products such as sensors, drives and various robots.

The first volume of the 'Advances in Robotics and Automatic Control: Reviews', Book Series started by IFSA Publishing in 2018 contains ten chapters written by 32 contributors from 9 countries: Belgium, China, Germany, India, Ireland, Japan, Serbia, Tunisia and USA.

This book will be a valuable tool for those who involved in research and development of various robots and automatic control systems.

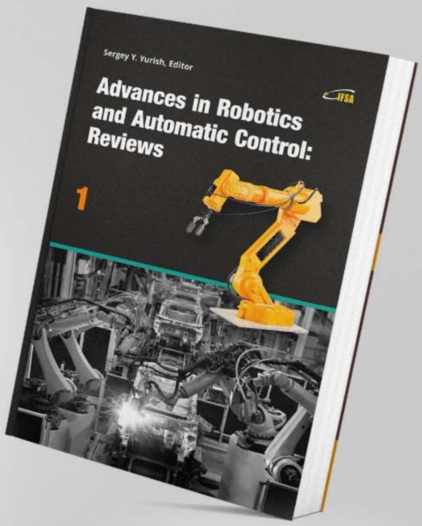

IFSA Publishing

Sensors & Transducers, Vol. 273, Issue 2, June 2026, pp. 50-61

Sensors & Transducers
Published by IFSA Publishing, S. L., 2026
http://www.sensorsportal.com

A Multi-Objective LQR-Based Motion Cueing Framework for Redundant Ski Simulators with Human Perception Integration

[1, *] Taha HOUDA, [2] Lotfi BEJI and Ali AMOURI
[1] Computer Engineering department, Prince Mohammad Bin Fahd University, Alkhobar, Saudi Arabia
[2] ISAT Nevers, Université de Bourgogne (UBE), France
[3] IBISC Laboratory, University of Paris-Saclay, Évry-Courcouronnes, France
Tel.: + 966 506468532
E-mail: thouda@pmu.edu.sa, lotfi.beji@u-bourgogne.fr, ali.amouri@univ-evry.fr

Received: 31 March 2026 /Revised: 4 May 2026 /Accepted: 20 May 2026 /Published:29 June 2026

Abstract: To facilitate the integration of people with disabilities into sports domains using simulators, particularly in the field of skiing, this article proposes a solution to the Motion Cueing Algorithm (MCA) parameter optimization problem under some human-platform interactions and environment constraints, distinguished here as a multi-objective problem. The considered simulator is redundant with respect to skier's motions and to generate high-fidelity movements, the Linear-Quadratic Regulator (LQR) method is employed to minimize the human perceptual error between the real and simulated skier environments. Both the vestibular model and the redundant simulator constraints are considered in MCA parameter optimization. Linear time-invariant representations are detailed and the appropriate optimal control parameters are solved. The implemented skier scenarios demonstrate the improvement in human sensation and the efficiency of the proposed redundancy resolution method.

Keywords: Optimal control, Human sensation, Hybrid robot, Motion cueing algorithm, Redundancy resolution.

1. Introduction

3D interactions in mixed reality environments and their integration into industry have recently experienced significant growth [1, 2]. A crucial question for the design and validation of a modern simulator is how to combine mechanical systems and virtual tools [3]. The best-known examples are driving simulators [4] and flight simulators [5], which have contributed much knowledge to the automotive and aerospace industries. They can help study the effects of implementing active safety technologies and driver assistance, and explore human factors such as driver response to road conditions and aging [6].

Handiskiing [7, 8], which combines the words Disability and Alpine Skiing, refers to the adaptation of alpine skiing to people with disabilities. It is a new sport that has attracted a lot of interest from enthusiasts who enjoy practicing it every year. However, there are many constraints on ski training, especially for people with disabilities. There are environmental dependencies, as skiing requires a good amount of snow and slopes, which limits the sport to adapted resorts. For this reason, ski simulators are becoming increasingly popular in the ski sports industry due to their ability to replicate real snow conditions and provide users with an immersive experience. They use advanced technologies to reproduce sliding movements, gravity and snow vibrations, such as Motion Cueing Algorithm (MCA) [9, 10]. Ski simulators can also be coupled with virtual reality to increase immersion and human sensation. A motion simulator proves to be an effective tool that allows training of people with various joint diseases while maintaining a clinical safety environment [11]. In addition, these simulators provide psychological, muscular and social benefits for people with severe disabilities [12]. A Motion-Cueing Algorithm (MCA), also known as a washout filter algorithm, is the strategy that controls how motion cues are generated while keeping the motion of the platform within its physical limits [10]. The main goal is to provide realistic motion cues to the pilot or seated skier in the simulator while keeping the motion platform within its physical limits.

In [13, 14], several washout algorithms have been proposed. Many researchers have modified and improved these algorithms in recent years [15, 16]. They can mainly be divided into classical, adaptive and optimal cueing algorithms. The classical approach consists of defining fixed coefficients in the worst-case maneuvers, which degrades the quality of motion perception in moderate maneuvers. Moreover, it can generate wrong cues due to the filter characteristics and lead to wrong motion signals. The main drawback of the classical washout filter is that it does not take human perception into account. The adaptive approach was implemented by Reid and Nahon [17]. It eliminates this shortcoming by adaptively modifying the coefficients and providing better motion sensation. Several motion cueing approaches have been proposed in recent years. Qazani et al. [18] introduced a fuzzy logic-based adaptive motion cueing algorithm to improve simulator performance under varying operating conditions. However, such approaches are mainly heuristic and do not explicitly incorporate a detailed mathematical model of human motion perception. Nahavandi [19] emphasized the importance of human-centric design in modern engineering systems, highlighting the need to integrate human perception into control strategies. In this direction, Gharib et al. [20] proposed an evolutionary optimal washout filter based on a genetic algorithm, aiming to optimize motion cueing performance through advanced optimization techniques. This optimal washout filter algorithm was based on human motion perception and considered a mathematical model of the human vestibular system [21].

The optimal algorithm, which uses LQR-based control techniques, attempts to provide higher-order filters prior to real-time application to minimize the error of motion sensing rather than motion states while maintaining the physical limits of the simulator. To the best of our knowledge, all existing ski simulators use only a 2-DoF mechatronic system, which is not sufficient to reproduce all the skier's movements. In general, most simulation platforms use only one hexapod platform. As a result, fewer research studies have addressed MCA for hybrid platforms. A so-called XY table is a significant improvement over the conventional simulators, which are able to perform larger translational motion in the longitudinal and transverse directions. The hexapod (6-DoF) is mounted above a table (2-DoF), giving a total of eight degrees-of-freedom (8-DoF). Thus, the human operator is exposed to both motions. Therefore, we propose a VR based high degree-of-freedom indoor ski training system, an 8-DoF simulator. Using this training system, we replay the movement of an expert skier recorded on a virtual slope and can reproduce this movement in the simulator as closely as possible [22].

In recent years, an increasing number of kinematically redundant robots have been used in various fields of robotics [23, 24]. This may be due to the focus on increasingly constrained environments where the conventional six degrees of freedom (6-DOF) may prove insufficient for obstacle avoidance and singularity [25, 26]. Kinematic redundancy occurs when a manipulator has more degrees of freedom than are required to perform a particular task. Thus, it is widely recognized that a seven-joint robotic arm following an end-effector motion trajectory requiring six degrees of freedom is generally considered an example of an inherently redundant manipulator. This means that a particular position and orientation of the end effector determines an entire solution space, rather than a single solution. To obtain a particular configuration (or joint velocities/moments), a redundancy resolution method should select the element with the "best fit" in the solution space. The simplest method uses the pseudo-inverse of the Jacobian matrix. This guarantees a least-squares reconstruction of the desired end-effector velocity. A drawback of this method is that singularity avoidance cannot be guaranteed despite local minimization of joint velocities [27].

This journal article extends our previous conference work [28] with several significant contributions. First, a complete and explicit state-space formulation of the human vestibular system is provided, including both otolith and semicircular canal dynamics, whereas the conference version presented a more limited formulation. Second, a simplified and computationally efficient linear time-invariant (LTI) representation is introduced to facilitate real-time implementation of the motion cueing algorithm. Third, perceptual thresholds of the human vestibular system are explicitly incorporated into the MCA design, improving the realism of the generated motion cues. Fourth, the LQR-based formulation is extended with a fully specified cost function, explicit weighting matrices, and a reproducible numerical setup. Fifth, the redundancy resolution strategy is further developed and formalized, including a clear algorithmic implementation for motion distribution between the hexapod and the XY table. Finally, a quantitative performance evaluation is introduced through a well-defined performance indicator (PI), allowing comparison with classical, adaptive, and optimization-based approaches. These extensions significantly enhance the rigor, reproducibility, and practical applicability of the proposed method compared to the conference version.

In this article, we describe the model of human motion perception in Section 2. Then, in Section 3, we explain the optimal MCA control based on the LQR theory. In Section 4, we develop a redundancy solution method that makes the simulator nonredundant with respect to the task by finding the appropriate motion distribution of the XY table and the hexapod. Finally, in Section 5, we draw a conclusion and give an outlook of the work.

2. Human Motion Perception System

The vestibular system illustrated in Fig. 1 is a set of organs located in the inner ear and responsible for detecting inertial movements, whether translation or rotation. There are two subsystems: the otolith organs and the semicircular canals, responsible for the detection of translation and rotation, respectively. A certain threshold of detection must be crossed to feel a movement.

According to [29], the specific stimulus of the otolith organs is the shear force between the two layers of the otolith membrane. The deformation of the gelatinous layer will induce the bending of the hair cells. The operation that transforms the biomechanical signal (bending of the hair cells) into nervous impulses (electrical activity of the hair cells) is the transduction mechanism [30]. When the hair cells tilt towards the kinocil, this causes depolarization. The frequency of the action potentials (nerve impulses noted Ni and measured in ips: impulse per second) is sent to the brain. When the hair cells tilt in the opposite direction, the sensory cells are hyperpolarized and the production of action potentials decreases. The variations in polarization (excitation and inhibition) lead to a variation in the frequencies of the action potentials of the afferent fibers.

Each semi-circular canal has a swollen base (bulb) that contains sensory cells and a cup (elastic gelatinous membrane denser than the endolymph). The bulbs also have a receptor area (sensory epithelium) called the ampullary ridge, similar to the macula of otoliths. As with otoliths, this area is involved in the transformation of the rotational movement of the head into a neuronal signal. The cupula is a gelatinous membrane, attached to the base of the ampullary ridge and the top of the bulb. The crista ampullaris or crista ampullaris (thick, rounded area) contains the hair cells responsible for neural transmission. When a rotational movement of the head occurs in the plane of one of the canals, the endolymph undergoes an inertial force with respect to the labyrinth and deforms the cupula. This deformation of the cup causes the hair cells to bend in the direction opposite to the movement (inertia). The fluid then continues to rotate in the canal at the same rate as the rotation. However, when the rotation continues at constant speed, the cup returns to its equilibrium position (non-linear phenomenon of saturation in neutral position and energy accumulation). Then, at the end of the rotation, the endolymph-cup system reacts in the opposite direction (energy discharge) of the one of the rotations which was completed. Finally, the cup returns to its initial position.

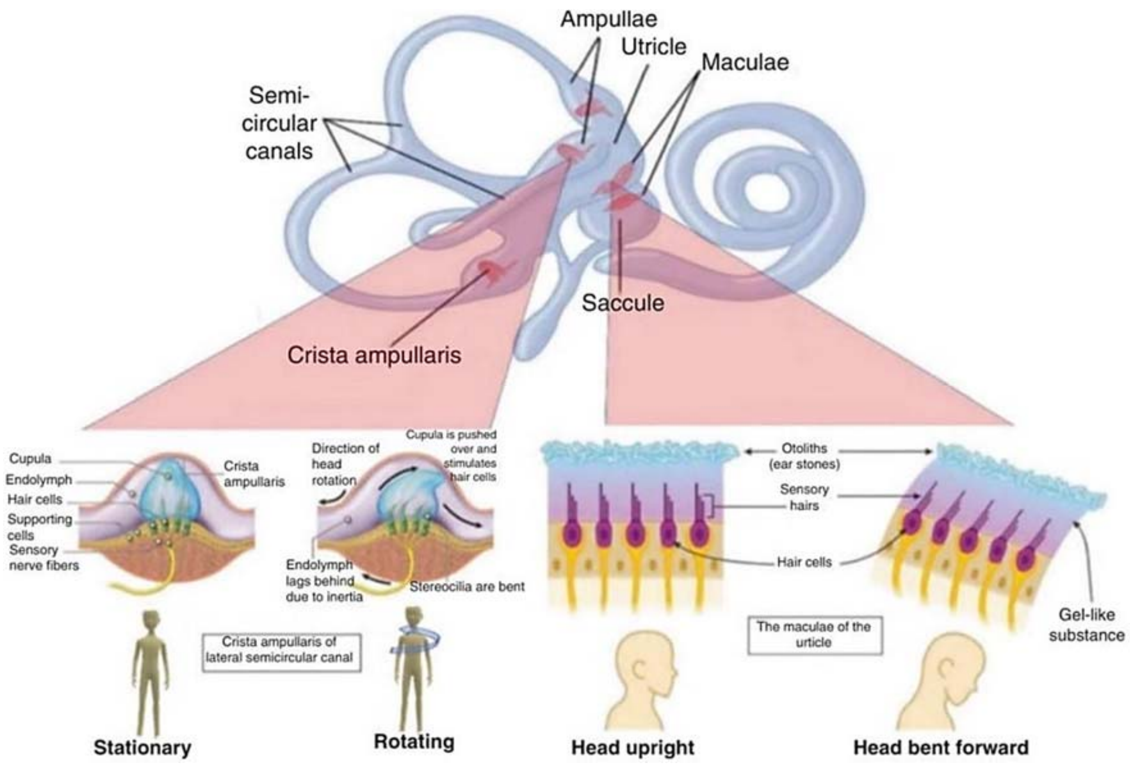

Fig. 1. Motion transduction, Rest vs otoliths (a) and semicircular canals (b) subjected to linear and rotational motion, respectively [29].

The proposed MCA must consider the human sensation model. The development of a mathematical model of the vestibular system is therefore crucial.

In the literature, the otolithic subsystem dynamics are modeled as a mass-spring-damper absorber [31] and [32]. This dynamic is modeled by the following second-order filter:

$$\frac{\hat{F}(s)}{F(s)} = K_{oto}\frac{\tau_L s + 1}{(1+\tau_1 s)(1+\tau_2 s)}, \quad (1)$$

where τ_1, τ_2 , and τ_L are long time, short time, and lead term constants, respectively, and s is the Laplace operator. $\hat{F}$ is the felt specific force and F is the stimulating specific force at the head level. Recall that the specific force is the difference between the linear acceleration and the gravity vector since, at rest, the otolithic organs undergo vertical gravity acceleration.

However, the dynamics of the semicircular canal subsystem are modeled as an overdamped pendulum [33–35]. This dynamic can be modeled by the following second-order low-pass filter:

$$\frac{\hat{\Omega}(s)}{\Omega(s)} = K_{scc}\frac{\tau_1\tau_a s^2(1+\tau_L s)}{(1+\tau_a s)(1+\tau_1 s)(1+\tau_2 s)}, \quad (2)$$

where $\hat{\Omega}$ is the felt angular velocity, Ω is the head angular velocity and τ_1, τ_2 , τ_L and τ_a are long time, short time, lead term, and adaptation operator constants, respectively. In the context of motion restitution using a motion simulator, there are three modes. The first mode is the longitudinal mode, also called surge/pitch mode which consists of a translation along the x-axis and a rotation θ_y around the y-axis. The second mode is the transverse mode where the translation is along the y-axis and the rotation θ_x is around x-axis and finally the third mode is the vertical mode which consists only of a translation along the z-axis. These modes are decoupled at the level of human sensations and, consequently, at the level of the vestibular system [28]. Therefore, the development of each mode occurs separately and in a similar way. Therefore, in this article, we present and develop below the algorithm of the longitudinal mode only (x, θ_y).

We develop the state space representation of the vestibular system constituting the otolith subsystem and the semicircular canal subsystems. The otolith's dynamic (1) in the longitudinal mode can be rewritten as:

$$\frac{\hat{F}_x(s)}{F_x(s)} = \overline{K}_{oto}\frac{(s+\frac{1}{\tau_L})}{(s+\frac{1}{\tau_1})(s+\frac{1}{\tau_2})}, \quad (3)$$

where $\underline{K}_{oto} = K_{oto}\frac{\tau_L}{\tau_1\,\tau_2}$ is defined as the static sensitivity.

Let us define the input as:

$$U(s) = \left(U_1(s)U_2(s)\right)^T\left(s\Theta y(s)s^2X(s)\right)^T,$$

where $(\quad)^T$ denotes the transpose. The specific force in the longitudinal mode is expressed by

$$F_x(s) = s^2X(s) + g\Theta y(s)$$

Therefore, $F_x(s) = U_2(s) + \left(g\frac{1}{s}\right)U_1(s)$.

Substituting $F_x(s)$ into (3) and introduce the Laplace inverse transformation leads to:

$$\begin{aligned}\ddot{\hat{f}}_x + \left(\frac{\tau_1+\tau_2}{\tau_1\tau_2}\right)\dot{\hat{f}}_x + \frac{\hat{f}_x}{\tau_1\tau_2} &= \\ = \overline{K}_{oto}\left(gu_1 + \frac{g}{\tau_L}\int u_1 dt + \dot{u}_2 + \frac{u_2}{\tau_L}\right),\end{aligned} \quad (4)$$

where $f_x(t) = u_2(t) + g\int u_1(t)\,dt$ and $u(t) = \left(\dot{\theta}_y(t)\ddot{x}(t)\right)^T$.

We retain the model of the head movement (u_1, u_2) and the human sensation at the otolith level:

$$\begin{aligned}\ddot{\hat{f}}_x + \lambda_1\dot{\hat{f}}_x + \lambda_2\hat{f}_x = \lambda_3\dot{u}_1 + \lambda_4 u_1 + \\ +\lambda_5\int u_1 dt + \lambda_6\dot{u}_2 + \lambda_7 u_2),\end{aligned} \quad (5)$$

(Sensation dynamics = Input dynamics),

where

$$\begin{aligned}\lambda_1 = \frac{\tau_1+\tau_2}{\tau_1\tau_2}, \lambda_2 = \frac{1}{\tau_1\tau_2},\\ \lambda_3 = 0, \lambda_4 = \overline{K}_{oto}\,g,\\ \lambda_5 = \overline{K}_{oto}\frac{g}{\tau_L}, \lambda_6 = \overline{K}_{oto}, \lambda_7 = \frac{\overline{K}_{oto}}{\tau_L}\end{aligned} \quad (6)$$

Let us consider the state vector $x_{oto} = (x_{oto1}x_{oto2}x_{oto3})^T$ as follows:

$$\begin{aligned}x_{oto1} &= \hat{f}_x\,,\\ x_{oto2} &= \dot{x}_{oto1} - \lambda_3 u_1 - \lambda_6 u_2,\\ x_{oto3} &= \lambda_5\int u_1 dt\end{aligned} \quad (7)$$

By taking the derivative state $\dot{x}_{oto1}$, we get the following LTI (Linear Time Invariant) model:

$$\begin{aligned}\dot{x}_{oto} &= A_{oto}\,x_{oto} + B_{oto}\,u,\\ y_{oto} &= C_{oto}\,x_{oto} + D_{oto}\,u\end{aligned} \quad (8)$$

where $x_{oto}\,\epsilon\,\mathbb{R}^3$, $y_{oto}\,\epsilon\,\mathbb{R}$ and $u = (u_1u_2)^T\,\epsilon\,\mathbb{R}^2$, are the otoliths states, output and the vestibular system input, respectively. The constant matrices are given as:

$$\begin{aligned}A_{oto} &= \begin{pmatrix}0 & 1 & 0\\ -\lambda_2 & -\lambda_1 & 1\\ 0 & 0 & 0\end{pmatrix}; C_{oto} = (1 \quad 0 \quad 0),\\ B_{oto} &= \begin{pmatrix}\lambda_3 & \lambda_6\\ \lambda_4-\lambda_1\lambda_3 & \lambda_7-\lambda_1\lambda_6\\ \lambda_5 & 0\end{pmatrix}; D_{oto} = (0 \quad 0)\end{aligned} \quad (9)$$

The semicircular subsystem dynamic (2) can be rewritten as:

$$\frac{\hat{\Omega}(s)}{\Omega(s)} = \frac{\beta_4 s^3+\beta_3 s^2}{s^3+\beta_2 s^2+\beta_1 s+\beta_0}, \quad (10)$$

where

$$\beta_0 = \frac{1}{\tau_a\tau_1\tau_2},\ \beta_1 = \frac{\tau_a+\tau_1+\tau_2}{\tau_a\tau_1\tau_2},$$
$$\beta_2 = \frac{\tau_1\tau_2 + \tau_a(\tau_1+\tau_2)}{\tau_a\tau_1\tau_2},\ \beta_3 = \frac{K_s cc}{\tau_2}, \quad (11)$$
$$\beta_4 = \frac{K_{scc}\tau_L}{\tau_2}$$

Let us take the semicircular states $x_{scc} = (x_{scc1}\ x_{scc2}\ x_{scc3})^T \in \mathbb{R}^3$ follows:

$$\begin{aligned} x_{scc1} &= \widehat{\omega}, \\ x_{scc2} &= \dot{x_{scc1}} + \beta_2 x_{scc1} - (\beta_3 - \beta_2\beta_4)u_1, \\ x_{scc3} &= \dot{x_{scc2}} + \beta_1 \dot{x_{scc1}} + \beta_1\beta_4 u_1 \end{aligned} \quad (12)$$

By taking the derivative state $\dot{x_{scc}}$, we can get the following semicircular model in LTI form as:

$$\begin{aligned} \dot{x_{scc}} &= A_{scc}x_{scc} + B_{scc}u, \\ y_{scc} &= C_{scc}x_{scc} + D_{scc}u \end{aligned} \quad (13)$$

where $y_{scc} = \widehat{\omega_{scc}}$ the felt rotation speed and its canonical observer matrices are:

$$\begin{aligned} A_{scc} &= \begin{pmatrix} -\beta_2 & 1 & 0 \\ -\beta_1 & 0 & 1 \\ -\beta_0 & 0 & 0 \end{pmatrix}; C_{scc} = (1 \quad 0 \quad 0), \\ B_{scc} &= \begin{pmatrix} \beta_3 - \beta_2\beta_4 & 0 \\ -\beta_1\beta_4 & 0 \\ -\beta_0\beta_4 & 0 \end{pmatrix}; D_{scc} = (\beta_4 \quad 0) \end{aligned} \quad (14)$$

The state space representation of the human vestibular system (v), which consists of both semicircular model and otolith subsystems, can be presented as follows:

$$\begin{aligned} \dot{x_v} &= A_v x_v + B_v u, \\ y_v &= C_v x_v + D_v u, \end{aligned} \quad (15)$$

where $x_v = (x_{scc}\ x_{oto})^T \in \mathbb{R}^6$contains the vestibular states, $y_v = (y_{scc}\ y_{oto})^T \in \mathbb{R}^2$ is the felt output representation, and $A_v \in \mathbb{R}^{6\times6}$, $B_v \in \mathbb{R}^{6\times2}$, $C_v \in \mathbb{R}^{2\times6}$, and $D_v \in \mathbb{R}^{2\times2}$ are:

$$\begin{aligned} A_v &= \begin{pmatrix} A_{scc} & 0_{(3\times3)} \\ 0_{(3\times3)} & A_{oto} \end{pmatrix}, \\ C_v &= \begin{pmatrix} C_{scc} & 0_{(3\times3)} \\ 0_{(3\times3)} & C_{oto} \end{pmatrix}, \\ B_v &= \begin{pmatrix} B_{scc} \\ B_{oto} \end{pmatrix}; D_v = \begin{pmatrix} D_{scc} \\ D_{oto} \end{pmatrix} \end{aligned} \quad (16)$$

The mathematical modeling of the vestibular system is illustrated in Fig. 2, which presents the conventional representation combining both the otolith and semicircular canal dynamics. This model reflects the detailed physiological behavior of human motion perception and serves as the basis for motion cueing design.

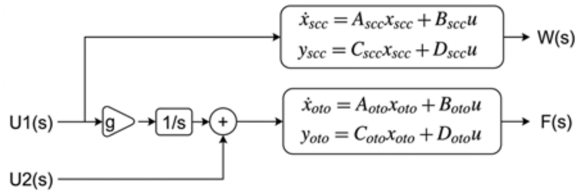

Fig. 2. The existing mathematical model of the vestibular system.

To facilitate the control design and integration within the optimal framework, a simplified state-space representation is proposed, as shown in Fig. 3. This representation reformulates the vestibular dynamics into a compact linear time-invariant (LTI) structure, enabling efficient implementation within the LQR-based optimization process. The proposed model preserves the essential perceptual dynamics while significantly reducing the computational complexity, making it suitable for real-time motion cueing applications.

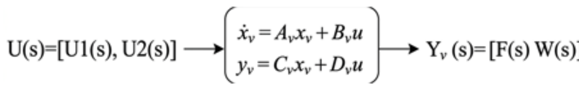

Fig. 3. The proposed simplified state space representation of the vestibular system.

The human vestibular system is characterized by perceptual thresholds below which motion stimuli are not consciously perceived. These thresholds play a crucial role in motion cueing design, as they define the limits within which discrepancies between real and simulated motion can remain imperceptible to the user. In particular, the otolith organs exhibit a detection threshold for linear acceleration typically in the range of 0.01 to 0.05 g (≈ 0.1–0.5 m/s²), while the semicircular canals have angular velocity detection thresholds on the order of 0.1 to 0.5 deg/s, with angular acceleration thresholds around 0.5 to 2 deg/s². When the generated motion signals remain below these thresholds, the human operator does not detect inconsistencies, allowing the simulator to operate within constrained physical limits while maintaining perceptual realism. Therefore, these thresholds are explicitly considered in the MCA design to ensure that the generated motion cues do not exceed human perception limits during washout and tilt coordination processes, thereby preserving motion fidelity and avoiding false or misleading sensations.

In addition to human perception constraints, the physical behavior of the motion platform must also be considered. The XY-6 DoF simulator is a nonlinear and coupled robotic system whose dynamics can be described using the standard rigid-body formulation:

$$\Gamma = M(q)\,\ddot{q} + H(q,\dot{q}),$$

where $\Gamma \in \mathbb{R}^8$ denotes the actuator torque vector, $q \in \mathbb{R}^8$ represents the generalized coordinates, $M(q)$ is the inertia matrix, and $H(q, \dot{q})$ includes Coriolis and gravitational effects. This model has been previously developed and validated in our earlier work [15]. The integration of both perceptual thresholds and system dynamics enables a unified framework for motion cueing optimization, which is presented in the following section.

3. MCA Multi-Objective Resolution

Simulator performance is measured by how well the following three objective functions are satisfied:

1. obj1: approximate the specific forces sensed by the human performing an application in the real world to the human performing the same application on a simulator;
2. obj2: respect the simulator's displacement, speed and acceleration limits;
3. obj3: do not exceed certain otoliths and semicircular canals thresholds in the washout and tilting operations.

Let us call the known human movement in real application the "predefined motion - pd" and the human movement on the simulator the "simulated motion - s". Thus, we can define the sensitive error $y_{v,e} \in \mathbb{R}^2$ as the difference in human perception between real $y_{v,pd}$ and simulated $y_{v,s}$ applications, and is expressed as follows:

$$y_{v,e} = y_{v,s} - y_{v,pd} \tag{17}$$

The vestibular state error is given $x_{v,e} = x_{v,s} - x_{v,pd}$. The sensitive error LTI model can be expressed as:

$$\begin{aligned} \dot{x_{v,e}} &= A_v x_{v,e} + B_v u_s - B_v u_{pd}, \\ y_{v,e} &= C_v x_{v,e} + D_v u_s - D_v u_{pd} \end{aligned} \tag{18}$$

This problem can be formulated as a classical optimal control problem which seeks to minimize a cost function containing the quadratic form of the sensitive error and the control inputs while limiting the simulator movement. This cost function J based on the LQR, over [t0 t1], can be specified as:

$$J = E\{\int_{t_0}^{t_1} (y_{v,e}^T Q y_{v,e} + \xi_d^T R_d \xi_d + \\ + u_s^T R u_s) dt\}, \tag{19}$$

where $y_{v,e}^T Q y_{v,e}$ denotes the perception error cost (perception validity), $\xi_d^T R_d \xi_d$ is the platform displacement cost, $u_s^T R u_s$ is the control input cost, E{} is the mean of the evaluation functions with respect to u_{pd} considered as filtered white noise as in [36], Q and R_d are positive semi definite matrices, and R is a positive definite matrix. To constrain the simulator motion, the $\xi_d^T R_d \xi_d$ part of the cost function must take the simulator's translational speed and displacement, and rotational speed. The principle of the MCA is to use the workspace efficiently and to bring the simulator back to its neutral position, for this we add the integral of the translational displacement. Therefore, we can define ξ_d as follows:

$$\begin{aligned} \xi_d &= \left(\iiint \ddot{x} dt^3 \iint \ddot{x} dt^2 \int \ddot{x} dt \theta_y\right)^T, \\ \dot{\xi_d} &= A_d \xi_d + B_d u_s, \end{aligned} \tag{20}$$

which are linked to the simulator input us through

$$A_d = \begin{pmatrix} 0 & 1 & 0 & 0 \\ 0 & 0 & 1 & 0 \\ 0 & 0 & 0 & 0 \\ 0 & 0 & 0 & 0 \end{pmatrix} \text{ and } B_d = \begin{pmatrix} 0 & 0 \\ 0 & 0 \\ 0 & 1 \\ 1 & 0 \end{pmatrix}$$

As recommended in [36], filtered white noise can be used as an input to the MCA in order to reproduce several scenario situations. This implies that an additional state space model needs to be incorporated to the one created earlier, whose states are the input. The predefined input upd can be considered as filtered white noises, and can be stated as follows:

$$\dot{x_n} = A_n x_n + B_n w, \tag{21}$$

where, x_n contains the filtered white noise states and w indicates white noise. A_n and B_n are given as:

$$A_n = \begin{pmatrix} -\gamma_1 & 0 \\ 0 & -\gamma_2 \end{pmatrix} \text{ and } B_n = \begin{pmatrix} \gamma_1 \\ \gamma_2 \end{pmatrix}, \tag{22}$$

where γ_1 and γ_2 are the cutoff frequencies.

The state space equations presented in (18), (20), and (21), can be combined to form the augmented state space equations and can be expressed as follows:

$$\begin{aligned} \dot{\chi} &= A\chi + Bu_s + Nw, \\ Y &= C\chi + Du_s, \end{aligned} \tag{23}$$

where $Y = (y_{v,e} \xi_d)^T$ is the desired output and $\chi = (x_{v,e} \xi_d x_n)^T \in \mathbb{R}^{12}$ contains the combined states. The combined system matrices $A \in \mathbb{R}^{12\times12}$, $B \in \mathbb{R}^{12\times2}$, $C \in \mathbb{R}^{6\times12}$, $D \in \mathbb{R}^{6\times2}$, and $N \in \mathbb{R}^{12\times1}$ are expressed as follows:

$$\begin{aligned} A &= \begin{pmatrix} A_v & 0_{(6\times4)} & -B_v \\ 0_{(4\times6)} & A_d & 0_{(4\times2)} \\ 0_{(2\times6)} & 0_{(2\times4)} & A_n \end{pmatrix}, \\ B &= \begin{pmatrix} B_v \\ B_d \\ 0_{(2\times2)} \end{pmatrix}, \\ C &= \begin{pmatrix} C_v & 0_{(4\times4)} & -D_v \\ 0_{(4\times6)} & I_4 & 0_{(4\times2)} \end{pmatrix}, \\ D &= \begin{pmatrix} D_v \\ 0_{(4\times2)} \end{pmatrix}, N = \begin{pmatrix} 0 \\ B_n \end{pmatrix}, \end{aligned} \tag{24}$$

with I_4 is the (4×4) identity matrix. In the design procedure of an optimal washout filter based on the LQR theory, several iterations are needed by changing the weighting matrices Q, R, and Rd for generating a suitable LQR-based optimal washout filter. The system equation and cost function can be transformed into the standard optimal control form, as follows:

$$\dot{\chi} = A_{tot}\chi + B u_{tot} + N w, \quad J_{tot} = E\{\int_{t_0}^{t_1}(\chi^T R_{tot1}\chi + u_{tot}^T R_{tot2} u_{tot})dt\}, \tag{25}$$

where $G = diag[Q, R_d]$, $R_{tot2} = R + D^T G D$, $R_1 = C^T G C$, $R_{12} = C^T G D, R_{tot1} = R_1 - R_{12} R_{tot2}^{-1} R_{12}^T$, $A_{tot} = A - B R_{tot2}^{-1} R_{12}^T$, $u_{tot} = u_s + R_{tot2}^{-1} R_{12}^T \chi$.

The cost function of (25) is minimized when

$$u_{tot} = -R_{tot}^{-1} B^T P \chi, \tag{26}$$

where P is the solution of the following algebraic Riccati equation:

$$R_{tot1} - P B R_{tot2}^{-1} B^T P + A_{tot}^T P + P A_{tot} = 0 \tag{27}$$

By specifying a matrix K, where $u_s = -K\chi$, we can get the following equation:

$$u_s = -(K_1\, K_2\, K_3)\begin{pmatrix} x_{v,e} \\ \xi_d \\ x_n \end{pmatrix}, \tag{28}$$

where $K = R_{tot2}^{-1}(B^T P + R_{12}^T)$ and $K_1 \in \mathbb{R}^{2\times 6}$, $K_2 \in \mathbb{R}^{2\times 4}$ $K_3 \in \mathbb{R}^{2\times 2}$. As $x_n = u_{pd}$, the states corresponding to x_n are eliminated. Thus, we get:

$$\begin{pmatrix} \dot{x}_{v,e} \\ \dot{\xi}_d \end{pmatrix} = \begin{pmatrix} A_v - B_v K_1 & -B_v K_2 \\ -B_d K_1 & A_d - B_d K_2 \end{pmatrix}\begin{pmatrix} x_{v,e} \\ \xi_d \end{pmatrix} + \begin{pmatrix} -B_v(I_2 + K_3) \\ -B_d K_3 \end{pmatrix} u_{pd}$$

After developing the state space form of (18) and (29), the optimal filter that connects the predefined input and the simulator input can then be expressed as:

$$u_s(s) = W(s) u_{pd}(s), \tag{29}$$

where

$$W(s) = (K_1 K_2)\Gamma(s)\begin{pmatrix} B_v(I_2 + K_3) \\ B_d K_3 \end{pmatrix} - K_3, \tag{30}$$

where $\Gamma(s) = \begin{pmatrix} sI - A_v + B_v K_1 & B_v K_2 \\ B_d K_1 & sI - A_d + B_d K_2 \end{pmatrix}^{-1}$, and $W(s) \in \mathbb{R}^{2\times 2}$ is a matrix of the optimized transfer function based on the LQR theory that links the simulator motion input. In this method, the structure of the filter is part of the optimization process unlike other approaches where the structure of the filter is completely predefined (classic approach) or partially defined (adaptive approach). In addition, the predefined trajectory is no longer a simple deterministic signal but a band of signals (filtered white noise), the optimization certainly becomes less precise but in return, we are left with a filter usable in real-time.

The weighting matrices used in the LQR design were selected through an iterative manual tuning process to balance motion fidelity, control effort, and physical constraints of the simulator.

The final matrices used in the simulations are:

$$Q = diag([80, 80, 80]),$$
$$R = diag([0.058, 0.058]),$$
$$R_d = diag([0.1, 0.1, 0.1])$$

The predefined input was modeled as filtered white noise with cutoff frequencies:

$$\gamma_1 = 10, \gamma_2 = 10$$

The simulations were performed over a duration of T = 60 s with zero initial conditions.

4. Application: Skier Motion in $\mathbb{R}^2$ Space

Within the IBISC laboratory we have fully designed and developed from scratch a motion simulator called XY-6 DoF and is shown in Fig. 4.

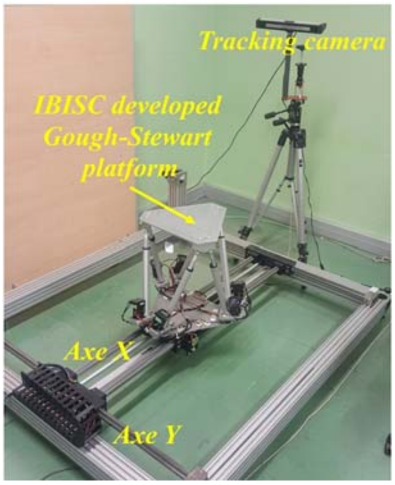

Fig. 4. XY-6 DoF simulator constructed at IBISC Laboratory.

The simulator consists of the well-known Gough-Stewart platform carried by two slider joints, X and Y, which form an XY-table, hence the name XY-6 DoF. To actuate the XY-6 DoF simulator we used the Nanotec PD4 servo motor due to its high performance and low weight. The translational movement of the sliders is obtained thanks to a mechanical rack wheel system. The translational movement of the hexapod legs is obtained thanks to the high-quality ball screw system, which transforms the rotational movement into translational movement.

In our work, we are interested in reproducing the ski scenario. The predefined scenario is defined and described in detail in the previous research work [15]. In order to find the simulator, input u_s using the optimal control, we need to introduce the simulator physical limits. We present in the following table the XY-6 DoF maximum of displacements, speeds and accelerations. In the following, we present the specific force restored by optimal approach in Fig. 5.

Table 1. XY-6 DoF motion interval.

D.o.F	Position	Max velocity	Max acceleration
X, Y	± 0.5 m	1.2 m/s	1.7 m/s²
X_p, Y_p, Z_p	± 0.1 m	0.8 m/s	1.1 m/s²
θ_x	± 15 deg	48.7 deg/s	71.6 deg/s²
θ_y	± 15 deg	48.7 deg/s	65.8 deg/s²
θ_z	± 15 deg	106 deg/s	154 deg/s²

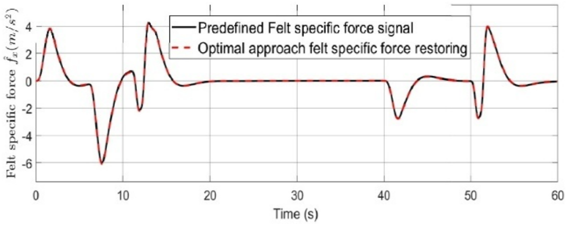

Fig. 5. Desired specific force from optimal algorithm.

The acceleration and specific force generated by the optimal filter show improved perceptual accuracy due to the coherence and proximity to the predefined trajectory. Fig. 6 shows the displacement, speed and acceleration of the hybrid simulator along the x-direction and Fig. 7 shows the tilt angle and tilt speed.

It is clear that the optimal approach can use the platform workspace more efficiently while respecting vestibular thresholds, can operate faster and be more precise compared to the classic and adaptive approach.

The simulator's displacement, speed, and acceleration resulting from the optimal approach have been determined according to the total capacity of the platform. Consequently, these movements exceed the capacity of either the table or the hexapod alone. A redundancy resolution must be developed to distribute the total simulator movement according to the capacity of each subsystem (hexapod and table).

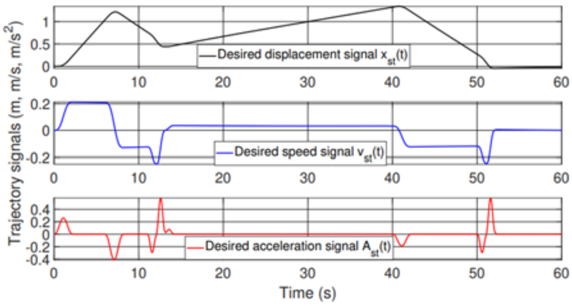

Fig. 6. Simulator trajectories along the x-direction.

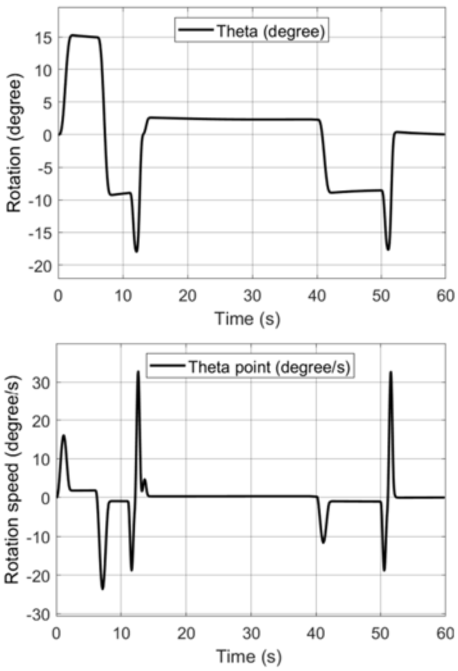

Fig. 7. Tilt angle and speed.

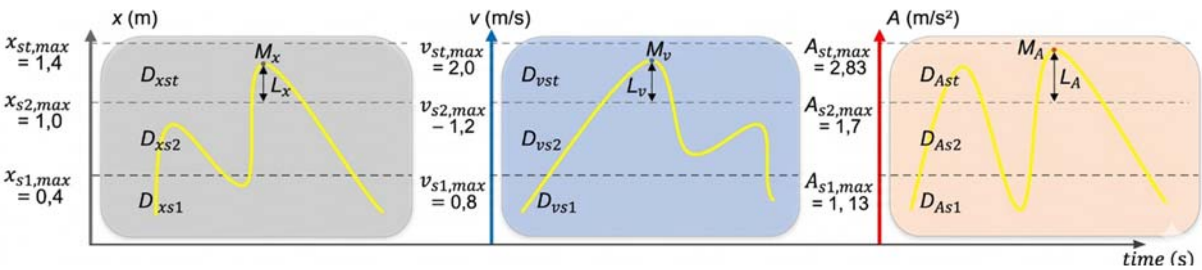

Fig. 8. Displacement, speed and acceleration workspaces.

First, we propose to use the hexapod mainly for tracking and performing the translation task once the XY table is inefficient. This means that the XY table will make the most significant translational move which is consistent with the purpose of introducing the XY table to the hexapod. Let us define $S1$ the first subsystem - hexapod, $S2$ the second subsystem – XY table and finally St the total system. Let us define the set $M = (M_x, M_v, M_a)$ where M_x, M_v, M_a denotes the maximum displacement, speed and acceleration of the predefined trajectory, respectively (obviously known for optimal approach). Fig 8 presents the displacement, speed and acceleration workspaces with its boundaries. The workspace boundaries are $x_{i,max}$, $v_{i,max}$, $A_{i,max}$ where $i = s1, s2, st$ for the first, the second subsystem and the total system. These boundaries are calculated from the real capacity of the platform motors using the direct kinematic model [24].

As described above, the most significant displacement will be mainly performed by the XY table. In the following, we present the proposed method to exploit the XY-6 DoF redundancy. First, if none of the M points M_x, M_v, M_A exceeds the capacity of the XY table, the XY table can perform the translational displacement alone. However, when one of the M points exceeds the capacity of the XY table, the hexapod must intervene and assist the XY table, as described below.

Let us take the case where one or more of the M points exceed the XY table capacity. Let us define L_x, L_v and L_A as the lack of displacement, speed and acceleration, respectively, that the XY table cannot perform. Moreover, let us define the dimensionless variables of L_x, L_v and L_A. Therefore

$$\begin{aligned} L_x &= M_x - x_{s2,max};\ L_{x_{dl}} = \frac{M_x - x_{s2,max}}{M_x} \\ L_v &= M_v - v_{s2,max};\ L_{v_{dl}} = \frac{M_v - v_{s2,max}}{M_v} \\ L_A &= M_A - A_{s2,max};\ L_{A_{dl}} = \frac{M_A - A_{s2,max}}{M_A} \end{aligned} \tag{31}$$

In addition to rotation movement, these translational trajectories lack should be performed by the hexapod. The total trajectory is designed by $x_{st}(t)$ which is equal to the trajectory performed by the XY table $x_{s2}(t)$ and the hexapod $x_{s1}(t)$. The two subsystems should perform the task in the same time conserving the same total desired trajectory, thus the trajectory of each subsystem can be composed as:

$$\begin{aligned} x_{s1}(t) &= \alpha x_{st}(t), \\ x_{s2}(t) &= (1-\alpha) x_{st}(t), \end{aligned} \tag{32}$$

where $\alpha \in$ R denotes the portion of the trajectory that should be performed by the hexapod, in other words the maximum lack of the XY table trajectory. Thus, α is the maximum of displacement, speed and acceleration lack.

$$\alpha = max(L_{x_{dl}}, L_{v_{dl}}, L_{A_{dl}}) \tag{33}$$

Since the hexapod model is non-linear thus the displacement, speed and acceleration capabilities are not similar. Therefore, we calculate the maximum displacement, speed and acceleration that can be performed by the hexapod by taking point M based on the 8-DoF simulator capacity. Therefore,

$$\begin{aligned} L_{x_{dl,max}} &= 28.5\ \%, \\ L_{v_{dl,max}} = 40\ \%, L_{A_{dl,max}} &= 40\ \% \end{aligned} \tag{34}$$

We can see that even if the hexapod has greater capacities in speed and acceleration than in displacement but it should still be limited by the displacement. Therefore α will be limited by the minimum of the maximum lack which is $L_{xdl,max}$. Thus

$$\alpha = min\left[max(L_{x_{dl}}, L_{v_{dl}}, L_{A_{dl}}), L_{x_{dl,max}}\right] \tag{35}$$

We summarize the proposed algorithm.

Algorithm 1. Redundancy Exploitation Algorithm

```
Initialization;
    Apply Optimal MCA;
Mx= max(xst(t));(Total desired displacement);
Mv= max(vst(t)); (Total desired speed);
MA=max(Ast(t));(Total desired acceleration);

X-Table Limits;
    xs2max = 1;  (Displacement limit);
    vs2max = 12; (Speed limit);
    As2max = 1.7;(Acceleration limit);

If((Mx>xs2max)OR(Mv>vs2max)OR(MA>As2max))
then
    Lx,dl=(Mx-xs2max)/Mx;(Displacement lack);
    Lv,dl=(Mv-vs2max)/Mv; (Speed lack);
    LA,dl=(MA-As2max)/MA;(Acceleration lack);

    Lm = max(Lx,dl, Lv,dl, LA,dl);  (Maximum
dimensionless lack);

    α = min(Lm, 0.285);
Else
    α = 0;
End If

Result;
    xs1(t) = α * xst(t);
    vs1(t) = α * vst(t);
    As1(t) = α * Ast(t);

    xs2(t) = (1 - α) * xst(t);
    vs2(t) = (1 - α) * vst(t);
    As2(t) = (1 - α) * Ast(t);
```

Let us apply the redundancy resolution to the trajectory result from the optimal MCA approach (Fig. 6). The maximum displacement, speed and acceleration are M: (M_x = 1.276 m, M_v = 0.313 m/s, M_A = 0.798 m/s^2). M_x is greater than the table displacement workspace which requires the use of the hexapod. Thus, we calculate the amount of the assistance provided by the hexapod L_x = 0.276 m, L_v = 0 m/s, L_A = 0 m/s^2. Consequently, compared to our constraints, for this specific task, the hexapod will carry $\alpha = L_{xdl}$ = 0.216 of the total trajectories which corresponds to 21.6 % and the X-table will carry the 78.4 %. Therefore, the total desired trajectories are clearly distinguished in hexapod and X-table trajectories shown in Fig. 9 and Fig. 10.

Fig. 9 and Fig. 10 show that the entire trajectory can be split into two trajectories achievable by each subsystem while maintaining the same human sensation. In summary, we have designed an optimal approach that considers human sensation via the vestibular system model and the physical limits of our platform XY-6 DoF. Using the optimal approach, we may deduce the upper platform behavior (at the human vestibular level) that corresponds to the total system trajectories. We therefore proposed the redundancy exploitation algorithm to generate the trajectories of each subsystem, hexapod and table, from the total trajectories.

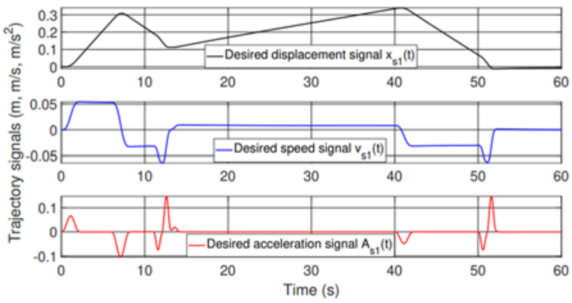

Fig. 9. Desired Hexapod trajectories.

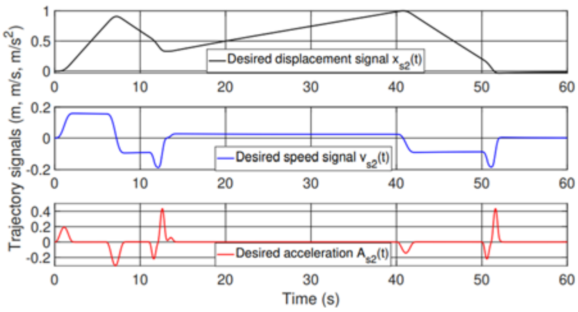

Fig. 10. Desired X-Table trajectories.

Motion fidelity can be defined as the degree to which the motion cues match those of the actual skier. Motion fidelity is affected by several factors, in particular the motion platform hardware and the MCA algorithm. Since motion tracking is subjective, motion fidelity is usually measured subjectively. Subjective assessment is performed using scales or questionnaires that pilots/skiers are asked to complete. Subjective assessment is the natural way to validate MCA and is fairly "easy" to perform. However, it has several drawbacks. First, there can be large differences between pilots/skiers, even with the same simulator and under the same conditions. In addition, the operator's responses may depend on the timing of the assessment, the particular sequence or order of the tests, the individual's personal preferences or even the nature of the assessment. In fact, the same person may provide different evaluations on different days, for the same simulator and under the same conditions. Therefore, subjective evaluation cannot provide repeatability nor reliability.

As our XY- 6 DoF platform is a prototype for the validation of algorithms and architecture and it is not possible to integrate a human being. To objectively evaluate the motion fidelity, we introduce a performance indicator (PI). This metric quantifies the similarity between the simulated motion cues and the predefined (reference) motion cues. This PI takes into account the scale of the generated movements with respect to the original scale (amplitude distortion) and the time-delay (phase distortion) produced by the motion platform's inertial nature and by the effects of frequency filtering.

$$PI = 100\left(1 - \frac{|| F_{sim}(t) - F_{pd}(t)||_2}{||F_{pd}(t)||_2}\right), \quad (36)$$

where $F_{sim}(t)$ is the simulated specific force generated by the motion platform, $F_{pd}(t)$ is the predefined (reference) specific force corresponding to the real skier motion, $||.||_2$ denotes the Euclidean (L2) norm computed over the simulation time interval.

The PI is computed over the entire simulation duration using discrete-time samples of the signals. This formulation captures both amplitude discrepancies and temporal misalignment (phase distortion) between the simulated and reference signals.

The value of PI ranges between 0 and 1, where, PI = 1 indicates a perfect match between simulated and real motion cues and lower values indicate increasing deviation and reduced motion fidelity. Using this metric, the proposed optimal approach achieves a PI value of 97 % representing the highest performance reported to date. Compared to previously published results [2, 15], where classical methods achieved PI values of 63.25 % and 77.57 %, adaptive approaches reached up to 95 %, and PSO-based optimization attained 96.66 %, the proposed approach provides a clear improvement. This confirms the effectiveness and superiority of the proposed method, establishing it as a state-of-the-art solution for MCA optimization. The results show the effectiveness of the proposed optimal washout filter on many levels: reduce the human sensation error, maximize the shape following factor and use the entire XY-6 DoF platform workspace availability.

5. Conclusions

In this article, we addressed the limitations of existing Motion Cueing Algorithms (MCAs), which often neglect both the human vestibular perception and the efficient use of the simulator workspace. To overcome these challenges, we propose a multi-objective optimal washout filter based on Linear Quadratic Regulator (LQR) theory that explicitly incorporates a mathematical model of the human vestibular system.

The proposed approach minimizes perceptual error while respecting the physical constraints of the motion platform, leading to a significant improvement in motion fidelity. Simulation results demonstrated that the method achieves up to 97 % recovery of human perception, highlighting its effectiveness compared to classical and adaptive approaches.

Furthermore, we introduced a novel redundancy resolution strategy for an 8-DoF hybrid simulator, enabling an optimal distribution of motion between the hexapod and the XY-table. This approach ensures efficient workspace utilization while preserving realistic motion cues, thereby enhancing the overall simulation experience.

Despite these promising results, the current study is limited to simulation-based validation. Future work will focus on integrating a real-time tracking controller that accounts for the coupled dynamics of the vestibular system and the hybrid platform. In addition, experimental validation involving human subjects or humanoid robotic systems will be conducted to further assess the realism and effectiveness of the proposed method.

Overall, this work contributes to the development of more accurate and human-centered motion simulation systems, with potential applications in rehabilitation, training, and immersive virtual environments.

Availability of Data and Materials

Data sharing is not applicable to this article as no datasets were generated or analyzed during the study.

References

[1]. S. Seher, K. Abedi, K. Fatima, S. Badiwala, et al., VR applications and vision-based recognition techniques for sign language: A survey, in *Proceedings of the 16th IEEE International Conference on Computational Intelligence and Communication Networks (CICN)*, 2024, pp. 1527-1533.

[2]. T. Houda, L. Beji, A. Amouri, M. Mallem, Dynamic behavior of an interactive XY-6 DoF simulator for people with reduced mobility, in *Proceedings of the IEEE Conference on Control Technology and Applications (CCTA)*, 2020, pp. 522-527.

[3]. S. de Groot, J. de Winter, M. Mulder, P. A. Wieringa, Nonvestibular motion cueing in a fixed-base driving simulator: Effects on driver braking and cornering performance, *Presence: Teleoperators and Virtual Environments*, Vol. 20, Issue 2, 2011, pp. 117-142.

[4]. R. A. Wynne, V. Beanland, P. M. Salmon, Systematic review of driving simulator validation studies, *Safety Science*, Vol. 117, 2019, pp. 138-151.

[5]. J. G. Allen, P. MacNaughton, J. G. Cedeño-Laurent, X. Cao, et al., Airplane pilot flight performance on 21 maneuvers in a flight simulator under varying carbon dioxide concentrations, *Journal of Exposure Science & Environmental Epidemiology*, Vol. 29, Issue 4, 2019, pp. 457-468.

[6]. Y. Wu, K. Kihara, Y. Takeda, T. Sato, et al., Effects of scheduled manual driving on drowsiness and response to take over request: A simulator study towards understanding drivers in automated driving, *Accident Analysis and Prevention*, Vol. 124, 2019, pp. 202-209.

[7]. E. Perera, G. Villoing, S. Ruffié, Devenir pilote handiski: Valoriser la lenteur pour sécuriser l'expérience de glisse handisportive en station de ski, *Nature & Récréation*, Issue 7, 2019, pp. 22-30 (in French).

[8]. T. Houda, A. Beghdadi, L. Beji, A. Amouri, Multi-complex robot interaction with homothetic human feedback in a virtual environment, *Sensors & Transducers*, Vol. 260, Issue 2, 2023, pp. 15-24.

[9]. N. J. I. Garrett, M. C. Best, Driving simulator motion cueing algorithms - a survey of the state of the art, *Proceedings of the Institution of Mechanical Engineers, Part D: Journal of Automobile Engineering*, Vol. 224, Issue 4, 2010, pp. 537-550.

[10]. T. Houda, A. Amouri, A. Beghdadi, L. Beji, Multi-robot interaction with mixed reality for enhanced perception, in Smart Applications and Data Analysis (M. Hamlich, F. Dornaika, C. Ordonez, L. Bellatreche, et al., Eds.), *Springer*, Cham, 2024, pp. 219-232.

[11]. D. Petrovic, R. Mijailovic, D. Pesic, How to improve the inclusion of drivers with disabilities: Measures to enhance accessibility, mobility, and road safety, *Journal of Transportation Engineering, Part A: Systems*, Vol. 148, Issue 3, 2022, 04021122.

[12]. J. Ku, D. P. Jang, H. B. Ahn, J. Lee, et al., The development and clinical trial of a driving simulator for the handicapped, *Studies in Health Technology and Informatics*, Vol. 85, 2002, pp. 240-246.

[13]. R. A. Telban, F. M. Cardullo, Motion cueing algorithm development: A human-centered approach, Technical Report NASA/CR-2005-213747, *National Aeronautics and Space Administration*, 2005.

[14]. M. A. Nahon, L. D. Reid, Simulator motion-drive algorithms - A designer's perspective, *Journal of Guidance, Control, and Dynamics*, Vol. 13, Issue 2, 1990, pp. 356-362.

[15]. T. Houda, L. Beji, A. Amouri, M. Mallem, Handiski simulator performance under PSO-based washout and control parameters optimization, *Nonlinear Dynamics*, Vol. 108, Issue 3, 2022, pp. 2161-2182.

[16]. H. Şahin, V. H. Dang, E. Sayar, A. Yegenoglu, et al., Fuzzy logic theory-based adaptive reward shaping for robust reinforcement learning (FARS), *arXiv*, 2026, arXiv:2604.15772.

[17]. L. D. Reid, M. Nahon, Flight simulation motion-base drive algorithms: Part 1. Developing and testing equations, Technical Report UTIAS 296, *University of Toronto Institute for Aerospace Studies*, 1985.

[18]. M. R. C. Qazani, H. Asadi, T. Bellmann, S. Pedrammehr, et al., A new fuzzy logic based adaptive motion cueing algorithm using parallel simulation-based motion platform, in *Proceedings of the IEEE International Conference on Fuzzy Systems (FUZZ-IEEE)*, 2020, pp. 1-8.

[19]. S. Nahavandi, Industry 5.0 – A human-centric solution, *Sustainability*, Vol. 11, Issue 16, 2019, 4371.

[20]. A. Gharib, M. Goharimanesh, A. Koochi, M. R. Gharib, Designing an evolutionary optimal washout filter based on genetic algorithm, *Aviation*, Vol. 26, Issue 4, 2022, pp. 193-201.

[21]. A. R. Naseri, P. R. Grant, Difference threshold: Measurement and modeling, in Proceedings of the *International Conference on Motion Perception and Simulation*, 2011.

[22]. T. Houda, A. Beghdadi, L. Beji, A. Amouri, Complex multi-robot hybrid platform for augmented virtual skiing immersion, in *Proceedings of the 3rd IFSA Winter Conference on Automation, Robotics & Communications for Industry 4.0/5.0 (ARCI)*, 2023, pp. 95-99.

[23]. M. Tanaka, F. Matsuno, Modeling and control of head raising snake robots by using kinematic redundancy, *Journal of Intelligent & Robotic Systems*, Vol. 75, Issue 1, 2014, pp. 53-69.
[24]. T. Houda, A. Amouri, L. Beji, M. Mallem, Dynamic parameters optimization and identification of a parallel robot, in Multibody Dynamics 2019 (A. Kecskeméthy, F. Geu Flores, Eds.), *Springer*, Cham, 2020, pp. 285-292.
[25]. A. L. Orekhov, N. Simaan, Directional stiffness modulation of parallel robots with kinematic redundancy and variable stiffness joints, *Journal of Mechanisms and Robotics*, Vol. 11, Issue 5, 2019, 051001.
[26]. S.-H. Cha, T. A. Lasky, S. A. Velinsky, Singularity avoidance for the 3-RRR mechanism using kinematic redundancy, in *Proceedings of the IEEE International Conference on Robotics and Automation (ICRA)*, 2007, pp. 1195-1200.
[27]. J. Baillieul, J. M. Hollerbach, R. W. Brockett, Programming and control of kinematically redundant manipulators, in *Proceedings of the 23rd IEEE Conference on Decision and Control (CDC)*, 1984, pp. 768-774.
[28]. T. Houda, L. Beji, A. Amouri, Multi-objective LQR-based optimization of motion cueing for redundant ski simulator, in *Proceedings of the 6th IFSA Winter Conference on Automation, Robotics & Communications for Industry 4.0/5.0/6.0 (ARCI)*, 2026, pp. 1-13.
[29]. W. E. Omer, K. Abdulhadi, Physiology and diagnostic tests of the vestibular system, in Textbook of Clinical Otolaryngology (A. Al-Mujaddidi, Ed.), *Springer*, Cham, 2020, pp. 169-183.
[30]. F.-O. Bohoua-Nassé, Compréhension et modélisation du comportement conducteur et de sa perception, Master's Thesis, *École des Mines de Paris*, Paris, 2004 (in French).
[31]. L. R. Young, J. L. Meiry, A revised dynamic otolith model, *Aerospace Medicine*, Vol. 39, Issue 6, 1968, pp. 606-608.
[32]. J. Laurens, D. E. Angelaki, The functional significance of velocity storage and its dependence on gravity, *Experimental Brain Research*, Vol. 235, Issue 12, 2017, pp. 3507-3521.
[33]. J. A. Houck, R. J. Telban, F. M. Cardullo, Motion cueing algorithm development: Human-centered linear and nonlinear approaches, Technical Report NASA/TP-2005-213745, *National Aeronautics and Space Administration*, 2005.
[34]. A. Berthoz, I. Viaud-Delmon, Multisensory integration in spatial orientation, *Current Opinion in Neurobiology*, Vol. 9, Issue 6, 1999, pp. 708-712.
[35]. G. L. Zacharias, Motion cue models for pilot-vehicle analysis, Technical Report AMRL-TR-78-2, *Defense Technical Information Center*, 1978.
[36]. S.-H. Chen, L.-C. Fu, An optimal washout filter design with fuzzy compensation for a motion platform, *IFAC Proceedings Volumes*, Vol. 44, Issue 1, 2011, pp. 8433-8438.

Published by International Frequency Sensor Association (IFSA) Publishing, S. L., 2026 (http://www.sensorsportal.com).

IFSA

Open Access Book

Advances in Measurements and Instrumentation: Reviews

Sergey Y. Yurish, Editor

1

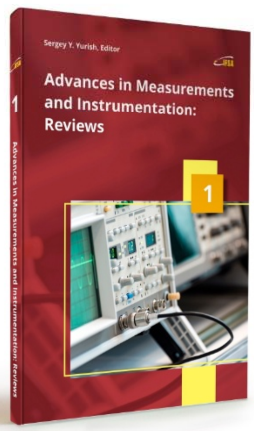

'Advances in Measurements and Instrumentation: Reviews', Book Series, Vol. 1 is covering some aspects related to metrology, sensors, measuring systems and sensor instrumentation as well as modeling and mathematical tools for measurements in a quality control and other applications. The book volume contains seven chapters written by nine contributors from academia and industry from 6 countries: Algeria, Canada, China, Germany, Slovak Republic and United Kingdom.

'Advances in Measurements and Instrumentation: Reviews' will be a valuable tool for those who involved in research and development of various measuring instruments and systems.

http://www.sensorsportal.com/HTML/BOOKSTORE/Advances_in_Measurements_Vol_1.htm

Sensors & Transducers, Vol. 273, Issue 2, June 2026, pp. 62-69

Sensors & Transducers

Published by IFSA Publishing, S. L., 2026
http://www.sensorsportal.com

Development of a Robotic Tool-Handling System for Decontamination in Nuclear Facilities

S. KAZEMI and S. GENTES

Karlsruhe Institute for Technology, Institute of Technology and Management in Construction,
Building 50.33, Am Fasanengarten, 76131 Karlsruhe, Germany
Tel.: +49 721 608-48235
E-mail: siavash.kazemi@kit.edu

Received: 1 April 2026 /Revised: 29 May 2026 /Accepted: 10 June 2026 /Published: 29 June 2026

Abstract: As part of the ROBDEKON [1] project, KIT-TMB is developing a robotic system for positioning two tools used in the decontamination and clearance measurement of concrete walls in nuclear power plants. To achieve this, a lifting platform (Manitou 100-VJR) was equipped with the necessary electronics-including controllers, sensors, actuators, communication modules, and safety systems-and converted into the robotic system "DecontBot" [2]. The machine can be operated in both teleoperation and (semi-)autonomous modes. Additionally, a graphical user interface (GUI) was designed for the DecontBot, allowing users to visualize the system in RViz2 on ROS2 and operate it in an intuitive, user-friendly manner. The DecontBot has been tested and evaluated by various personnel working in nuclear environments to gather feedback. This article provides a detailed description of the development steps of the DecontBot.

Keywords: Robotics, Automation, Decontamination, PLC, Robot operating system (ROS), Nuclear power plant (NPP).

1. Introduction

On April 15, 2023, the last three nuclear power plants in Germany-Emsland, Neckarwestheim 2, and Isar 2-were taken offline. Currently, there are 25 nuclear power plants and research reactors in the country at various stages of decommissioning and dismantling. Globally, it is estimated that around 297 nuclear power plants will begin the decommissioning process by 2030 [3].

To date, decommissioning and dismantling activities have been largely carried out manually. According to organizations such as the OECD, the current technological capabilities in dismantling are not being fully leveraged. By increasing the use of robots and automation technologies, it is possible not only to reduce costs but also to minimize radiation exposure for personnel involved in the process. Considering the large number of nuclear facilities undergoing dismantling, there is significant potential for digital and automated solutions in this field [4].

The ROBDEKON project, commissioned by the Federal Ministry of Research, Technology, and Space (BMFTR), aims to develop autonomous and semi-autonomous robotic solutions to improve safety and efficiency during decontamination in hazardous environments, including nuclear facilities. In collaboration with Karlsruhe University of Applied Sciences and the company Götting KG, KIT-TMB is developing an integrated chain for automating the decommissioning of nuclear power plants [5]. This chain consists of five steps and three robotic systems (see Fig. 1):

1. GammaBot – for environmental exploration, capturing geometric and radiological data;
2. Digitization – utilizing Building Information Modeling (BIM) for facility mapping;

3. Autonomous Decontamination and Clearance Measurement – performed with two robot-portable tools;
4. DecontBot – an autonomous carrier [6, 7];
5. Autonomous Waste Transportation handled by an autonomous forklift [8].

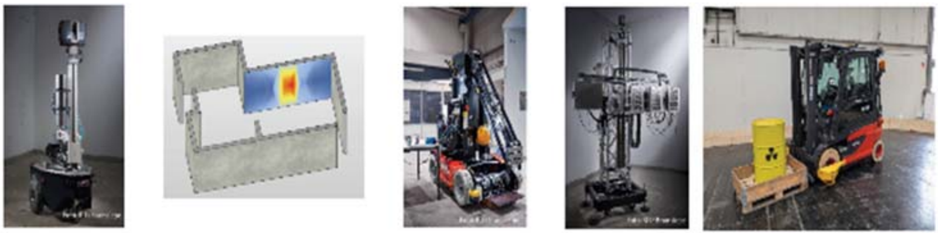

Fig. 1. Closed automated chain for decommissioning of NPPs.

The structure of this article is as follows: Section 2 details the development of the DecontBot, including both the adaptation of the original platform and the implementation of software and hardware components. Section 3 addresses the design of the human-machine interface, system visualization, and data communication while Section 4 describes the primary implementation of the control algorithm to automate the manipulator and Section 5 describes the automation of the vehicle. Section 6 presents the results of functional testing and summarizes feedback obtained from users. Finally, Section 7 provides the conclusions and an outlook on future developments.

A shorter version of this work appeared in ARCI 2026 [7]. This article extends it by introducing a vehicle-motion control framework, presenting initial experiments, and integrating manipulator and vehicle automation into a unified system-level study.

2. Development of DecontBot

To achieve the described objectives, the "Manitou 100-VJR" was further developed and automated as the base vehicle. The platform has approximate dimensions of 1.2 m in length, 1 m in width, and 2 m in height. Its manipulator, featuring three degrees of freedom (DOF), can reach up to 8 m in height with the aid of a telescopic joint and arm, and is capable of positioning tools weighing up to 270 kg.

2.1. Description of the Robot's Main Task

If the locations of hotspots or contaminations are identified using GammaBot, these areas must be decontaminated. To address this, KIT-TMB has developed an automated, robot-portable milling tool for decontaminating concrete walls [9]. Following decontamination, the surfaces are autonomously measured to verify that the contamination has been removed. For this purpose, a second tool, the "Contamination Array" [10], was developed. The primary function of the DecontBot is to position these two tools in either teleoperated or (semi-)autonomous modes [11].

The milling tool shown in Fig. 2 has two degrees of freedom, with a 2.2 kW motor driving the milling head for cutting and a 0.4 kW motor controlling its lateral motion. Safety features include digital switches and sensors that detect surface contact and the end of the milling trajectory, while a current sensor adjusts lateral speed to optimize cutting performance. The tool is powered by a 48 V battery, controlled via a Siemens CPU, and communicates with the DecontBot through UDP and TCP protocols, with a suction unit for dust and debris collection.

Fig. 2. Milling Tool.

The contamination array illustrated in Fig. 3 consists of four parallel detectors that are positioned precisely using linear drives, guided by a laser scanner to avoid obstacles and prevent self-contamination. Measurements are recorded digitally, including position, time, and radiological data, and can be monitored and managed.

Fig. 3. Contamination Array.

Together, these tools enable the DecontBot to perform automated and safe decontamination and radiological assessment tasks in nuclear environments.

2.2. Description of the Integrated Electronics

The foundation of the automated decontamination system is the mobile platform described in Section 2.1. To transform this platform into a (semi-)automated decontamination system, it is first equipped with the necessary components. The control unit (PLC) is connected via a gateway to the sensors used to determine the positions of the manipulator and motor controllers.

The motor controllers, in turn, provide the PLC with essential feedback, including motor current, voltage, and temperature.

For positioning the decontamination system within its environment, two safety-rated LiDAR sensors are mounted on the platform. These sensors can also detect people or objects in the vicinity and, if necessary, trigger a warning signal or an emergency stop to prevent accidents or collisions.

In addition, the platform is equipped with other safety sensors, such as tilt sensors and safety switches, which generate warning signals when a hazard is detected. All warning signals are processed by a safety CPU on the PLC.

The safety system can be partially or fully overridden manually via the GUI if necessary; in such cases, the user receives a warning and assumes full responsibility for system operation.

Additional watchdog mechanisms are implemented to ensure safe communication among hardware components, including the PLC, control PC, operator PC, WLAN, and other connected devices.

Table 1 summarizes the key features and performance metrics of the integrated electronics.

Table 1. Performance metrics.

Cycle Time (PLC)	1 ms
Watchdog Response Time	2 ms
Safety Stop Distance	40 cm
Safety Warning Distance	60 cm
Manipulator Position Measurement Accuracy	Arm: 0.01° Turret: 0.05° Telescope: 0.1 mm
LiDAR Localization Accuracy	x: 0.01 mm y: 0.01 mm yaw: 0.1 °

3. GUI, HMI, Visualization and Data Transfer

The decontamination system is designed to operate in both teleoperation and autonomous modes, providing flexibility depending on the task requirements and the skill level of the operator. To ensure that the system can be used effectively without requiring extensive technical expertise, a user-friendly graphical interface has been developed. This interface allows operators to interact with the system intuitively, monitor its status in real-time, and make adjustments as needed.

In autonomous mode, the decontamination process is guided by the contamination map generated by GammaBot. Using this information, the DecontBot can automatically identify areas of contamination and accurately position its tools for decontamination or clearance measurement. The map data is transmitted directly from GammaBot to the DecontBot via a TCP server/client architecture, enabling seamless integration and continuous data exchange between the two systems.

Through the user interface (Fig. 4), operators can select, load, or delete available maps, initiate or stop the DecontBot, and switch between teleoperation and autonomous operation. The interface also provides critical real-time feedback, including safety release signals, collision warnings, and key system parameters such as manipulator joint positions, battery voltage, and localization status. The selected map is visualized in RViz2 on ROS2, allowing users to view both the 2D layout and the 3D point cloud of the building, alongside a dynamic URDF model of the DecontBot (Fig. 5).

Fig. 4. Graphical user interface (GUI).

This combination of autonomous guidance, real-time visualization, and intuitive control ensures that the DecontBot can operate efficiently and safely, even in complex and partially constrained nuclear environments. By providing operators with clear visualizations and system feedback, the interface reduces cognitive load, improves situational awareness, and allows for precise control of decontamination and measurement tasks. Furthermore, the integration of teleoperation and autonomous modes ensures that the system can adapt to a wide range of operational scenarios, from routine measurements to more challenging environments where human oversight is required.

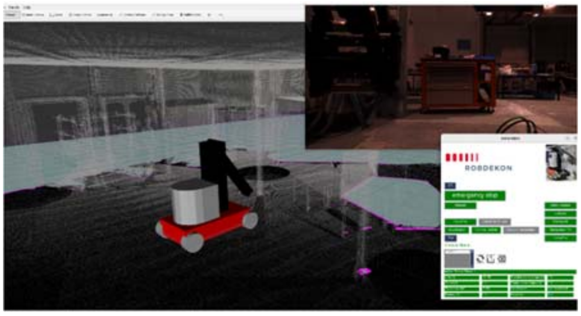

Fig. 5. Visualization via point cloud, camera image and URDF Model.

4. Automation of the Manipulator

For tasks such as robotic-assisted decontamination, ensuring that personnel remain outside hazardous working areas-or at a safe distance-is of paramount importance, often taking precedence over the degree of automation. This safety requirement can be addressed even in systems that rely primarily on teleoperation. Nevertheless, automation is highly recommended and frequently requested by users in the form of an assistant system to improve efficiency, precision, and overall workflow. Typical functionalities of such automation include autonomous navigation between rooms, execution of automated manipulation tasks, automatic positioning of the end effector at specified locations, returning the manipulator to a predefined home position, and independent automatic control of individual manipulator joints.

As illustrated in Fig. 4, the desired position of each manipulator joint can be specified directly through a graphical user interface, after which the manipulator moves to the corresponding configuration. Alternatively, a target point can be defined in task space using Cartesian coordinates, allowing the end effector to be commanded to the desired location. In this case, the desired task-space position is automatically transformed into joint-space positions for each joint through the manipulator's inverse kinematics. The details of the inverse kinematics equations are not included in this article, as they are standard and do not add significant insight to the presented methodology.

This dual approach-allowing both joint-space and task-space command-provides users with flexibility and precision when operating the manipulator, whether in teleoperation mode or during semi-autonomous and fully autonomous tasks. By combining intuitive interface controls with underlying kinematic transformations, the system ensures that manipulator movements are accurate, safe, and repeatable, reducing the risk of operator error while increasing the effectiveness of decontamination operations.

4.1. Controller Design for Manipulator

PID controllers are the most widely used controllers in industry, primarily due to their reliability and simplicity of implementation. In hydraulic systems-such as the manipulator of the DecontBot-where joint speeds are relatively low, the load acting on the end effector is nearly constant, and measurement noise is negligible or adequately filtered, the use of modern or adaptive control strategies is generally unnecessary. In most cases, classical controllers provide satisfactory performance after a one-time parameter tuning.

However, depending on the tool mounted on the DecontBot manipulator-such as a milling tool, contamination array, user-defined tool, or no tool at all-the load, which is directly related to the tool mass, can vary significantly. Consequently, different PID parameter sets are required for different operating conditions. To overcome this limitation, a two-degree-of-freedom (2-DOF) control structure is designed for each joint, consisting of a PI controller combined with a simple neural network-based controller [12], as illustrated in Fig. 6.

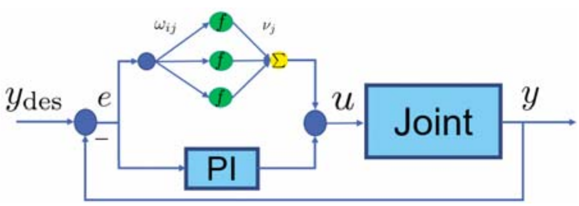

Fig. 6. 2-DOF control architecture with PI and neural network.

The PI component is primarily responsible for position control, while the neural network component provides corrective action by compensating for load-dependent variations in the system dynamics.

The input to the neural network component is the error dynamics, denoted by $I = [e]$.

The output of the hidden layer can be expressed as:

$$net_j^1 = f(I.\omega_{ij}), \quad (1)$$

and the output of the network can be expressed as:

$$u_{nn} = \sum_{j=1}^{M} \vartheta_j \,.\, net_j^1, \quad (2)$$

where i is an index of the network inputs, $e = y_{des} - y$ is a difference between desired position and actual position, $f(\cdot) = \tanh(\cdot)$ is an activation function, M is a number of neurons in the hidden layer, ω_{ij}, ϑ_j are network weights.

The total control law can be calculated as:

$$u = u_{nn} + u_{pi}, \tag{3}$$

or

$$\sum_{j=1}^{M} \vartheta_j . net_j^1 + k_p * e + k_i * \int e\, dt \tag{4}$$

The network parameters can be calculated and optimized online using backpropagation and gradient descent methods, as described in [12]. Table 2 shows the selected PI parameters of controller (4) for each joint and the corresponding position accuracies achieved.

Table 2. PI Parameters and results.

joint	Arm	Telescope	Turret
k_i	5	100	5
k_p.	8	500	12
accuracy	0.1 [°]	5 [mm]	2 [°]

It can be seen that the achieved accuracy of the turret is not fully satisfactory, which is due to the inherent positioning limitations of hydraulic systems caused by mechanical structure. Although this level of accuracy is sufficient for the current application, further improvements are planned to achieve an accuracy of less than 1°.

5. Automation of the Vehicle

Since the primary objective is to autonomously reach designated target points-specifically the contamination points-the vehicle must operate with a high degree of automation. The coordinates for these points are derived from a 3D contamination map generated by GammaBot, where the desired target points are defined as:

$$P_d = [x_d, y_d, z_d]^T \tag{5}$$

The operational workflow requires the vehicle to first navigate to an optimal 2D pose (x, y, θ) within the environment. Once the vehicle is positioned, the manipulator deploys the tools to the precise 3D target coordinates. It is important to note that the vehicle's mobile base may not always achieve the exact 2D coordinates required due to environmental constraints or positioning tolerances. In such cases, the manipulator must compensate by correcting the position not only along the z-axis but also within the x-y plane, provided the target remains within the robotic arm's reachable workspace.

A Point-to-Point (PTP) trajectory planning approach is utilized, which samples the optimal path through discrete iterations. This is implemented on the machine under the following convergence condition:

$$\|e(k)\| < \alpha, \tag{6}$$

where α is a small positive constant. Under this condition, the trajectory tracking problem is treated as a fixed-point control problem. The system advances to the next waypoint in the sequence only when the current tracking error is sufficiently small.

The following sections describe the automation logic and the implementation of the vehicle controller designed to transition the platform from one discrete waypoint to the next.

5.1. Controller Objectives for Vehicle

First step is to calculate distance and angle from start point and desired point as shown in Fig. 7.

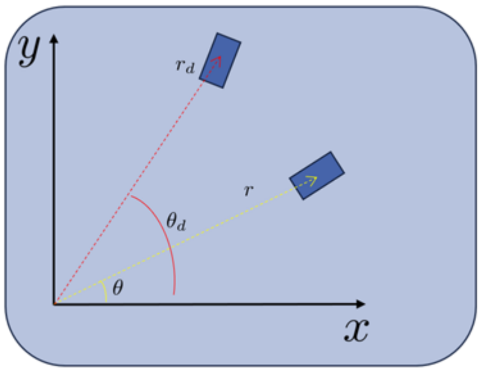

Fig. 7. Current vs. Desired Vehicle Position.

It can be seen that the vehicle needs to rotate from θ to θ_d and move along a distance equal to the magnitude of the vector $|r_d| - |r|$.

Therefore, the following error dynamics are to be minimized by the controller:

$$e_{rot} = \theta_d - \theta, \tag{7}$$

$$e_{lin} = |r_d| - |r|, \tag{8}$$

where θ and r are the current states of the Vehicle.

5.2. Motion Control Strategy

Fig. 8 illustrates the controller designed for the vehicle to perform linear motion. The control strategy uses a two-stage PI controller to ensure accurate and responsive motion.

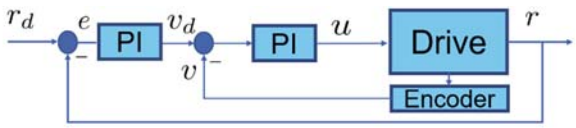

Fig. 8. Linear Motion Control.

First, the linear position error dynamics (difference between desired and current position) are fed into the first PI controller. The output of this controller is the desired velocity v_d for the vehicle. Using encoders, the current velocity v is continuously measured and compared to the desired velocity. The difference between these two signals, defined as the velocity error dynamics, is then used as the input to a second PI controller, which generates the control signal u. This signal u is ultimately implemented as the PWM applied to the drive motors.

This two-stage control strategy is necessary because using a single PI controller (where $u = f(e_{\text{lin}})$) can lead to very slow motion near the end of a trajectory, especially when Δr or e_{lin} is small, since the PWM would become too low to drive the motors effectively. By introducing the intermediate velocity control, the desired velocity is maintained at a sufficient level, ensuring the PWM signal remains strong enough to overcome friction, inclines, or obstacles, even when the position error is small. This allows the vehicle to maintain responsiveness and stability throughout the motion.

Unlike linear motion, the orientation control of the vehicle around the $\boldsymbol{z}$-axis is implemented using a single PD controller.

$$u = k_p * e_{rot} + k_d * \dot{e}_{rot} \tag{9}$$

The derivative (D) component in the PD controller is essential for controlling the vehicle's orientation around the $\boldsymbol{z}$-axis. Without this component, the vehicle exhibits significant overshoot, and the orientation response tends to resemble a sinusoidal oscillation around the desired angle $\boldsymbol{\theta_d}$. Such oscillatory behavior is caused by the system's inertia and the lack of damping in the control loop, which allows the vehicle to continuously overshoot the target orientation before eventually settling. By incorporating a properly tuned D term, these oscillations are effectively damped, providing additional resistance to rapid changes in angular velocity. As a result, the vehicle achieves smooth and stable convergence to the target orientation, with minimal overshoot and reduced settling time.

The choice and tuning of controller parameters are critical in achieving this performance. Table 3 summarizes the parameters of the controllers used for both linear motion and rotational control of the vehicle. These parameters were carefully selected to balance responsiveness and stability: the proportional components ensure the vehicle reacts appropriately to position and orientation errors, while the integral component in the linear motion controller eliminates steady-state errors, and the derivative component in the rotational controller mitigates oscillatory behavior. Together, these settings allow the vehicle to follow the desired trajectory accurately while maintaining smooth and stable motion in both translation and rotation.

Table 3. Parameters of the Controllers.

joint	Linear	Rotational
k_p	900	45
k_d.	-	12
k_i	25	-

5.2. Tests and First Control Results

As an initial test, the vehicle was required to move from the starting position [2.712 m, 0.414 m]with an orientation of $\theta = 4.08°$to the target position [6 m, 1 m]with a desired orientation of $\theta_d = 6°$. Fig. 9 illustrates the start and end positions of the vehicle after completing the movement. After executing the trajectory, the vehicle reached a final position of [5.976 m, 0.9828 m]with $\theta = 4.46°$. These results indicate that the vehicle performs well in terms of linear positioning, achieving a final position very close to the desired target.

While the orientation is slightly off from the desired value, the overall performance of the vehicle in following the planned path is satisfactory for an initial test, demonstrating the effectiveness of the implemented control strategy for basic linear motion.

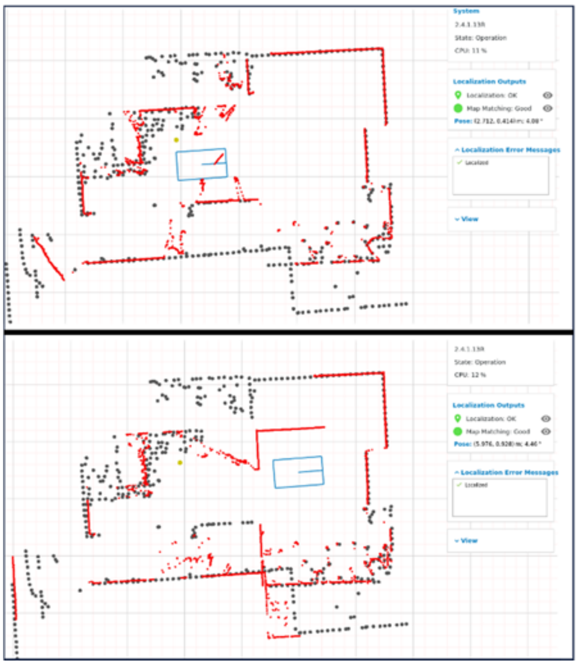

Fig. 9. Start position (top) versus end position (bottom) of the vehicle.

Achieving exact orientation for mobile vehicles with hydraulic steering is inherently challenging, especially when the required change in orientation is small, due to the limited steering dynamics. Therefore, further work on the vehicle's rotational control is needed to reduce the orientation error dynamics below an acceptable threshold.

In cases of larger orientation changes, for example $\Delta\theta = 20°$, the steady-state error remains around 1-2°. A more extensive analysis or statistical evaluation of the remaining error is not provided in this work, as the controller design is still in progress and will be addressed in future studies.

6. Primary Test Results

Understanding the opinions and experiences of actual users is crucial for improving the functionality and acceptance of any engineering system, and the DecontBot is no exception. To gather such feedback, the DecontBot-equipped with its secondary tool, the Contamination Array-was tested in a controlled nuclear laboratory environment at the Institute of Nuclear Waste Disposal (KIT-INE). The primary aim of these tests was to evaluate the system's usability, effectiveness, and overall user experience under realistic operational conditions.

A total of five testers, all professionals working in the field of nuclear engineering but without specialized robotics experience, participated in the evaluation. Each tester interacted with the system for approximately 30 minutes. During this period, the users positioned the contamination array to specific locations and initiated clearance measurements via teleoperation. It is important to note that only the positioning of the tool was controlled manually via teleoperation, while the measurement process itself was carried out automatically by the tool. This separation ensured that the evaluation focused on the human-machine interaction aspects rather than the automated measurement capabilities.

Due to data protection and safety requirements, further details regarding the layout and general characteristics of the testing environment cannot be disclosed in this work. Nonetheless, the testing setup provided sufficient realism to assess the system's practical usability.

In addition to the hands-on evaluation, the users completed a questionnaire consisting of 15 questions, designed to capture detailed feedback on multiple aspects of the system. The questionnaire addressed five categories: general impression, usability, work support, safety and trust, and fun factor. It also included open-ended sections where users could provide suggestions for improvement, such as the implementation of an adjustable step speed for teleoperation. All responses were recorded on a Likert scale from 1 to 5, and the aggregated results are summarized in Fig. 10, providing a visual overview of user ratings across all categories.

Additional tests with other users were also conducted, although these are not described in detail here. Overall, the results were highly encouraging, with the system exceeding expectations in most categories. The fun factor received the highest rating, highlighting the engaging and interactive nature of the system; however, it was observed that this rating tends to decrease slightly as users become more familiar with the system and the tasks begin to feel repetitive. Conversely, increased practice and familiarity led to noticeable improvements in usability and overall impression, suggesting that the system becomes more intuitive and efficient with repeated use. These findings underscore the importance of iterative testing and user feedback in optimizing both the functionality and user experience of complex robotic systems like the DecontBot.

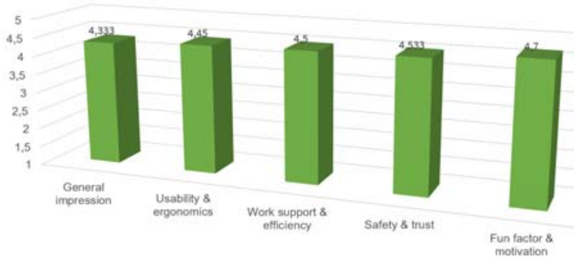

Fig. 10. Test results and user ratings.

7. Conclusions and Further Developments

The mechanical and electrical upgrades of the DecontBot have already been completed, and the platform can currently be operated in teleoperation mode. The next step involves the integration of path planning and advanced control algorithms to enable fully autonomous operation of the vehicle, as the manipulator control has already been successfully implemented. In particular, the control of the vehicle's driving and navigation needs further refinement to ensure precise and smooth movement, especially in complex environments with tight spaces, inclined surfaces, or obstacles. Improvements in driving control will enhance the platform's overall stability, responsiveness, and accuracy, allowing it to follow planned paths reliably without continuous manual intervention.

In addition to autonomous navigation, further degrees of freedom will be added to the end effector to allow more precise positioning of the decontamination and clearance measurement tools on inclined walls, floors, and ceilings. These enhancements will enable the DecontBot to reach areas that are difficult or unsafe for human operators, increasing both the versatility and effectiveness of the platform. The platform's safety will also be thoroughly evaluated and certified by TÜV (Technical Inspection Association), ensuring compliance with rigorous operational and occupational safety standards.

Future tests are planned to encompass not only measurement tasks but also actual decontamination operations using a milling tool. Automation and robot-based solutions have already demonstrated significant potential in decontamination work: they relieve personnel from physically demanding and hazardous tasks, while simultaneously helping to minimize the generation of secondary waste. The DecontBot was therefore specifically developed for the decontamination and clearance measurement of concrete walls in nuclear power plants. By employing the DecontBot, both the effort and the risk associated with these operations can be substantially reduced, making such work safer, faster, and more efficient.

There is strong interest among nuclear power plant operators in adopting autonomous or robotic systems for decontamination work, particularly as these solutions offer the dual benefit of reducing human exposure to radioactive materials and increasing the precision and reliability of decontamination processes. Further development of the driving and navigation control, combined with enhanced tool positioning and autonomous path planning, will be essential to fully realize the potential of the DecontBot and similar robotic platforms in industrial nuclear environments.

References

[1]. J. Petereit, et al., ROBDEKON: Robotic systems for decontamination in hazardous environments, in *Proceedings of the IEEE International Symposium on Safety, Security, and Rescue Robotics (SSRR)*, 2019, pp. 16-23.

[2]. S. Kazemi, S. Gentes, Development of a robot system as a tool-carrier machine for the decontamination process of nuclear power plants, in *Proceedings of the 5th Winter IFSA Conference on Automation, Robotics & Communications for Industry 4.0/5.0 (ARCI)*, 2025, pp. 47-52.

[3]. KernD, Kernkraftwerke außer Betrieb: Leistung und erzeugter Strom, https://www.kernd.de/kernd/themen/strom/Zahlen-und-Fakten/01_index.php#anchor_27a91b5f_Accordion-Kernkraftwerke-ausser-Betrieb (in German).

[4]. A. D. Little, Statista, Rückbau von Kernkraftwerken weltweit bis zum Jahr 2030, https://de.statista.com/statistik/daten/studie/201684/umfrage/rueckbau-von-kernkraftwerken-weltweit/ (in German).

[5]. S. Gentes, et al., From environmental exploration to clearance measurement – developing mobile robot systems for decommissioning of nuclear power plants, *at - Automatisierungstechnik*, Vol. 70, Issue 10, 2022, pp. 886-896.

[6]. S. Kazemi, Robotic automation for nuclear decommissioning: Development of a tool carrier system with milling and clearance measurement capabilities, *Sensors & Transducers*, Vol. 268, Issue 1, 2025, pp. 28-36.

[7]. S. Kazemi, S. Gentes, Design and development of a robotic tool-carrier for nuclear power plant decontamination, in *Proceedings of the 6th Winter IFSA Conference on Automation, Robotics & Communications for Industry 4.0/5.0/6.0 (ARCI)*, 2026, pp. 24-27.

[8]. Götting KG, Hannover Messe 2024, https://www.goetting.de/hannover-messe-2024/ (in German).

[9]. C. Li, S. Kazemi, S. Gentes, Development of an automated milling system for the decontamination of the wall surface in a nuclear power plant, *Safety of Nuclear Waste Disposal*, Vol. 1, 2021, pp. 23-24.

[10]. A. Wernke, Automatisierung der Kontaminationsmessung im Rückbauprozess kerntechnischer Anlagen, *atw – International Journal for Nuclear Power*, Vol. 67, Issue 5, 2022 (in German).

[11]. S. Kazemi, S. Gentes, Development of a robotic system for the automation of the decontamination process of nuclear power plants, *Safety of Nuclear Waste Disposal*, Vol. 2, 2023, pp. 13-14.

[12]. S. Kazemi, S. Gentes, Self-constructing neural network controllers with adaptive structural learning: Application to stepper motor positioning, in *Proceedings of the 13th International Conference on Control, Mechatronics and Automation (ICCMA)*, 2025, pp. 231-236.

CC BY

Published by International Frequency Sensor Association (IFSA) Publishing, S. L., 2026 (http://www.sensorsportal.com).

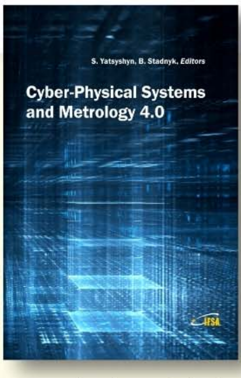

Cyber-Physical Systems and Metrology 4.0

S. Yatsyshyn and B. Stadnyk, Editors

The book is written by 30 authors whose scientific achievements for the last 5 years cover a significant information technology and measurement science areas.

The purpose of this title is to present and consider the main trends in the field of metrology of Cyber-Physical Systems, which are becoming a key element of everyday life. At the first, the book is intended for engineers, lecturers, students, persons who are not acquainted enough with the specificity of Cyber-Physical Systems and their Metrology, but are interested in it.

Formats: hardcover (print book) and PDF, 332 pages

ISBN: 978-84-09-26899-3, e-ISBN: 978-84-09-26898-6

IFSA Publishing

https://www.sensorsportal.com/HTML/BOOKSTORE/Cyber-Physical_Systems_and_Metrology_4_0.htm

Sensors & Transducers, Vol. 273, Issue 2, June 2026, pp. 70-78

Sensors & Transducers
Published by IFSA Publishing, S. L., 2026
http://www.sensorsportal.com

Human-Centric AI in Industry 6.0: How Marketing Narratives Align with User Experience in Organizations

Neviana KRASTEVA, Tsvetan DAVIDKOV and Aleksey POTEBNYA
Sofia University "St. Kliment Ohridski", Faculty of Economics and Business Administration,
125 Tsarigradsko shose blvd., Sofia 1000, Bulgaria
E-mail: nevianak@feb.uni-sofia.bg, tzvetandavidkov@feb.uni-sofia.bg,
aleksey.potebnia@feb.uni-sofia.bg

Received: 26 March 2026 /Revised: 30 April 2026 /Accepted: 29 May 2026 /Published: 29 June 2026

Abstract: This article extends our ARCI' 2026 conference paper by providing an expanded state-of-the-art and a replicable analytical approach to the relationship between human-centric marketing narratives and users' experience of artificial intelligence in organizational settings. Building on the human-centric orientation of Industry 5.0 and emerging Industry 6.0 discussions, the study examines how partnership and efficiency narratives set expectations, while perceived usefulness, autonomy constraints, and transparency shape lived experience at work. Evidence is triangulated across a survey of AI tool users, semi-structured interviews and open-ended responses, and a content analysis of marketing artifacts coded for narrative frames such as assistant/partner positioning, anthropomorphic cues, creativity support, and trust and ethical claims. Results indicate that narrative emphasis on partnership and productivity is common, yet users' perceived harmony depends on transparent governance and preserved autonomy. The article concludes that Industry 6.0 'harmony' should be treated as a governance and design challenge rather than a branding claim.

Keywords: Industry 6.0, Human-centered AI, Marketing narratives, User experience, Trust, Transparency, Organizational AI.

1. Introduction

The rapid evolution of artificial intelligence, automation and digitalization has accelerated the shift between industrial paradigms – from the automation of Industry 3.0 to the cyber-physical systems and connected production environments of Industry 4.0 [1, 2]. Industry 5.0 reintroduced the human being as a central element of technological systems, emphasizing sustainability, resilience and the development of ethical and trustworthy artificial intelligence [3]. Recent discussions of Industry 6.0 extend this trajectory by framing socio-technical ecosystems in which intelligent systems co-evolve with human goals, operate under accountable governance, and support value-aligned collaboration at scale [4-6].

This transition intensifies a longstanding tension: organizations increasingly expect humans to exhibit machine-like consistency and efficiency, while artificial intelligence is frequently framed as approximating human intuition, creativity and empathy. Against this background, this extended paper investigates how human-centric marketing narratives align with user experience in organizational contexts. It expands the state-of-the-art across human-centered artificial intelligence and marketing narrative scholarship, and it provides a replicable coding scheme for narrative frames and a transparent linkage between narratives, user experience dimensions and governance conditions.

Relationship to the ARCI' 2026 conference paper. A shorter conference version of this study was published in the ARCI' 2026 proceedings [12] and presented an initial conceptual framing of the human-centric gap together with pilot descriptive evidence. The present journal article constitutes a distinct and substantially expanded work. Specifically, it (i) extends and updates the state-of-the-art across human-centered AI, trust and governance, and marketing narrative scholarship; (ii) reports the full measurement instrument (item wording, scale construction and reliability) and the full statistical reporting for H1–H3 (tests, effect sizes and model coefficients); (iii) provides a complete narrative framing codebook (NF1–NF5) with conservative coding rules and replication-oriented appendices; and (iv) expands the discussion into actionable governance and communication measures (Table 9) to reduce the gap between branding claims and organizational experience. Any overlapping prose with the proceedings paper has been rewritten and restructured so that the journal article reads as a standalone contribution rather than an expanded proceedings text.

2. Related Work

2.1. Human-Centered Artificial Intelligence, Trust and Governance

Human-centered artificial intelligence emphasizes the design and deployment of intelligent systems that support human agency, safety and accountability. Shneiderman's framework highlights human control, responsibility and reliability as core design commitments, with governance mechanisms required to keep autonomy and oversight in the loop [7]. From a policy perspective, the OECD Artificial Intelligence Principles provide a widely adopted baseline for transparency, robustness, accountability and human-centered values in artificial intelligence deployment [6].

At the organizational level, autonomy constraints are amplified in settings of algorithmic management, where monitoring and automated evaluation may reconfigure control and accountability in the workplace [8]. Trust in artificial intelligence is shaped not only by performance but also by perceived transparency, explainability and the ability to contest or correct automated decisions. A synthesis of empirical research on trust in artificial intelligence shows that trust is dynamic and context-sensitive, and that overreliance and underreliance can both emerge when users cannot calibrate system capabilities and limits to their task context [9].

Beyond compliance, governance in human-centered AI can be understood as a set of organizational capabilities: setting clear boundaries for automated decision-making, ensuring traceability of outputs, and maintaining meaningful human oversight. In practice, these capabilities determine whether users can challenge, correct, or override AI-assisted recommendations, which in turn shapes perceived agency and responsibility in socio-technical systems [6, 7].

The trust literature emphasizes that trust calibration is not a one-off attitude but an ongoing process influenced by feedback loops, transparency cues, and users' prior experiences with similar systems. When systems are presented as highly capable but provide limited explanation or error-handling guidance, miscalibration becomes likely, producing either overreliance (automation bias) or defensive avoidance [9].

These concerns are particularly salient under algorithmic management. Monitoring, performance scoring, and automated workflow coordination may increase efficiency, yet they can also shift control from workers to opaque metrics and reduce discretion, thereby reconfiguring autonomy and accountability in everyday work settings [8].

A practical implication is that 'human-centric' deployment requires measurable governance indicators. Examples include availability of explanation interfaces, documented accountability for AI-assisted decisions, and clear escalation pathways when users disagree with algorithmic outputs. Such indicators operationalize the OECD principles as organizational practices rather than abstract commitments [6].

In addition, human-centered design implies that user experience should be evaluated not only by task efficiency but also by perceived fairness, contestability, and the preservation of discretion. These dimensions are especially important in knowledge work where judgment and creativity remain central, and where generative AI systems may influence decisions through persuasive language rather than transparent reasoning [7, 9].

2.2. Marketing Narratives, Anthropomorphism and Expectation Setting

Marketing communication increasingly frames artificial intelligence products through narrative devices such as assistant or partner metaphors, and through anthropomorphic cues that invite social interpretation. In consumer research, anthropomorphism can increase perceived warmth and compatibility when cues are congruent with user schemas, while incongruence may increase skepticism or perceived manipulation [10].

In the context of generative artificial intelligence brands, recent work suggests that anthropomorphic brand positioning can strengthen identification and engagement, but may also raise ethical concerns when narratives overstate empathy or agency beyond actual system behavior [11]. For Industry 6.0, where 'harmony' is often promoted as a socio-technical promise, the key analytical question is whether narrative frames are matched by implementation conditions – especially transparency, accountability and preserved autonomy – such that users' lived experience aligns with branding claims [4-6].

From a narrative perspective, assistant and partner metaphors function as cognitive shortcuts that frame expectations about responsibility and agency. When branding implies collaboration and mutual adaptation, users may infer that systems will be responsive, transparent, and aligned with human intentions. In practice, these inferences become fragile if organizational deployment emphasizes surveillance or rigid standardization rather than support and co-creation [8-10].

Anthropomorphic cues are especially influential for generative AI, where conversational interfaces and human-like language can amplify social responses. Schema congruity theory suggests that anthropomorphism can be persuasive when cues match users' expectations and task contexts, but can backfire when cues are perceived as deceptive or manipulative [10]. Accordingly, humanized brand positioning may increase engagement while simultaneously raising the stakes for perceived ethical conduct and accountability [11].

This creates a practical question for Industry 6.0 communication: how to signal 'harmony' without overstating empathy or autonomy. A conservative interpretation is that harmony is conditional on governance, transparency, and preserved human override rights, rather than on anthropomorphic presentation alone [4-7].

Industry 6.0 narratives also intersect with 'management fashion' dynamics. As new labels diffuse, organizations may adopt human-centric language as a signal of modernity and responsibility even when implementation changes are partial. This creates the risk that human-centricity becomes a symbolic resource in communication rather than a consistently implemented design principle [5].

From this perspective, marketing narratives can be evaluated not only by their prevalence but also by their specificity. Vague promises of partnership and harmony are less credible than concrete claims about transparency measures, data practices, user override rights, and accountability structures. Such specificity is also more consistent with the policy-oriented language of trustworthy AI [6].

Ethically, anthropomorphic branding may create asymmetric expectations: users may attribute intention, empathy, or responsibility to systems that are not designed to hold such properties. When outcomes contradict these expectations, disappointment can translate into broader distrust toward both the technology and the organization deploying it. Therefore, expectation management becomes a substantive component of responsible AI communication [9-11].

3. Theoretical Framework and Conceptual Model

Industry 4.0 established automation and networked cyber-physical systems as core drivers of industrial competitiveness [1, 2]. Industry 5.0 added an explicit human-centric and resilience-oriented agenda [3]. Industry 6.0 discourse extends this trajectory by emphasizing adaptive socio-technical ecosystems, participatory governance and value-aligned human–artificial intelligence collaboration [4-6].

Table 1. Evolution from Industry 4.0 to Industry 6.0 in terms of dominant logic, human role and governance orientation.

Dimension	Industry 4.0	Industry 5.0	Industry 6.0
Primary focus	Automation and efficiency	Human-centricity and resilience	Harmony between humans, artificial intelligence and society
Dominant logic	Technological optimization	Responsible technology	Adaptive socio-technical ecosystem
Role of humans	System operators / resources	Central stakeholders	Co-adaptive partners
Role of AI	Decision support and automation	Assistive and explainable systems	Context-aware and value-aligned intelligence
Design principle	Performance optimization	Ethical and human-centric design	Participatory and adaptive design
Governance orientation	Technical standards	Ethical guidelines	Accountable and participatory governance
Marketing narratives	Productivity and innovation	Trust and responsibility	Harmony, partnership and empathy
Risk	Dehumanization of work	Symbolic human-centricity	Human-centricity as branding rather than practice

Building on this framing, we conceptualize a 'human-centric gap' as the divergence between (i) marketing narrative frames that emphasize partnership, empowerment and ethical alignment and (ii) user experience reports that reflect simultaneous usefulness and autonomy constraints. The analytical logic links narrative frames to three user experience dimensions: perceived usefulness/efficiency, perceived autonomy constraints and perceived transparency and ethical alignment. Transparency and ethics are treated as enabling conditions that may reduce autonomy costs.

4. Methodology

The study triangulates evidence from three sources: a survey capturing user experience of artificial intelligence tools in organizational environments, semi-structured interviews and open-ended responses that contextualize trust and boundary-setting, and a content analysis of marketing artifacts used to operationalize narrative framing. The approach is designed to be replicable and to support transparent mapping between constructs, evidence and claims. Illustrative survey item wording and the narrative framing codebook are provided in Appendices A-C.

4.1. Survey Measures

All closed-ended survey items use a 5-point Likert scale (1 = strongly disagree; 5 = strongly agree). A structured questionnaire was administered to participants with exposure to AI-enabled tools in organizational environments (N = 87). The survey operationalizes three constructs: perceived usefulness/efficiency (U), perceived autonomy constraints and algorithmic control (A), and perceived transparency and ethical alignment (T). Table 2 provides illustrative items to support construct transparency and replication.

Sample recruitment and inclusion criteria. Participants were recruited via a combined strategy, including invitations disseminated through organizations where AI-enabled tools are used and voluntary participation of students and professionals with direct exposure to AI-supported work or study practices. Inclusion criteria required (i) active use of at least one AI-enabled tool in organizational or educational tasks and (ii) a minimum of one month of repeated exposure sufficient to form stable perceptions of usefulness, autonomy constraints and transparency/ethics. Because the sample is relatively small and cross-sectional, and organizational contexts vary, all quantitative results are interpreted as exploratory and indicative rather than as population-level estimates.

The sample is a convenience sample and should not be treated as representative of any specific sector or country-level workforce. Sectoral differences and monitoring regimes may influence perceptions; therefore, the findings are interpreted as exploratory and hypothesis-generating.

Table 2. Illustrative survey items for user experience constructs (5-point Likert scale).

Construct	Indicator focus	Example item (illustrative)
U (Usefulness)	Efficiency and task support	The AI tool helps me complete tasks faster and with fewer errors.
U (Usefulness)	Decision support	The AI tool improves the quality of my work decisions.
A (Control constraints)	Monitoring and autonomy	AI-based systems in my workplace increase monitoring of my performance.
A (Control constraints)	Constraint perception	Using AI tools reduces my freedom to choose how to complete tasks.
T (Transparency/ethics)	Explainability	I understand on what basis the AI tool produces its outputs.
T (Transparency/ethics)	Accountability	There are clear rules and responsibilities for how AI is used in my organization.

4.2. Interviews and Open-Ended Responses

Semi-structured interviews and open-ended responses were analyzed using thematic coding. Coding categories were anchored in the three user experience constructs and extended inductively for themes such as boundary-setting, role clarity, perceived fairness and trust calibration. The qualitative evidence is used to interpret mechanisms behind quantitative patterns and to qualify where narrative framing aligns with lived practice.

4.3. Content Analysis and Narrative Framing

Marketing narratives were operationalized as narrative frames coded in a corpus of 24 marketing artifacts collected within a one-month window. Each artifact was coded for the presence (1) or absence (0) of five frames: assistant or partner framing, anthropomorphism and affective cues, creativity support or empowerment, trust and ethical claims, and productivity or efficiency emphasis. Table 3 summarizes the coding scheme and frame prevalence in the corpus.

4.4. Operationalization and Analytical Strategy

To support transparency and replicability, the study links each empirical claim to a corresponding construct and evidence source. User experience outcomes are operationalized through three constructs measured on 5-point Likert-type scales: perceived usefulness/efficiency (U), perceived autonomy constraints and algorithmic control (A), and perceived transparency and ethical alignment (T). For the narrative domain, marketing materials are coded into narrative frames (NF) that capture recurring positioning strategies such as partner metaphors, productivity emphasis, and trust/ethics claims.

The analytical strategy follows a triangulation logic: (i) NF prevalence is used to describe dominant marketing narratives; (ii) survey and qualitative evidence is used to characterize how users experience usefulness, control, and transparency; and (iii) cross-source interpretation assesses whether partnership and harmony framing is matched by governance-related conditions in lived organizational practice. This approach prioritizes interpretive validity over post-hoc statistical optimization and supports comparison across future replications.

Table 3. Narrative frames (NF) and prevalence in the marketing corpus (n = 24 artifacts).

Narrative frame	Definition (summary)	Count	Percent
Assistant/partner framing	AI positioned as helper, partner or copilot	20	83.3 %
Anthropomorphism/affective cues	Human-like traits, emotions, social cues	10	41.7 %
Creativity support/empowerment	Claims of creativity or capability enhancement	13	54.2 %
Trust/transparency/ethical claims	Responsible AI, transparency, safety, ethics	15	62.5 %
Productivity/efficiency emphasis	Efficiency, performance, cost reduction	19	79.2 %

Coding procedure and quality control. Prior to coding, the narrative framing definitions (NF1–NF5) and the conservative inclusion rule were reviewed against a small calibration subset to harmonize interpretation of ambiguous marketing language. Coding decisions followed a conservative principle: frames were marked only when a cue was explicitly contextualized by surrounding claims (e.g., adjacent statements about user control rights, transparency features, or explicit productivity metrics). Disagreements identified during internal checks were resolved through documented discussion and consensus, and the final coding file preserves the rationale for boundary cases. Given the limited corpus size and the exploratory scope, narrative frame prevalence is reported descriptively as an indicator of dominant framing patterns rather than as a basis for broader inferential claims.

Table 4. Hypotheses and evidence mapping (constructs, measures and evidence sources).

Hypothesis / focus	Key constructs	Operationalization	Evidence source	Interpretation criterion
H1: Useful yet controlling	U vs. A	U high with coexisting autonomy constraints	Survey + interviews	Ambivalence: usefulness coexists with monitoring/control cues
H2: Control undermines harmony	A, T	Higher A with lower perceived transparency and trust conditions	Survey + qualitative themes	Control becomes salient when transparency/contestability are weak
H3: Transparency as condition	T and governance	Transparency/ethics enable ‘partner’ framing to be credible	Triangulation with NF	Harmony framing aligns only under accountability and oversight conditions

4.5. Validity Considerations and Limitations

The mixed-method design supports construct and interpretive validity through triangulation, yet several limitations should be noted. First, survey measures capture perceptions at a single point in time and may reflect local organizational policies as much as system properties. Second, the marketing corpus is bounded to a one-month window and a limited set of publicly available artifacts; it represents dominant narratives but not the full diversity of organizational communication. Third, the qualitative evidence emphasizes mechanisms and conditions rather than statistical generalization. These limitations motivate future replications with broader sectoral coverage and longitudinal designs.

5. Results

5.1. Sample Characteristics

The survey included N = 87 respondents with exposure to AI-enabled tools in organizational environments. Table 5 summarizes the sample profile.

5.2. Scale Reliability and Descriptive Statistics

Internal consistency was assessed for the multi-item constructs measured on a 5-point Likert scale. Cronbach’s alpha indicated acceptable reliability for usefulness/efficiency (U; 5 items; $\alpha = 0.680$), algorithmic control constraints (A; 3 items; $\alpha = 0.600$), and transparency/ethical alignment (T; 5 items; $\alpha = 0.750$). Autonomy was operationalized as $A^* = 6 - A$, and perceived harmony as $H = (U + A^*)/2$. Table 6 reports descriptive statistics and reliability coefficients.

Note: Scale reliability for algorithmic control constraints (A) is borderline ($\alpha = 0.60$). Given the exploratory design and the short 3-item scale, this value is treated as acceptable for initial investigation; however, future work should expand the item pool and validate the construct across larger and sector-specific samples.

5.3. Narrative Framing Prevalence in Marketing Materials

Narrative framing (NF) prevalence in the marketing corpus is summarized in Table 3 (n = 24 artifacts).

5.4. Hypothesis Testing

H1 (helpful but controlling). A Wilcoxon signed-rank test comparing U with autonomy ($A^* = 6 - A$) indicates a statistically significant difference ($Z = 7.671$, $p < 0.001$), with a large effect size ($r = 0.822$). The direction supports the interpretation that AI is perceived as operationally useful while autonomy is comparatively lower.

H2 (control reduces harmony). The Spearman association between algorithmic control constraints (A) and the harmony index (H) is negative ($\rho = -0.633$, $p < 0.001$). However, because H is partially constructed from A via $A^* = 6 - A$, this association is reported as a consistency check rather than as an independent confirmation of H2. Accordingly, we interpret H2 primarily through complementary evidence (H1 and H3) and through qualitative mechanisms linking control salience to transparency/contestability conditions.

Methodological note for H2. Because the harmony index H is partially constructed from autonomy ($A^* = 6 - A$), the correlation between A and H is not fully independent and should not be interpreted as a stand-alone empirical confirmation. Therefore, we treat the A–H association as a consistency check and emphasize cleaner complementary evidence, including (i) the within-subject U vs. A* difference test (H1) and (ii) the moderation model (H3) showing how transparency/ethics conditions the usefulness–control relationship.

H3 (transparency moderates the usefulness–control relationship). Moderation regression with mean-centered predictors shows a significant interaction between usefulness and transparency (U×T; $\beta = -0.394$, $p = 0.008$), suggesting that higher transparency/ethical alignment attenuates the association between perceived usefulness and perceived control constraints.

Table 5. Sample characteristics (N = 87).

Variable	Category	n	%
Gender	Female	65	74.7 %
	Male	22	25.3 %
Age	Under 25	23	26.4 %
	25-40	43	49.4 %
	Other ages	21	24.1 %
Sector	Education	21	24.1 %
	Services	18	20.7 %
	Technology	9	10.3 %
	Production	3	3.4 %
	Other (e.g., trade/student/other)	36	41.4 %
AI/automation use in the organization	Yes	58	66.7 %
	Partly	23	26.4 %
	No	6	6.9 %
Awareness of Industry 5.0/6.0	Yes	14	16.1 %
	No	73	83.9 %

Table 6. Construct descriptives and reliability (N = 87; 5-point Likert scales).

Construct	Items	Mean	SD	Cronbach's α
Usefulness / Efficiency (U)	5	3.593	0.581	0.680
Algorithmic control constraints (A)	3	3.632	0.629	0.600
Transparency & ethical alignment (T)	5	3.175	0.669	0.750
Autonomy (A* = 6 − A)	computed	2.368	0.629	–
Harmony index (H)	computed	2.980	0.364	–

Note: Cronbach's α is reported only for multi-item scales (U, A, T). Computed indices (A*, H) are derived variables and do not have α.

Table 7. Spearman correlation matrix (ρ).

	U	A	T	H
U	1.000	0.243*	0.030	0.551***
A	0.243*	1.000	-0.191	-0.633***
T	0.030	-0.191	1.000	0.171
H	0.551***	-0.633***	0.171	1.000

Note: Spearman correlations (two-tailed). * $p < 0.05$; ** $p < 0.01$; *** $p < 0.001$.

Table 8. Moderation regression predicting algorithmic control constraints (A).

Predictor	β	SE	t	p
Intercept	3.631	0.061	59.089	< 0.001
U (centered)	0.251	0.108	2.329	0.022
T (centered)	-0.187	0.093	-2.020	0.047
U×T	-0.394	0.145	-2.720	0.008

Note: Predictors are mean-centered. N = 87. Model fit: $R^2 = 0.198$; Adj. $R^2 = 0.169$. Unstandardized coefficients are reported.

6. Discussion

The findings support the existence of a human-centric gap: narrative frames that emphasize harmony and partnership do not, on their own, ensure user experience consistent with preserved autonomy. In Industry 6.0 discourse, harmony should therefore be treated as a governance and design outcome that depends on transparent accountability regimes and participatory control mechanisms. From a marketing perspective, anthropomorphic cues may increase initial engagement, but can undermine trust when users encounter monitoring or autonomy constraints that contradict the partner narrative [9-11].

Implications for governance and management are straightforward. Organizations that deploy AI at scale should treat transparency and contestability as core design requirements, not as optional communication add-ons. This includes clear documentation of data use, role definitions for accountability, and explicit pathways for appeal and correction when AI outputs affect evaluations or decisions. Such measures translate trustworthy AI principles into workplace practice [6, 8].

Implications for marketing and communication follow the same logic. Anthropomorphic cues can increase initial engagement, but sustainable trust depends on the consistency between promises and experienced constraints. More credible positioning emphasizes bounded assistance, clearly stated limitations, and user control rights, thereby reducing the probability that a ‘partner’ narrative will be perceived as manipulative when monitoring or automation intensifies [10, 11].

Future work should refine and validate measurement instruments for autonomy, transparency, and perceived governance quality, and test interventions that reduce autonomy costs while sustaining usefulness. A particularly valuable direction is comparative analysis across sectors with different monitoring regimes and accountability cultures.

To translate the Industry 6.0 harmony proposition into actionable practice, Table 9 summarizes governance and communication measures that support alignment between narrative positioning and organizational experience.

Table 9. Practical measures for reducing the human-centric gap (governance and communication).

Gap driver	Risk in practice	Governance / design measure	Communication implication
Low transparency	Mistrust, miscalibration	Explainability interfaces; clear data-use statements	Avoid vague assurances; disclose limits
Limited contestability	Perceived loss of agency	Appeal/override pathways; human-in-the-loop checkpoints	State user control rights explicitly
Algorithmic monitoring	Control without accountability	Documented accountability roles; audit logs	Do not label surveillance as ‘partnership’
Anthropomorphic overclaim	Expectation backlash	Bounded capability statements; UX testing for deception risk	Use conservative metaphors; avoid ‘empathy’ claims
Productivity-only framing	Dehumanization	Balanced KPIs including autonomy and wellbeing	Include autonomy and fairness in value proposition
Unclear responsibility	Blame shifting	RACI matrix for AI outputs; escalation owners	Communicate responsibility and escalation points

7. Conclusions

This extended paper links Industry 6.0 human-centric claims to a replicable analysis of marketing narratives and organizational user experience. The contribution is twofold: (i) an expanded synthesis of human-centered artificial intelligence and marketing narrative scholarship, and (ii) a practical coding approach for assessing the alignment between branding discourse and lived practice. Future work should refine measurement instruments, broaden sectoral coverage and evaluate governance interventions that reduce autonomy costs while sustaining usefulness.

Overall, the extended contribution lies in making the ‘human-centric’ claim empirically assessable: marketing narratives are treated as observable frames, and user experience is decomposed into measurable perceptions of usefulness, autonomy constraints, and transparency. This framing enables future studies to compare sectors, track changes over time, and evaluate whether governance interventions reduce the gap between branding and practice.

A shorter conference version of this work was published in the ARCI’ 2026 proceedings [12].

Acknowledgements

This study was funded by the Ministry of Education and Science of Bulgaria (MES) under the National Science Fund, Competition for Fundamental Scientific Research 2024, Contract No. КП-06-Н85/3 dated December 5, 2024.

References

[1]. K. Schwab, The Fourth Industrial Revolution, *World Economic Forum*, Geneva, 2016.
[2]. H. Kagermann, W. Wahlster, J. Helbig, Recommendations for Implementing the Strategic Initiative Industrie 4.0, *acatech*, Munich, 2013.
[3]. M. Breque, L. De Nul, A. Petridis, Industry 5.0: Towards a sustainable, human-centric and resilient European industry, *Publications Office of the European Union*, Luxembourg, 2021.
[4]. A. Fernández-Miguel, F. E. García-Muiña, D. Settembre-Blundo, S. C. Tarantino, et al., Exploring systemic sustainability in manufacturing: Geoanthropology’s strategic lens shaping Industry 6.0, *Global Journal of Flexible Systems Management*, Vol. 25, 2024, pp. 579-600.
[5]. D. Ø. Madsen, K. Slåtten, T. Berg, From Industry 4.0 to Industry 6.0: Tracing the evolution of industrial paradigms through the lens of management fashion theory, *Systems*, Vol. 13, Issue 5, 2025, 387.
[6]. OECD AI principles, https://oecd.ai/en/ai-principles
[7]. B. Shneiderman, Human-Centered AI, *Oxford University Press*, Oxford, 2022.
[8]. International Labour Organization, Algorithmic management in the workplace, https://www.ilo.org/algorithmic-management-workplace
[9]. E. Glikson, A. W. Woolley, Human trust in artificial intelligence: Review of empirical research, *Academy*

of Management Annals, Vol. 14, Issue 2, 2020, pp. 627-660.
[10]. P. Aggarwal, A. L. McGill, Is that car smiling at me? Schema congruity as a basis for evaluating anthropomorphized products, *Journal of Consumer Research*, Vol. 34, Issue 4, 2007, pp. 468-479.
[11]. K. Hussain, Humanizing generative AI brands: How brand anthropomorphism converts customers into brand heroes, *Computers in Human Behavior Reports*, Vol. 19, 2025, 100707.
[12]. N. Krasteva, T. Davidkov, A. Potebnya, Human-centric design, marketing narratives and user experience in human-AI interaction: Evidence from the Industry 6.0 transition, in *Proceedings of the 6th IFSA Winter Conference on Automation, Robotics & Communications for Industry 4.0/5.0/6.0 (ARCI)*, 2026, pp. 35-39.

Appendix A. Illustrative Survey Item Wording (5-point Likert Scale)

Scale anchors: 1 = Strongly disagree; 5 = Strongly agree.

Usefulness / efficiency (U):

U1. The AI tools used in my work help me complete tasks more efficiently.

U2. AI improves the quality of my work outputs.

U3. AI reduces routine workload.

U4. AI supports better decision-making in my tasks.

U5. Overall, AI increases my productivity.

Autonomy constraints / algorithmic control (A):

A1. AI-based systems in my workplace increase monitoring of my work.

A2. AI tools constrain my discretion in how I perform tasks.

A3. AI-based metrics influence evaluations of my performance.

Transparency and ethical alignment (T):

T1. It is clear to me how AI-based recommendations are generated.

T2. I understand what data is used by AI tools in my workplace.

T3. AI decisions in my workplace can be questioned or appealed.

T4. AI tools are used in a way that is consistent with ethical standards.

T5. Responsibilities for AI outcomes are clearly defined.

Appendix B. Narrative Framing Codebook (NF): Definitions and Inclusion Rules

Each marketing artifact was coded for the presence (1) or absence (0) of the following frames. Frames were coded only when the cue was supported by surrounding context (conservative rule).

NF1 Assistant/partner framing: AI positioned as a collaborator (e.g., assistant, copilot, partner, teammate).

NF2 Anthropomorphism/affective cues: Human-like traits, emotions, or ‘friend’ metaphors that invite social interpretation.

NF3 Creativity support/empowerment: Claims that AI enables creativity, learning, ideation, or co-creation.

NF4 Trust/transparency/ethical claims: References to responsible AI, transparency, safety, accountability, privacy, compliance, or explainability.

NF5 Productivity/efficiency emphasis: Performance, speed, cost reduction, optimization, automation, streamlining workflows.

Appendix C. Illustrative Narrative Cues Used for coding

NF1 Assistant/partner framing – typical markers: assistant; copilot; partner; collaborator; teammate; helps you; works with you; supports you; your assistant.

NF2 Anthropomorphism/affective cues – typical markers: friend; human-like; empathic; understands; feels; caring; personal; conversational; ‘artificial human’.

NF3 Creativity support/empowerment – typical markers: co-create; generate ideas; inspire; enhance creativity; empower; learn with you; build together; creative collaborator.

NF4 Trust/transparency/ethical claims – typical markers: responsible; transparent; accountable; safe; privacy; secure; compliant; explainable; governed; trustworthy.

NF5 Productivity/efficiency emphasis – typical markers: faster; optimize; automate; streamline; reduce costs; increase efficiency; boost performance; accelerate workflows.

Coding note: Ambiguous phrases were coded only when supported by contextual evidence in the artifact (e.g., nearby claims about user control, transparency features, or explicit productivity metrics). This rule reduces inflation of frame prevalence in promotional texts.

Appendix D. Replication Checklist (Minimum Reporting Items)

1. Report sampling criteria and context of AI tool exposure.
2. Provide item wording and scale anchors for U, A, and T (or a representative subset, with the full list in Appendix A).
3. Define the marketing corpus and the collection window.
4. Provide the NF codebook (definitions and examples) and the coding unit (artifact-level).

5. Describe the coding procedure, disagreement resolution, and any double-coding or verification step.

6. Report descriptive prevalence of frames and the logic linking frames to user experience themes.

7. State limitations (sample scope, artifact selection, measurement constraints) and boundary conditions for interpretation.

Published by International Frequency Sensor Association (IFSA) Publishing, S. L., 2026 (http://www.sensorsportal.com).

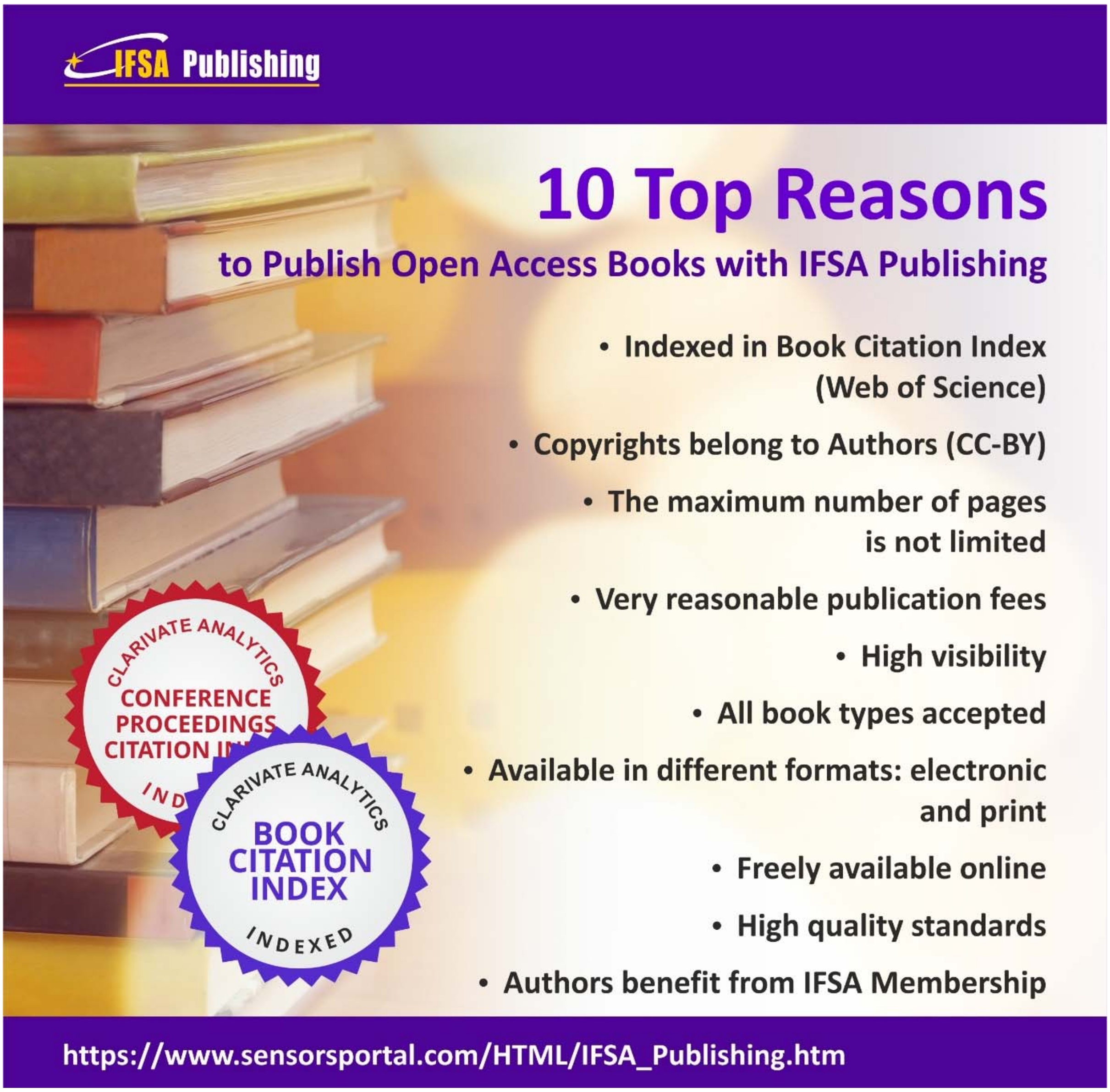

Call for Chapters

IFSA Publishing

Your Chapter may be in the next Volume of the popular Book Series

ADVANCES IN SENSORS 9

Open Access Book Series

Sinse 2012

- Physical, chemical and biosensors
- Sensor uncertainty, accuracy, calibration
- Smart sensors and systems
- Intelligent sensors and systems
- Artificial Intelligence enabled sensors
- Virtual and soft sensors
- Sensor instrumentation
- Sensor buses and networks
- Signal processing, sensor fusion
- Nanosensors
- Photonic sensors
- Sensor interfacing and signal conditioning
- Materials for sensors
- MEMS, BioMEMS and NEMS
- Remote Sensors and Telemetry
- Sensor packages and reliability

https://sensorsportal.com/ifsa_publishing.html

IFSA

International Frequency Sensor Association Publishing

www.sensorsportal.com

ISSN 1726-5479